Toward High Performance Broad-band Frequency Comb Operation of Terahertz Quantum Cascade Lasers

by

Chao Xu

A thesis
presented to the University of Waterloo
in fulfillment of the
thesis requirement for the degree of
Doctor of Philosophy
in
Electrical & Computer Engineering

Waterloo, Ontario, Canada, 2017

Examining Committee Membership

The following served on the Examining Committee for this thesis. The decision of the Examining Committee is by majority vote.

External Examiner	NAME	Ray LaPierre
	Title	Professor
Supervisor(s)	NAME	Dayan Ban
	Title	Professor
Internal Member	NAME	Zbigniew Wasilewski
	Title	Professor
Internal-external Member	NAME	Alexander Wong
	Title	Associate Professor
Other Member(s)	NAME	Young Ki Yoon
	Title	Assistant Professor

I hereby declare that I am the sole author of this thesis. This is a true copy of the thesis, including any required final revisions, as accepted by my examiners.

I understand that my thesis may be made electronically available to the public.

Abstract

Recent advances in Terahertz Quantum Cascade Laser (THz QCL) development are pushing this technology ever closer to practical application, particularly within the spectroscopic field. For this reason, optimizing the operation of THz QCL frequency combs, which can potentially provide unprecedented accuracy and stability to the optical spectra in a broad frequency band, is of particular interest to the research community. The THz QCLs frequency comb was only recently realized using two separate techniques: either a broad-gain active region or a group velocity dispersion controlled waveguide. However, due to residual optical dispersion from both the gain medium and the cold waveguide, comb formation in these reported THz QCLs can only sustain a limited current injection region and the observed comb frequency range is much narrower than the bandwidth of the designed gain medium.

To overcome these limitations, this thesis targets a new THz QCL frequency comb device design that simultaneously exploits the broadband gain active region and a group velocity dispersion (GVD)-compensated waveguide over an octave frequency band of 2-4 THz. In designing a broadband gain active region, two heterogeneous structures are proposed and simulated, with one combining three different bound-to-continuum (BTC) active regions operating at a temperature of 25 K, and another one consisting of four different resonant-phonon (RP) active regions operating at the liquid nitrogen temperature (77 K) or higher. The simulation results show that both active region designs can provide a broadband and ‘flat-top’ gain profile covering the frequency range from 2 to 4 THz. To design a group velocity dispersion-compensated waveguide, strategies are explored for simulating chirped Distributed Bragg Reflectors (DBRs) that can serve as THz QCL metal-metal waveguides, and one-dimensional (1D) and three-dimensional (3D) modeling approaches are established and verified. A novel two-section chirped DBR is proposed, which provides substantially-improved group delay compensation over a broadband octave frequency range from 2 to 4 THz.

Two THz QCL structures are grown using in-house molecular beam epitaxy and THz QCL devices equipped with a metal-metal waveguides are fabricated in the University of Waterloo Quantum-Nano-Centre clean-room fabrication lab. The experimental results demonstrate that the new THz QCL active region design can operate up to a maximum lasing temperature of 111 K, and with a broad lasing spectrum covering frequencies from 2.36 to 2.86 THz under pulse mode, at temperature of 13 K. The combined theoretical and experimental work would ultimately lead to the demonstration of improved THz QCL frequency comb operation over the broadband range from 2 to 4 THz.

Acknowledgements

First and foremost, I would like to acknowledge Professor Dayan Ban for supervising my work on this project. His enthusiasm for research has been both infectious and inspiring, and without his efforts and encouragement this PhD would not have been possible.

I would also like to thank Professors Alex Wong, Ray LaPierre, Youngki Yoon, and Zbigniew Wasilewski for spending the time, and having the patience, to serve on my thesis committee. Special thanks also goes to Professor Wasilewski and Mr. Man Chun Tam (Alan) for their great efforts in setting up and calibrating a new MBE system at the University of Waterloo and providing excellent MBE growth for this project.

It goes without saying that many of collaborators helped me during my time here. In particular, I owe a debt of gratitude to Dr. Seyed Ghasem Razavipour, who was always generous with his ideas and provided invaluable support throughout the modeling of our THz QCL active region design. I attribute many of the skills I have today to his training. It is also a pleasure to thank Siyi Wang and Dr. Guocheng Liu who spent many days (and nights) with me in the Quantum-Nano-Centre cleanroom, fabricating devices. I also wish to thank Boyu Wen, for designing the vacuum chamber and cold finger for this project and assisting me with setting up the new LJV system in our lab, and Xiaoliang He, Yue Zhuo, Alam Mahmud for assisting me in the experimental work.

Furthermore, I am grateful to many past and present students in this research group, including Dr. Jun Chen, Dr. Rudra Dhar, Dr. Simon Ferre, Jianchen Tao, Hao Wang, Nolan Lassaline, Burak Tekcan, and Cathy Wang, who maintained the highly motivated and intellectual environment in this group.

Finally, I would like to thank my parents for raising me and supporting me during these years of my PhD project.

Table of Contents

List of Tables

List of Figures

List of Abbreviations

1D	one-dimensional
3D	three-dimensional
AlAs	aluminum arsenide
$Al_xGa_{1-x}As$	aluminium gallium arsenide (with a composition of x for aluminum)
Ar	argon
Au	gold
BCl_3	boron trichloride
BTC	bound-to-continuum
Cl_2	chloride
CO_2	carbon dioxide
CSL	chirped super-lattice
CW	continue wave
DBR	distributed Bragg reflector
DC	direct current
DI	deionized
EM	electromagnetic
FP	Fabry-Perot
FTIR	Fourier-transform infrared
FWHM	full wave half maximum
FWM	four wave mixing

GaAs	gallium arsenide
GVD	group velocity dispersion
HCl	hydrogen chloride
H_2O	water
IDP	Indirectly pumped
IPA	isopropanol
IV	current-voltage
JV	current density-voltage
LJV	light-current density-voltage
LO	longitudinal - optical
MBE	molecular beam epitaxy
MIR QCLs	mid-infrared quantum cascade lasers
RF	radio frequency
RIE	reactive ion etching
RP	resonant-phonon
SA	sacttering-asssited
SISP	semi-insulating surface-plasmon
SWIFT	shifted wave interference Fourier-transform
THz QCLs	terahertz quantum cascade lasers
Ti	titanium
TO	transverse-optical
XRD	X-ray diffraction

Chapter 1

Introduction

The electromagnetic spectrum is broad, spanning frequencies from ~100 kHz (wavelength around ~3 km) to ~100 PHz (wavelength around ~10 nm). Two technologies have been developed to satisfy application demand across this vast frequency range; one to provide an efficient light source at the lower radio frequency (RF) end of the spectrum (electronic transmitters), and a second to serve the higher, optical frequency end (optical lasers) [1].

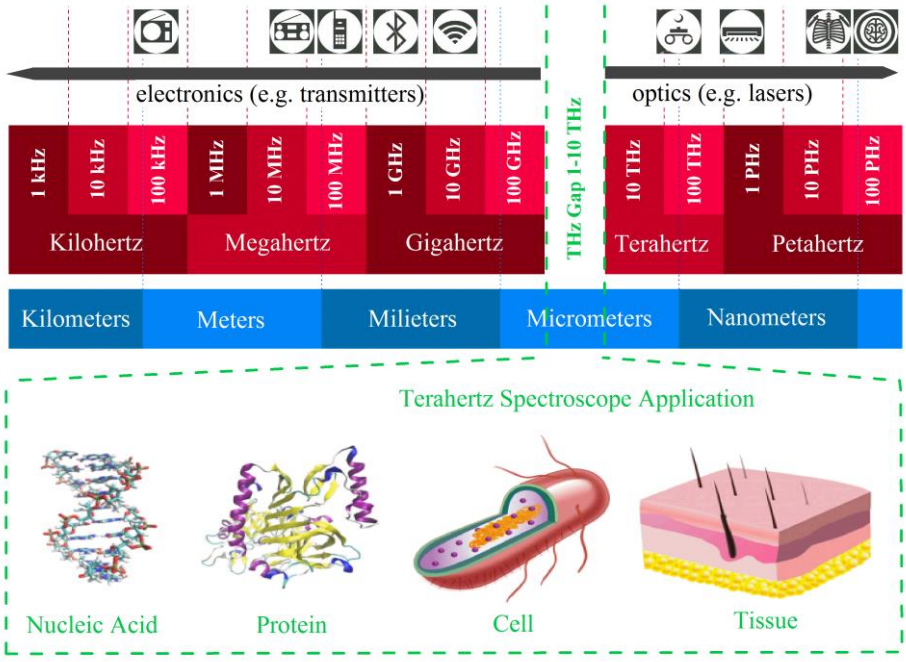

Figure 1.1 The terahertz gap, lying between 1-10 THz, exists because the frequencies generated by transistors and semiconductor lasers don't overlap. However, the terahertz radiation in this range is in great demand for biomedical spectroscopy applications [2].

However, while these technologies are highly efficient at the extreme ends of the

electromagnetic spectrum, neither can efficiently convert electrical power into terahertz radiation, creating a gap in the spectrum between 1 and 10 THz where the frequency ranges of these technologies do not meet (as shown in Figure 1.1).

In recent decades, there has been growing interest in leveraging the terahertz radiation from this 'gap' in the frequency band for spectroscopy and imaging applications. Since terahertz radiation closely approximates the energy of most bio-molecular motions, various biomolecules can be effectively identified, monitored, and characterized through their spectral fingerprints lying within this frequency gap [2][3][4]. To fill the gap, a great many light sources with potential to generate terahertz radiation have been proposed [5]: 1. Gas lasers, which discharge electric current through a gas medium, exploit transitions of certain molecules (e.g. CO_2) between their rotational states, allowing generation of discrete frequencies in a wide range, typically with output powers of a few milliwatts. However, the conversion efficiency for these technologies is very low (<0.1%) [6]. 2. Some high-frequency oscillators, such as Gunn diodes, Impatt diodes and resonant tunneling diodes have been optimized to emit frequencies above 2 THz, but demonstrate poor performance than that at low frequencies (GHz) [7][8][9]. 3. Free electron lasers, which achieve light amplification in an undulator fed with fast electrons, can be constructed to emit very high power in the terahertz spectral region. While useful for various research purposes, these technologies are both very large and expensive, which dramatically limits their usefulness for general terahertz applications [10]. 4. Photoconductive antennas have been developed for terahertz radiation generation [11]. These antennas consist of two short metallic stripes separated by a small gap, and are made on a semiconductor material with a short charge carrier lifetime. As a direct current (DC) bias voltage is applied to the stripes, an intense ultrashort laser pulse from a mode-locked laser is focused on the region between the metallic stripes, inducing a sudden electric current in the antenna, which in turn leads to terahertz radiation. The antennas must be pumped by high intensity mode-locked lasers, which is prohibitive for practical applications.

Finally, in 2002, Kohler et al. developed a technique to extend mid-infrared quantum cascade laser (MIR QCL) function into the terahertz frequency range and

demonstrated the world's first terahertz quantum cascade laser (THz QCL) - an efficient, electrically-pumped terahertz radiation source in which light emission relies on intersubband transitions [12]. With strident efforts to improve the performance of these devices (e.g. increase the operating temperature) through the last 15 years, the THz QCL has become the most efficient and compact terahertz radiation source available, and is now attracting significant interest for potential application [13].

1.1 Potential application of terahertz comb spectroscopy

The advent of THz QCL technologies has intensified efforts to push the limits of device performance, and opened up new lines of research to realize a range of specialized practical applications. Terahertz spectroscopy is a rapidly emerging field of study, for example, where recent advances in optical frequency comb development may offer the opportunity to create highly-precise measurement tools using current THz QCL technology.

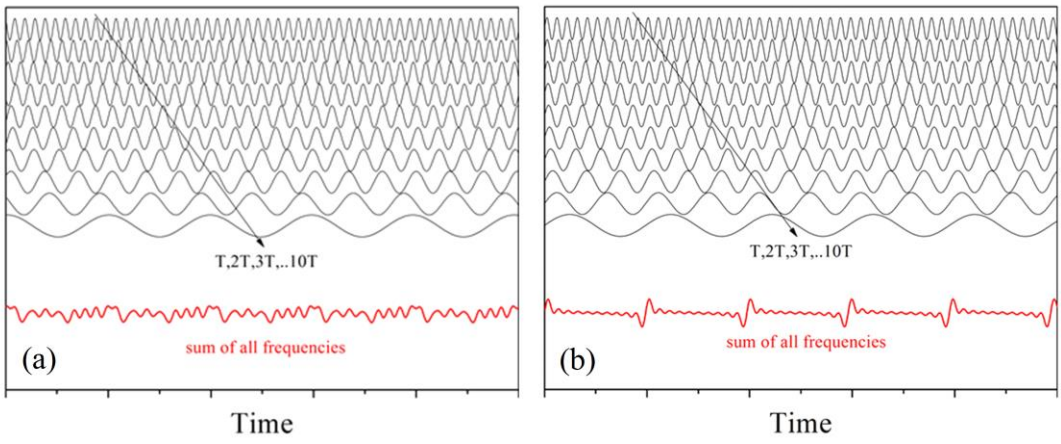

Figure 1.2 Time-frequency interpretation of the output of a conventional laser (a) and a comb laser (b). Each has 10 involved lasing modes, but demonstrate different frequency distributions. (a) The lasing modes in a conventional semiconductor laser are characterized by a random phase and uncertain frequencies due to the dispersion and noise, thus the output (red curve) looks like a CW laser. (b) The phase and frequencies of lasing modes in a comb laser are locked by the FWM effect, thus the output is a train of pulses.

The distinct advantage of frequency combs lies in their stability, predictability and control. The lasing modes (Fabry-Perot modes) within the optical spectra of conventional QCLs operate independently, which means the phase noise and the interval frequencies of two adjacent lasing modes evolve randomly with the time of operation due to the dispersion or external noise, as shown in Figure 1.2(a). An optical frequency comb, on the other hand, consists of equidistant frequencies and a correlated phase of its lasing [14][15][16][17]. This is the result of the four wave mixing (FWM) effect, which works like a chain, locking the lasing modes and mitigating the dispersion and external noise. If the FWM is strong enough to lock many lasing modes with a high order of synchronization, a train of short pulses with a fixed repetition rate will be formed, as shown in Figure 1.2(b). A stabilized frequency comb has excellent frequency accuracy for each lasing mode and, at the same time, broad frequency band coverage. In some well-controlled frequency comb lasers, the accuracy of the individual lasing modes can be restricted below Hz level over the hundreds of THz of the comb bandwidth [18], making these technologies very promising spectroscopic tools. Key examples including their use as frequency rulers and for direct frequency comb spectroscopy.

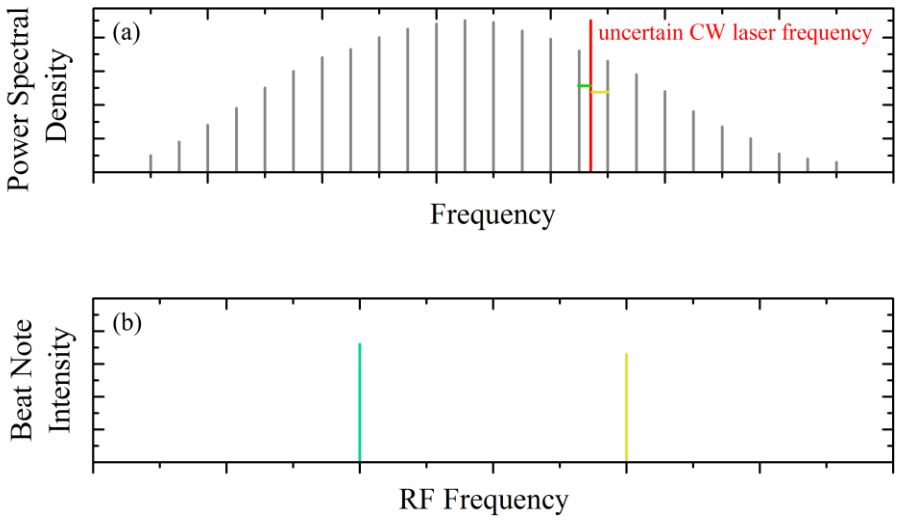

Figure 1.3 Illustration of an optical frequency comb operating as a frequency ruler, measuring a continue wave (CW) laser with uncertain frequency. (a) the uncertain CW laser line (red) lies between two adjacent comb teeth, which generates two beat note frequency signals, one for each tooth (green and yellow lines). (b) The frequencies of the beat notes can be accurately measured in a RF frequency spectrum.

When applied as a frequency ruler, the stabilized optical comb measures a continuous-wave (CW) laser, while the CW laser scans the samples and performs the spectroscopy [19][20]. Figure 1.3(a) shows the basic approach for measuring uncertain CW laser frequencies (the uncertainty should be less than the repetition frequency of the optical comb) using an optical frequency comb as a frequency ruler. When the unknown frequency line falls between adjacent teeth of an optical comb, two RF beat note signals (signal of differential frequency) are generated, which can be accurately detected with an RF electronic system. By measuring the frequencies of the two beat notes with an uncertainty below kHz level or even lower, the accurate frequency of the CW laser can accurately be calculated.

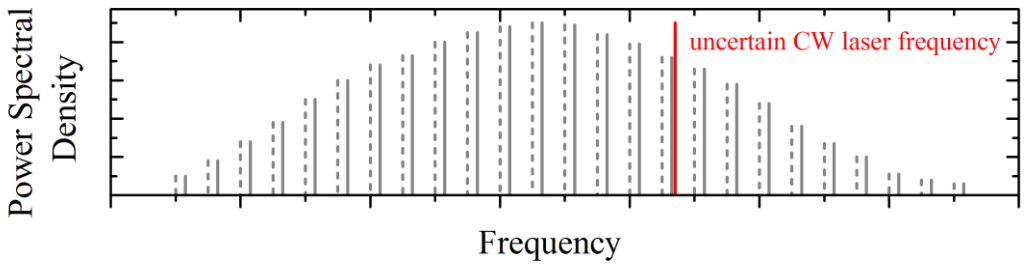

Figure 1.4 Optical frequency combs always exhibit a frequency offset, caused by intra-cavity dispersion, which shifts the absolute frequency of the comb teeth with time (indicated as dashed lines).

However, the optical ruler has one critical drawbacks, in that conventional frequency combs demonstrate a frequency offset, caused by intra-cavity dispersion and nonlinearities, as shown in Figure 1.4, which dramatically degrades the accuracy of the optical ruler. One of the best approaches to solving this problem is to take a 1f to 2f (where "f" refers to lasing mode frequency) self-referencing method to calibrate the optical comb itself, as shown in Figure 1.5.

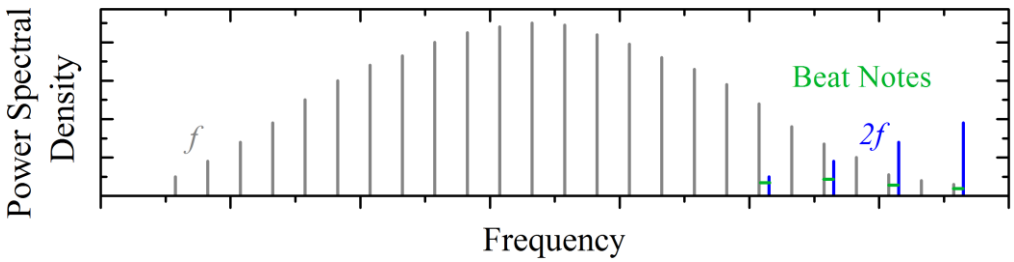

Figure 1.5 Principle of the 1f-2f self-referencing technique for comb offset frequency calibration. The higher frequencies of original comb teeth (grey, 1f lines) and the lower frequencies of the frequency-doubled comb teeth (blue, 2f lines) generate a RF beat note frequency equal to the comb offset frequency (green lines).

The 1f-2f self-referencing technique doubles the optical comb frequency using a frequency up-converter, then mixes the low frequency of the frequency-doubled comb teeth (2f lines) with the original optical frequency comb (1f lines), generating a RF beat note signal equal to the offset frequency. However, the frequency span of the original optical comb must be broad enough to contain both 1f and 2f frequencies, requiring an "octave frequency spanning frequency comb".

Apart from their use as frequency rulers, comb lasers can also be applied to frequency dual-comb spectroscopy [21][22]. As illustrated in Figure 1.6, a system generates two frequency combs with interval frequencies (repetition rates) slightly detuned from each other (~kHz), where one comb serves as a probe source, and the other acts as a reference source. Measurement results can be expressed in terms of frequency and time. For example, the slight detuning of individual pairs of teeth from each comb source generates a comb of beat notes on the RF spectrum, which is easily measurable with an RF electronic detection system. Once the probe comb passes through sample materials, the change of both its phase and amplitude in response to the sample material will be fully recorded and expressed on the RF comb spectrum after interfering with the reference comb. On the other hand, the slight difference in their repetition rates between the combs looks like two short pulses, separated by a slight time delay, walking through each other (one pulse passing through the sample). While this approach is similar to Fourier transform

infrared spectroscopy, the dual comb technique has many of advantages such as fast full spectrum scanning time without the need for moving parts and highly focused power for trace detection [23].

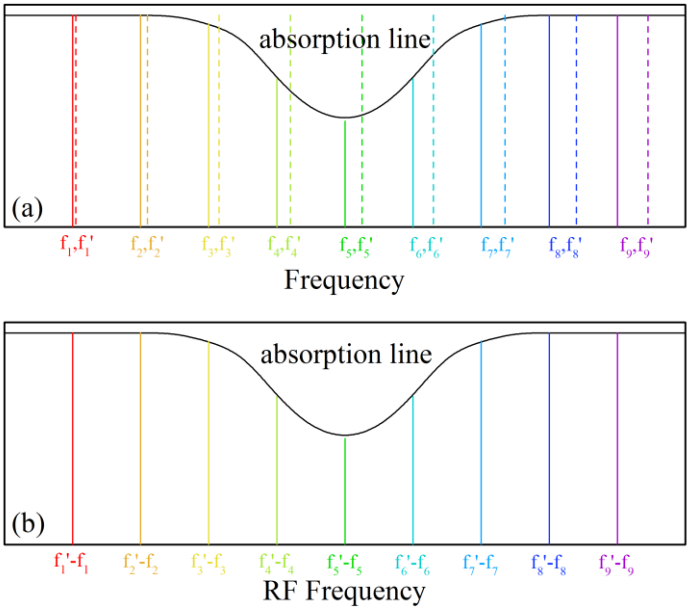

Figure 1.6 Principle of dual comb spectroscopy. (a) Two optical frequency combs with slightly different repetition frequencies. One serves as a probe beam and passes through the sample (solid lines), while the other acts as reference beam (dashed lines). (b) The two optical combs are mixed on a photodiode, generating an RF frequency comb.

1.2 Basic principles of designing a THz QCL

1.2.1 THz QCL active region

The band engineering of the active region is a crucial aspect of THz QCL design. Molecular Beam Epitaxy (MBE) is generally used to grow the multiple-quantum-well active region in the GaAs/$Al_xGa_{1-x}As$ material system. One of the advantages of using GaAs/$Al_xGa_{1-x}As$ material for THz QCLs is that GaAs and AlAs have almost the same lattice constant, thus,

when combined, their compound alloy has very little induced strain, which allows them to be grown to an almost arbitrary thickness. By tuning the thickness of quantum wells (GaAs) and barriers ($Al_xGa_{1-x}As$) in the supper-lattice structure, we can properly engineer the energy states, the wavefunctions, and the transition rates of carriers in the conduction band of the material to provide population inversion between two lasing states. As a key parameter to describe THz QCL performance, the optical gain must be optimized. The fundamental concept in optimizing the optical gain of the active region is to maximize the carrier injection efficiency to the upper lasing state and the extraction efficiency from the lower lasing state. As a result, the higher carrier population inversion between two lasing states can be achieved. Several different active region design schemes have been investigated to improve THz QCL performance [24].

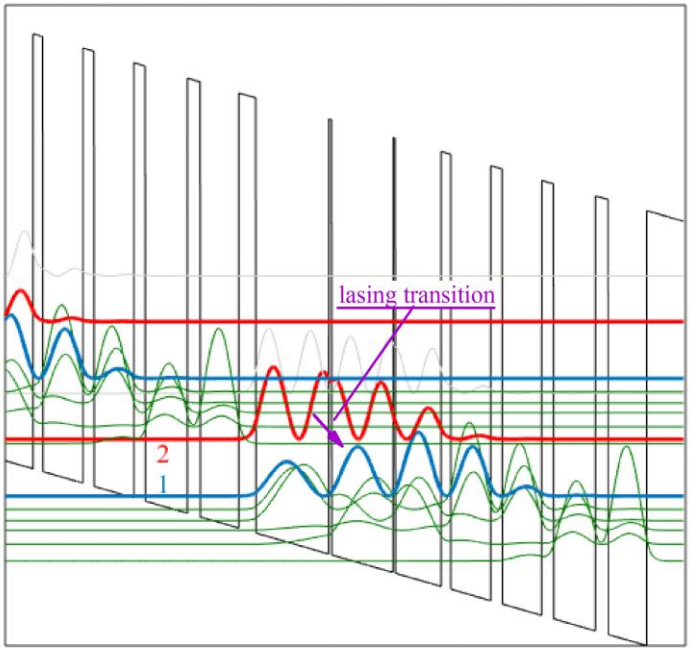

Figure 1.7 Conduction band diagram of THz QCL active region design based on CSL structure.

The first THz QCL design, demonstrated by Kohler in 2002, is based on a chirped super-lattice (CSL) structure [12][25][26]. As shown in Figure 1.7, the CSL structure is

formed by coupling several quantum wells together to create mini-bands of states when the appropriate electric field is applied. In this kind of active region, most radiation transitions take place from the lowest state of the upper mini-band (state 2) to top state of the lower mini-band (state 1). Due to the relatively small bandwidth of the mini-bands, a longitudinal-optical (LO) phonon is not directly involved in the carriers' transition process.

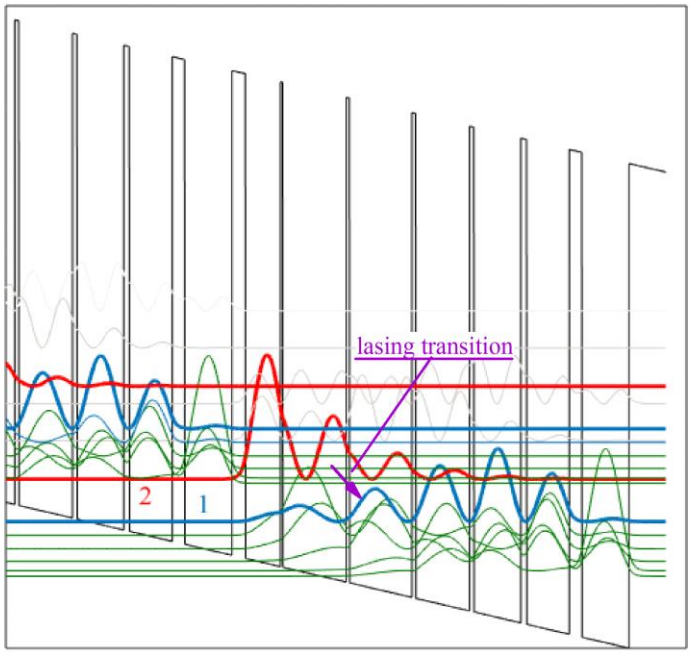

Figure 1.8 Conduction band diagram of THz QCL active region design based on BTC structure.

After the design of CSL structures, the bound-to-continuum (BTC) structure was demonstrated [27][28][29]. The BTC structure is similar to that of CSL designs, but with the upper lasing mini-band re-designed to become a bounded state (state 2, as shown in Figure 1.8). Compared to the CSL design, the BTC structure demonstrates a slight drop in transition oscillator strength due to a decreased overlap between the upper bounded state and lower mini-band. However, since the lifetime of the upper bounded state increases dramatically, the BTC structure demonstrates better temperature and power performance.

In 2003, the resonant-phonon (RP) structure, which is commonly used for most MIR QCLs, was adapted to THz QCLs design [30][31][32]. As shown in Figure 1.9, the RP structure extraction state strongly overlaps with the lower lasing state (state 1), while the injection state for the next module is designed to be lower than the extraction state by approximately 36 meV. This creates energy spacing that corresponds to the LO phonon energy in GaAs material, allowing the electrons in the lower lasing state to relax quickly and drop below the extraction state. Then, the carriers in the injection state tunnel through the injection barrier into the next module.

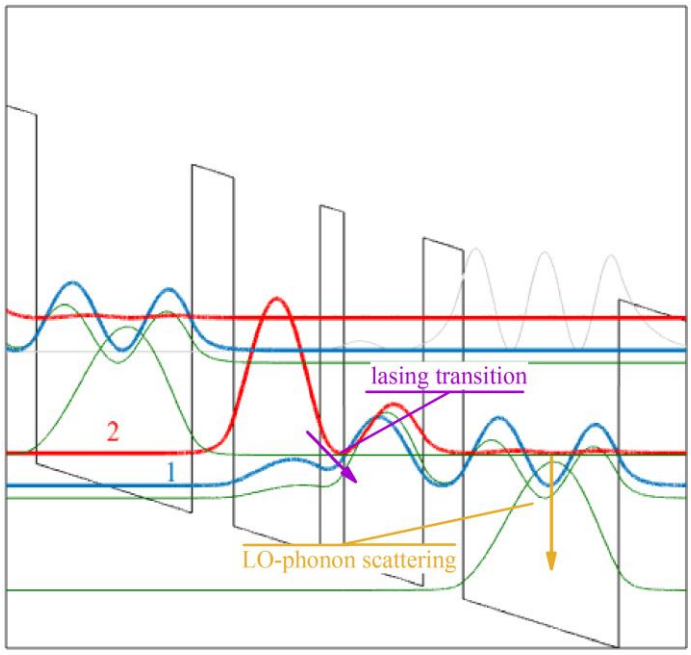

Figure 1.9 Conduction band diagram of a THz QCL active region design based on RP structure.

Many early RP THz QCL designs contained a key flow that prevented lasing. That is, they created very close energy spacing between two lasing states (~10 meV), making it difficult to use LO-phonon scattering to depopulate the lower lasing state without also depopulating the upper lasing state. A feasible solution is to extend the wavefunction of the lower lasing state far away from the quantum well where the injection state is located. As

a result, the lower lasing state maintains a strong spatial overlap with the extraction state and experiences very fast LO-phonon scattering. However, instead of creating a mini-band in the RP structure, the bounded lower lasing state causes decreased oscillator strength below that of BTC structures, which is only partially compensated for by the fact that the length of a RP module is typically half that of a BTC module, which results in a higher density of gain medium (the active region can contain more modules).

New THz QCL designs based on scattering assist (SA) carrier injection and extraction have recently been investigated (as shown in Fig. 1.10) [33][34]. Since the carriers experience consecutive phonon, photon, and phonon transitions in each module, these structures are called indirectly pumped (IDP) QCLs or phonon-photon-phonon (3p) QCLs. For example, in one kind of SA structures, a four-well structure consisting of two double-phonon wells leads to a faster phonon scattering process, as shown in Figure 1.10.

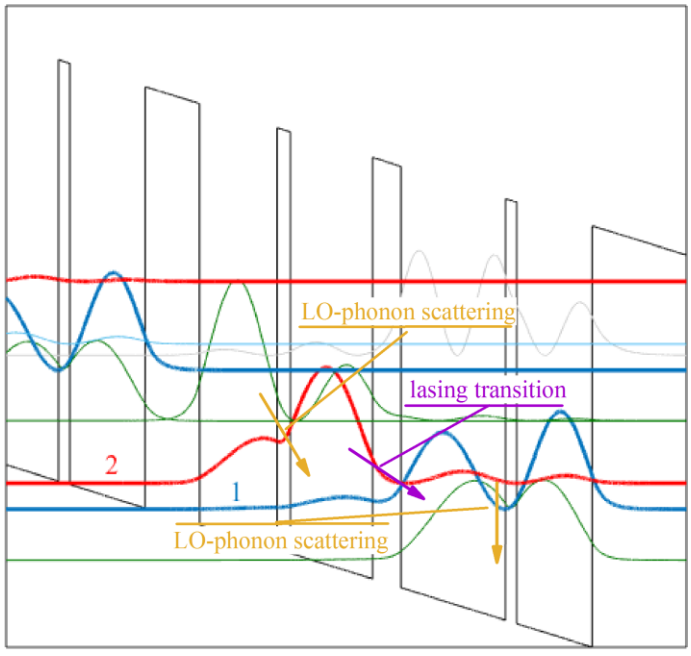

Figure 1.10 Conduction band diagram of a THz QCL active region design based on SA structure.

In addition, the energy spacing of each double well is set based on GaAs LO-phonon energy (~36.7 meV). Since the energy spacing between the injection state and lower lasing state in these devices is at least 36.7 meV, the negative impact of a carrier incorrectly travelling from the injection state to the lower lasing state (state 1), instead of upper lasing state (state 2), is much smaller for a 3p structure than for an RP structure. Thus, SA structure-based THz QCLs demonstrate good temperature performance, output power, and large lasing dynamic range. However, these advantages come at the cost of high applied bias and injected current density.

1.2.2 Waveguides

Optical waveguides are spatially heterogeneous structures for guiding light, and are essential in semiconductor lasers. The design work of high optical confinement and low loss THz QCL waveguides has proven more difficult than for conventional devices, due to the long wavelengths of electromagnetic (EM) waves. To date, two waveguide designs have been successfully applied to THz QCLs, namely: the semi-insulating surface-plasmon (SISP), and the metal-metal waveguide, as shown in Figure 1.11. The success of world's first THz QCL, demonstrated by Kohler et al., can be partially attributed to its low-loss SISP waveguide. The SISP waveguide involves the growth of a thin (0.2-0.8 μm thick) heavily doped layer underneath a ~10-μm-thick active region, but on top of a semi-insulating GaAs substrate. This structure guides EM wave between the top metal contact and the lower heavily doped layer. Although the mode crosses the high-loss heavily doped layer and extends substantially into the substrate, it overlaps only slightly with the heavily-doped layer, thus the free-carrier loss is not significant [12][35]. The confinement factor of the THz QCL SISP waveguides is low, typically ranging from 0.1 to 0.5, which suppresses excitation of higher order lateral modes inside the cavity. This presents a significant shortcoming, where the modes in waveguides with narrow ridge widths (below 100 μm) are squeezed into the substrate, resulting in increased optical loss.

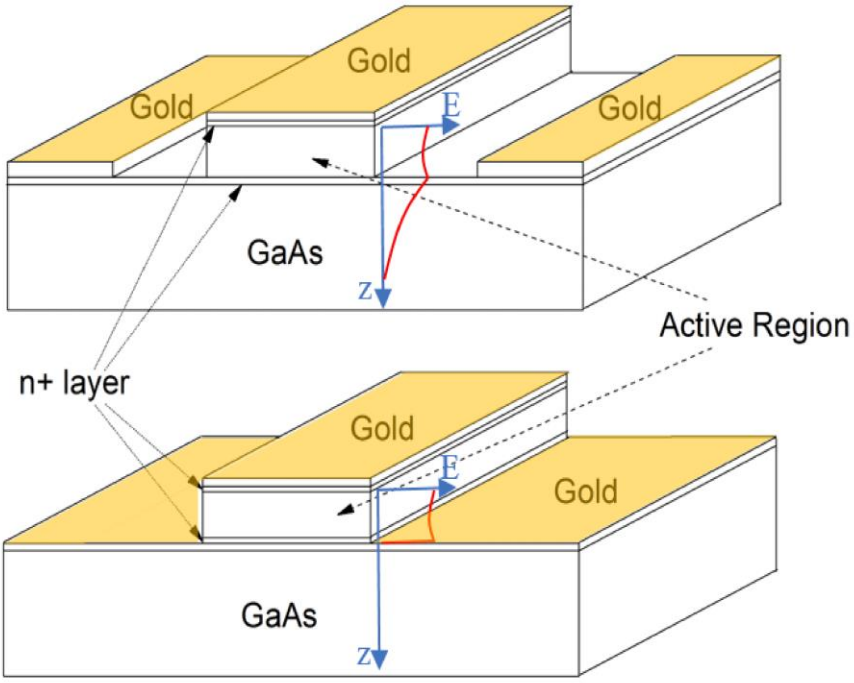

Figure 1.11 Schematic of SISP waveguide (top) and metal-metal waveguide (bottom). Red curves show the mode distributions (vertical) in each waveguide.

By contrast with the SISP waveguide design, the metal-metal waveguide, first deployed in 2003 [36], affixes a metal layer instead of a heavily doped semiconductor layer along the bottom of the active region. The optical modes inside the metal-metal waveguide are almost completely confined into the active region, which results in a higher order lateral mode inside the cavity. The competition between the fundamental lateral mode and the higher order modes causes a distortion in the output power of THz QCL devices [37], and may break the stability of comb formation in optical comb lasers. To solve this problem, two narrow strips of highly-doped contact layer are fabricated and placed along both sides of the top metal contact. The exposed side strips generate a significantly stronger loss on higher lateral modes, which are distributed closer to the exposed side strips than that of the fundamental lateral mode, which are distributed closer to center region. As a result, the higher order lateral modes are suppressed [38].

1.3 Comb operation in THz QCLs

The FWM effect, which is an intermodulation phenomenon explained in non-linear optics, enables comb operation inside the THz QCL cavity. To demonstrate, suppose one cavity mode is generated at the transition frequency ω of the lasing states, as shown in Figure 1.12. The degenerated FWM (ω, $\omega + \omega_{\mathrm{rt}}$ and $\omega - \omega_{\mathrm{rt}}$ involved) will lock the side-band frequencies of the original cavity mode. Then the non-degenerated FWM (e.g. ω, $\omega - \omega_{\mathrm{rt}}$, $\omega + \omega_{\mathrm{rt}}$, and $\omega \pm 2\omega_{\mathrm{rt}}$) will lock the side-band of the cavity modes into a broad frequency band, where the comb operation is formed.

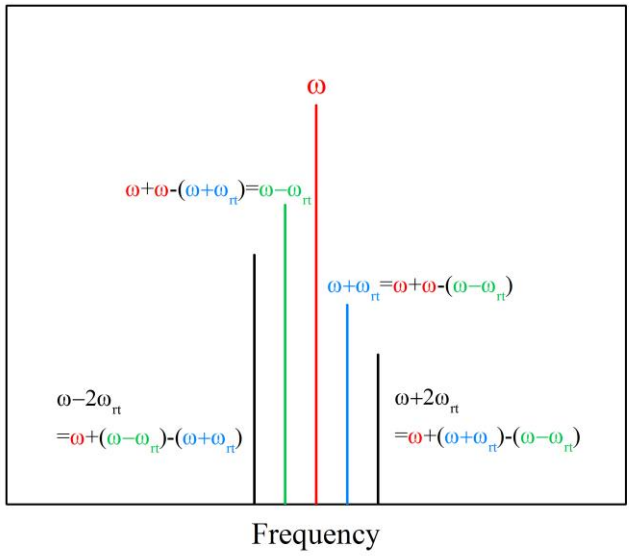

Figure 1.12 A simplified explanation of optical comb formation at the side bands of the transition frequency ω.

To clearly explain how the FWM effect works on THz QCL cavity modes, we introduce a model simplified from [39][40]. The model is based on the density matrix of a two-level system with carrier populations, ρ_{11} and ρ_{22}, on lower state 1 and upper state 2, which is an approximation for describing two lasing states in a THz QCL. The model can be defined thus:

$$\begin{pmatrix} \dot{\rho}_{11} & \dot{\rho}_{12} \\ \dot{\rho}_{21} & \dot{\rho}_{22} \end{pmatrix} = -\frac{i}{\hbar}\left[\begin{pmatrix} \hbar\omega_1 & \hbar\Omega_{12} \\ \hbar\Omega_{21} & \hbar\omega_2 \end{pmatrix}, \begin{pmatrix} \rho_{11} & \rho_{12} \\ \rho_{21} & \rho_{22} \end{pmatrix}\right] + \begin{pmatrix} -\gamma_{11}\rho_{11} & -\gamma_{21}\rho_{12} \\ -\gamma_{12}\rho_{21} & -\gamma_{22}(\rho_{22} - \rho_{22,p}) \end{pmatrix} \tag{1.1}$$

where $\Omega_{12} = \Omega_{21} = \mu_{21}E/\hbar$ is time dependent Rabi frequency, μ_{21} is the dipole matrix element, and γ_{11} and γ_{22} are transition rates from state 1 and 2. Assuming the carrier population on the lower state is negligible ($\rho_{11} \approx 0$),

$$\Delta\dot{\rho} = 2i\Omega_{12}(\rho_{21} - \rho_{12}) - \gamma_{22}(\Delta\rho - \Delta\rho_p)$$

$$\dot{\rho}_{21} = -i\omega_{21}\rho_{21} + i\Omega_{12}\Delta\rho - \gamma_{21}\rho_{21}$$

$$\dot{\rho}_{21} = \dot{\rho}_{12}^*$$

(1.2-1.4)

where $\Delta\rho = \rho_{22} - \rho_{11}$, and $\omega_{21} = \omega_2 - \omega_1$ is the transition frequency between two states. To solve Equation 1.2-1.4, we expand the time dependent quantities based on the frequencies of the cavity modes ($\omega_l = \omega_{21} + l\omega,\ l \in [-n, n]$,n is integer), where ω is the cavity round trip frequency. This gives

$$E(t) = \frac{1}{2}e^{-i\omega_{21}t}\sum_{l=-n}^{l=n} A_l e^{-il\omega t} + c.c.$$

$$\Omega(t) = \frac{\mu_{21}E(t)}{\hbar} = \frac{1}{2}e^{-i\omega_{21}t}\sum_{l=-n}^{l=n} \Omega_l e^{-il\omega t} + c.c.$$

(1.5-1.6)

where $\Omega_l = \mu_{21}A_l/\hbar$. If we assume ρ_{21} and ρ_{12} are driven only at nearly the resonance frequency ω_{21}, and $\Delta\rho$ is driven at nearly DC [41], we can also expand the density matrix on cavity mode frequencies as follows:

$$\rho_{21} = e^{-i\omega_{21}t}\sum_{k=-n}^{k=n} \sigma_{21,k}e^{-ik\omega t}$$

$$\rho_{12} = \rho_{21}^*$$

$$\Delta\rho = \sum_{r=-n}^{r=n} \Delta\rho_r e^{-ir\omega t}$$

(1.7-1.9)

For simplicity, we assume the cavity is driven in DC mode without active RF modulation, such that $\Delta\rho_p = \Delta\rho_{p,0}$. With the expanded form from Equation 1.5-1.9, the density matrix

Equation 1.2-1.4 can be rewritten into the following form:

$$\sum_{r=-n}^{r=n}(-ir\omega+\gamma_{22})\Delta\rho_r e^{-ir\omega t}=\gamma_{22}\Delta\rho_{p,0}+\frac{i}{2}\sum_{l=-n}^{l=n}\sum_{k=-n}^{k=n}(\Omega_l^*\sigma_{21,k}\,e^{-i(k-l)\omega t}-\Omega_l\sigma_{21,k}^*e^{i(k-l)\omega t})$$

$$\sum_{k=-n}^{k=n}(\gamma_{21}-ik\omega)\,\sigma_{21,k}e^{-ik\omega t}=\frac{i}{2}\sum_{l=-n}^{l=n}\sum_{r=-n}^{r=n}\Omega_l\Delta\rho_r e^{-i(l+r)\omega t}$$

(1.10-1.11)

A rotating wave approximation is used in the derivation of Equations 1.10 &1.11, such that the terms with high frequencies (e.g. $e^{-i2\omega_{21}t}$) are neglected. Then Equation 1.10 &1.11 can be solved by matching the $e^{-ik\omega t}$ terms on both sides of the equations ($r=\pm(k-l)$ for Equation 1.10, and $k=l+r$ for Equation 1.11), which yields

$$\Delta\rho_r=\frac{1}{-ir\omega+\gamma_{22}}[\gamma_{22}\Delta\rho_{p,0}\delta_{r,0}+\frac{i}{2}\sum_{k=-n}^{k=n}(\Omega_{k-r}^*\sigma_{21,k}+\Omega_{k+r}\sigma_{21,k}^*)]$$

$$\sigma_{21,k}=\frac{i}{2(\gamma_{21}-ik\omega)}\sum_{l=-n}^{l=n}\Omega_l\,\Delta\rho_{k-l}$$

(1.12-1.13)

The Equations 1.12 and 1.13 can be solved with a perturbative approach on $\Delta\rho_r$ and $\sigma_{21,k}$, giving

$$\Delta\rho_r^{(0)}\longrightarrow\sigma_{21,k}^{(1)}\longrightarrow\Delta\rho_r^{(2)}\longrightarrow\cdots$$

If $\Delta\rho_r^{(0)}=0$, we have

$$\sigma_{21,k}^{(1)}=\frac{i}{2(\gamma_{21}-ik\omega)}\Omega_k\Delta\rho_{p,0}$$

$$\sigma_{21,k}^{(3)}=\frac{i}{8(\gamma_{21}-ik\omega)}\sum_{l=-n}^{l=n}\sum_{m=-n}^{m=n}\Omega_l\frac{i\Delta\rho_{p,0}}{\gamma_{22}-i(k-l)\omega}\left(\frac{\Omega_{m-k+l}^*\Omega_l}{-i\gamma_{21}-l\omega}-\frac{\Omega_{m+k-l}\Omega_l^*}{i\gamma_{21}-l\omega}\right),\quad(n\neq l)$$

(1.14-1.15)

Substituting $m'=m-k+l, and\ m'\to m$ for the second last term in Equation 1.15, we can define

$$\tilde{G}_k = \frac{i\gamma_{21}}{k\omega + i\gamma_{21}}$$

$$B_{lm} = \frac{\gamma_{21}}{2i}\left(\frac{1}{-i\gamma_{21} - m\omega} - \frac{1}{i\gamma_{21} - l\omega}\right)$$

$$C_{lm} = \frac{\gamma_{22}}{\gamma_{22} - i(m-l)\omega}$$

(1.16-1.18)

The Equations 1.14 and 1.15 can then be rewritten as

$$\sigma_{21,k}^{(1)} = -\frac{1}{2\gamma_{21}}\tilde{G}_k \Omega_k \Delta\rho_{p,0}$$

$$\sigma_{21,k}^{(3)} = \frac{-i}{4\gamma_{22}\gamma_{21}^2}\tilde{G}_n \sum_{l=-n}^{l=n}\sum_{m=-n}^{m=n} C_{lm} B_{lm} \Omega_{m+k-l}\Omega_l \Omega_m^* \Delta\rho_{p,0}$$

(1.19-1.20)

If we only consider the approximation of $\sigma_{21,n}$ to third order, we have

$$\sigma_{21,n} = \sigma_{21,n}^{(1)} + \sigma_{21,n}^{(3)}$$

(1.21)

The electric field generated in this two-level system can be solved from Maxwell's Equations as follows:

$$\nabla^2 E - \mu_0 \sigma \frac{\partial E}{\partial t} - \frac{\varepsilon_r}{c^2}\frac{\partial^2 E}{\partial t^2} = \mu_0 \frac{\partial^2 P}{\partial t^2}$$

(1.22)

where σ is the conductivity, and ε_r is the relative permittivity of the cavity material. The electric fields E and the polarization P can be expanded as in Equation 1.5, such that

$$E(t) = \frac{1}{2}\sum_{l=-n}^{l=n} A_l e^{-i\omega_l t} + c.c.$$

$$P(t) = \frac{1}{2}\sum_{l=-n}^{l=n} P_l e^{-i\omega_l t} + c.c.$$

(1.23-1.24)

where $P_l = -N\mu_{21}\sigma_{21,l}$ (N is the sum of all 2-level states in the active region). Since the envelope form $A_l(t,z)$ has a special dependence

$$A_l(t,z) = A_l(t)\sin(k_l z)$$

(1.25)

where k_l is the wave-vector for the l_{th} mode in the cavity. Solving Equation 1.22 by substituting $E(t)$, $P(t)$ with the expanded terms from Equations 1.23, 1.24, and 1.25, and assuming the envelope form evolve slowly ($\ddot{A}_l(t) = 0$), yields

$$\sin(k_l z)\left\{\left[(\omega_l^2 - \omega_{lc}^2) + \frac{i\omega_l\sigma}{\varepsilon_0\varepsilon_r}\right]A_l + \left(2i\omega_l - \frac{\sigma}{\varepsilon_0\varepsilon_r}\right)\dot{A}_l\right\} = \frac{1}{2\varepsilon_0\varepsilon_r}N\omega_l^2\mu_0\mu_{21}\sigma_{21,l}(z)$$

(1.26)

where $\omega_{lc} = k_l c/\sqrt{\varepsilon_r}$ is the eigen-frequency of the l_{th} mode, and $\omega_l = \omega_{lc}$ only if the cavity has no GVD. If we assume $\omega_l \gg \sigma/\varepsilon_0\varepsilon_r$ for a low loss cavity, Equation 1.26 can be written into the following form:

$$\dot{A}_l - i\frac{\omega_l^2 - \omega_{lc}^2}{2\omega_l}A_l = -\frac{i\omega_l N\mu_{21}\sigma_{21,l}(z)}{2\varepsilon_0\varepsilon_r\sin(k_l z)} - \frac{\sigma}{2\varepsilon_0\varepsilon_r}A_l$$

(1.27)

If the resonant mode $\omega_l = \omega_{lc}$, and no polarization exists ($\sigma_{21,l}(z) = 0$), then Equation 1.27 is simplified to

$$\dot{A}_l = -\frac{\sigma}{2\varepsilon_0\varepsilon_r}A_l$$

(1.28)

where the coefficient $-\sigma/2\varepsilon_0\varepsilon_r$ describes the decreasing rate of the photons (loss) inside the cavity. It is convenient to define a decay rate for this model, where $\tau_c = \varepsilon_0\varepsilon_r/\sigma$. To remove the spatial form in Equation 1.27, we integrate both sides of Equation 1.27 over the cavity length (by $(\frac{1}{l_c})\int_0^{l_c} f(z)dz$), and obtain

$$\dot{A}_l - i\frac{\omega_l^2 - \omega_{lc}^2}{2\omega_l}A_l = -\frac{i\omega_l N\mu_{21}}{\varepsilon_0\varepsilon_r}\frac{1}{l_c}\int_0^{l_c}\sigma_{21,l}(z)\sin(k_l z)\,dz - \frac{1}{2\tau_c}A_l$$

(1.29)

Expanding the integral item in Equation 1.29 with Equation 1.21, we have

$$\frac{1}{l_c}\int_0^{l_c}\sigma_{21,l}^{(1)}\sin(k_l z)\,dz \sim \frac{1}{l_c}\int_0^{l_c}\Omega_l(z)\sin(k_l z)\,dz = \frac{1}{l_c}\int_0^{l_c}A_l\sin(k_l z)\sin(k_l z)\,dz = \frac{A_l}{2}$$

$$\frac{1}{l_c}\int_0^{l_c}\sigma_{21,l}^{(3)}\sin(k_l z)\,dz \sim \frac{1}{l_c}\int_0^{l_c}\Omega_{l+k-m}\Omega_m\Omega_k^*\sin(k_l z)\,dz$$
$$= \frac{1}{l_c}\int_0^{l_c}A_{l+k-m}A_m A_k^*\sin(k_{l+k-m}z)\sin(k_m z)\sin(k_k z)\sin(k_l z)\,dz$$
$$= A_{l+k-m}A_m A_k^* K_{l+k-m,m,k,l} \tag{1.30}$$

where $K_{l+k-m,m,k,l} = \frac{1}{l_c}\int_0^{l_c}\sin(k_{l+k-m}z)\sin(k_m z)\sin(k_k z)\sin(k_l z)\,dz$. To further simplify the Equation 1.29, we introduce

$$g_0 = \frac{\omega_l \tau_c N \mu_{21}^2 \Delta\rho_{p,0}}{2\varepsilon_0\varepsilon_r\hbar\gamma_{21}}$$
$$G_l = g_0\tilde{G}_l \tag{1.31-1.32}$$

Substituting Equation 1.30, 1.31, and 1.32 into Equation 1.29, and normalizing the time to $2\tau_c$, yields

$$\dot{A}_l = \left[G_l - 1 + i\frac{\omega_l^2 - \omega_{lc}^2}{2\omega_l}\right]A_l - G_l\sum_{k=-n}^{k=n}\sum_{m=-n}^{m=n}C_{km}B_{km}A_{l+k-m}A_m A_k^* K_{l+k-m,m,k,l} \tag{1.33}$$

The Equation 1.33 describe the evolution of the amplitude of the *l*th mode, and which is also modulated by any groups of another three modes (k^{th}, m^{th}, and l+k-m^{th} mode) due to the FWM effect. A calculation is made with MATLAB to solve Equation 1.33. For simplicity, we removed the cavity dispersion term ($i\frac{\omega_l^2-\omega_{lc}^2}{2\omega_l}$) from Equation 1.33. where we assume $\tau_2 = 1/\gamma_{22} = 12\,ps$, $\tau_{coh} = 1/\gamma_{21} = 0.7\,ps$, and $\tau_{rt} = 1/\omega = 63\,ps$ (corresponding to a 3 mm long device) [40].

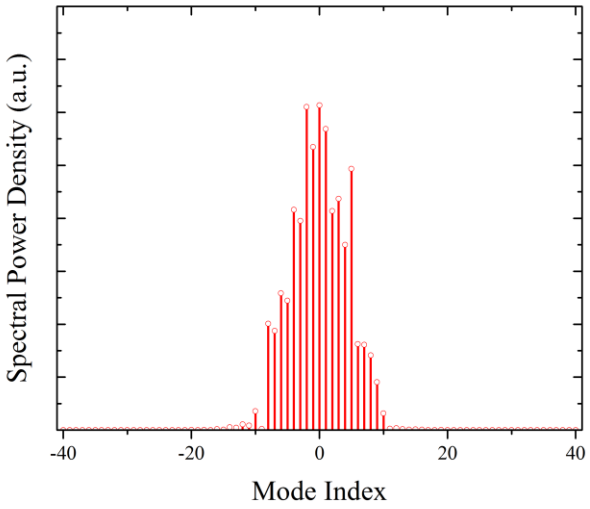

Fig. 1.13 Calculated optical amplitude of lasing modes around the transition frequency in a free running THz QCL.

In Figure 1.13, the calculated amplitudes of the modes are distributed in a somewhat Gaussian shape showing how the optical comb is generated at the side bands of the transition frequency (0^{th} mode). From this, we can then illustrate the cavity dispersion effect by including the $(i\frac{\omega_l^2-\omega_{lc}^2}{2\omega_l})$ term back into the model.

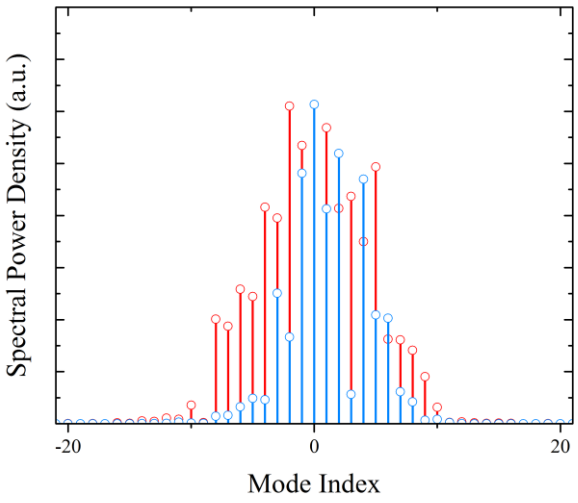

Fig. 1.14 Calculated optical amplitudes of lasing modes around the transition frequency in a free running THz QCL with (blue) and without (red) cavity dispersion.

Figure 1.14 shows the calculated spectral power density of the lasing modes with an introduced cavity dispersion of GVD=10^5 fs^2mm^{-1} ($GVD = \partial^2 k/\partial\omega^2$) (blue lines). Compared with the results from an ideal cavity (i.e., with no dispersion, red), the spectrum becomes narrower in its frequency bandwidth in a dispersion induced cavity. Clearly, the cavity dispersion damages the comb formation inside the THz QCL. Apart from the cavity dispersion, the non-flat gain medium across the broad frequency band width also introduces dispersion into the laser operation [42], and which may significantly degrade comb operation in high injection conditions [43].

1.4 Research goals and thesis organization

So far, several research groups in this field have presented different techniques to achieve the comb operation in THz QCLs. M. Rosch and J. Faist. et al from ETH presented a THz QCL, with three different active regions in an effort to extend the band-width of the gain profile [44]. The ETH design achieved an ultra-broad lasing spectrum, spanning 1.64 THz to 3.35 THz, however, it could not sustain stable comb operation across these frequencies due to the dispersion effect. D. Burghoff, and Q. Hu. et al from MIT demonstrated a novel waveguide equipped with a chirped DBR to compensate for the dispersion effect inside a THz QCL. With the help of the shifted wave interference Fourier-transform (SWIFT) spectrum, stable comb operation was observed from the 3.3 THz through to 3.8 THz [45], however, the operation bandwidth was limited due to the gain medium of that active region design.

Therefore, to properly realize a broad-band comb operation in a THz QCL device, we need to focus on optimizing and improving both the active region and waveguide design. The goal of this thesis is to design a THz QCL that can achieve comb operation between 2 THz and 4 THz. The project can be divided into three sections-

1. Theoretical modelling and design of a THz QCL active region with broadband gain

spectrum

2. Theoretical modelling and design of a waveguide that can compensate cold cavity dispersion, followed by design optimization to achieve octave frequency band operation.

3. Develop processes for device fabrication and, ultimately, demonstrate a THz QCL devices with good lasing performance.

The thesis is organized as follow,

Chapter 2 proposes new active region designs for THz QCL technologies with broadband gain profiles based on heterogeneous structure, using the rate equation model.

Chapter 3 introduces a 1D model (using Matlab) and a 3D model (using COMSOL) to investigate the chirped DBR for waveguide dispersion compensation.

Chapter 4 demonstrates the ability of our new chirped DBR waveguide design to achieve GVD within a broad frequency band.

Chapter 5 describes various achievements in device growth and fabrication. Development of an experimental setup for comb operation characterization. Subsequent device characterization results are also discussed. Preliminary experimental results of a THz QCL frequency comb device is presented.

Chapter 6 a conclusion.

Chapter 2

Active Region Design of THz QCLs with Broad-band Gain Profile

The fundamental requirements of active region design for broad-band comb THz QCLs are twofold. They include: 1. A broad lasing frequency band that provides a sufficient number of lasing modes within it to be phase-locked. 2. A relatively 'flat-top' shaped gain curve for the frequency band of interest, minimizing gain-induced GVD among the lasing modes, which would otherwise inhibit comb formation inside the cavity. In this chapter, the modeling for the THz QCL active region is presented.

2.1 Rate equation model basics

The rate equation model is an efficient and sufficiently accurate method for simulating the electrical and optical performance of a THz QCLs. Since QCLs are comprised of a series of repeated modules in the active region, it is possible and convenient to investigate the performance of the entire active region by applying the rate equation model to just two adjacent modules. A system of ordinary differential equations is formed to describe the changing rate of the carrier population (electrons) in each energy state as electrons move through multiple transition channels. By solving the rate equations in a steady state (where the carrier population in each state is stable), one can obtain the population of carriers in each state and the transition rate between any two of them. THz QCL performance (threshold current, optical gain, etc.) can then be predicted.

The general form of the rate equation in our model can be written as

$$\frac{d\rho_i(t)}{dt} = -\frac{\rho_i(t)}{\tau_i} + \sum_j \frac{\rho_j(t)}{\tau_{j\to i}} \tag{2.1}$$

where ρ and τ are the number of carriers and the carrier lifetime in one state, respectively, and the index i and j refer to two different states. The total lifetime of state i, is ${\tau_i}^{-1} = \sum_{i\neq j} {\tau_{i\to j}}^{-1}$, which expresses the transition rate of electrons from state i to all other states by including all intersubband transition mechanisms discussed in [46] (LO-phonon scattering [47], ion impurity scattering [48][49], the interface roughness scattering, and the dephasing time [50]).

Appling Equation 2.1 to the energy states in the conduction band of a THz QCL's active region, one can generate a group of differential equations that describes carrier transport channels connecting all energy states, as well as scattering times based on different mechanisms. As an example, Figure 2.1(a) shows both the calculated energy states in the conduction band and the corresponding moduli squared wavefunctions of THz QCL active region, where the corresponding schematic diagram of the rate equation configuration is presented in Figure 2.1(b).

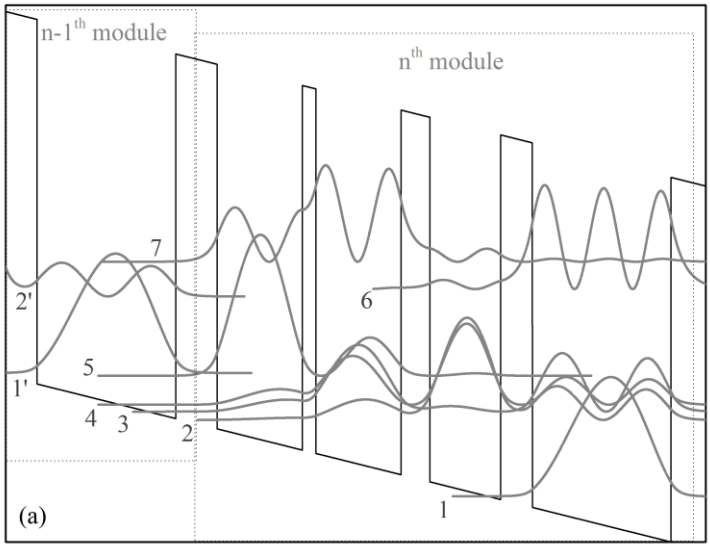

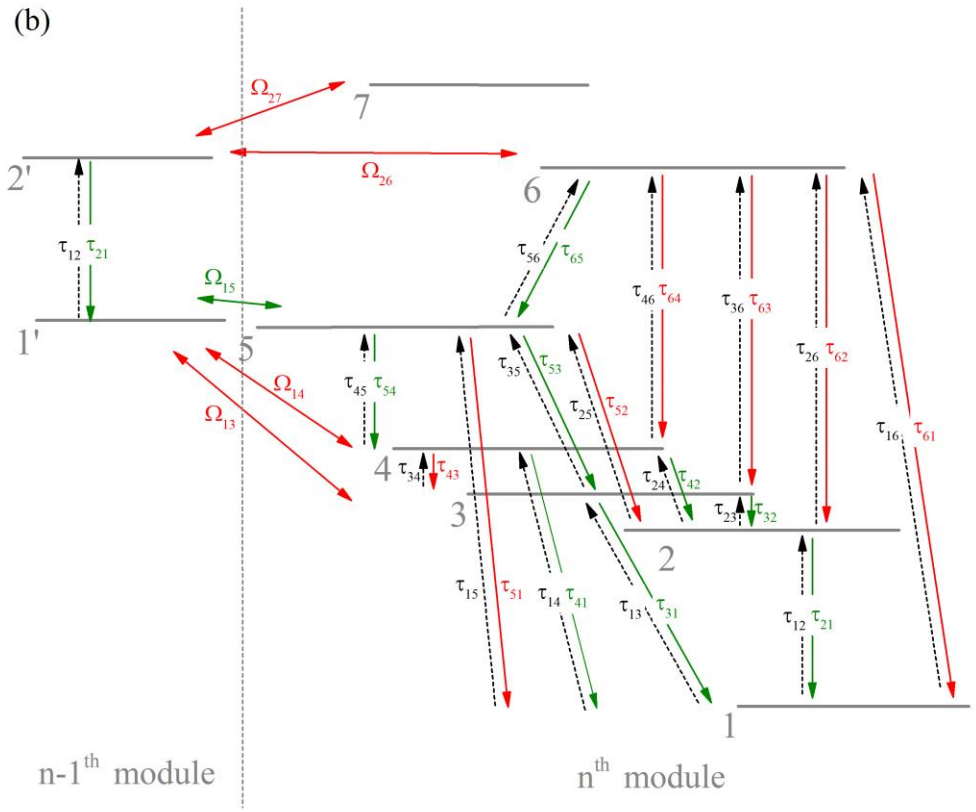

Figure 2.1 (a) An example of a calculated conduction band diagram and the normalized wave-functions of a THz QCL active region. (b) Schematic diagram of the transition channels described by the rate equation model, which correspond to the energy states in (a). The energy states within each module are labeled in energy ascending order 1 to 7. The solid lines show the forward scatterings, while the dashed lines indicate the backward scatterings. Ω_{ij} are the coupling between two states i and j. The green lines indicate the correct carrier injection and extraction paths, while the red lines show the wrong injection and extraction path in each module. State 5 is the upper lasing state, while 4 and 3 are the double lower lasing states.

Here, we assumed that the injection barrier between two adjacent modules is thick enough, and as a result, the carriers flowing across them are based on tunneling only. Based on the schematic shown in Figure 2.1(b), the rate equations can be written in the following matrix format for the steady state,

$$\begin{pmatrix} -\tau_1^{-1} - T_1^{-1} & \tau_{21}^{-1} + T_{21}^{-1} & \tau_{31}^{-1} + T_{31}^{-1} & \tau_{41}^{-1} + T_{41}^{-1} & \tau_{51}^{-1} + T_{51}^{-1} & \tau_{61}^{-1} + T_{61}^{-1} & \tau_{71}^{-1} + T_{71}^{-1} \\ \tau_{12}^{-1} + T_{12}^{-1} & -\tau_2^{-1} - T_2^{-1} & \tau_{32}^{-1} + T_{32}^{-1} & \tau_{42}^{-1} + T_{42}^{-1} & \tau_{52}^{-1} + T_{52}^{-1} & \tau_{62}^{-1} + T_{62}^{-1} & \tau_{72}^{-1} + T_{72}^{-1} \\ \tau_{13}^{-1} + T_{13}^{-1} & \tau_{23}^{-1} + T_{23}^{-1} & -\tau_3^{-1} - T_3^{-1} & \tau_{43}^{-1} + T_{43}^{-1} & \tau_{53}^{-1} + T_{53}^{-1} & \tau_{63}^{-1} + T_{63}^{-1} & \tau_{73}^{-1} + T_{73}^{-1} \\ \tau_{14}^{-1} + T_{14}^{-1} & \tau_{24}^{-1} + T_{24}^{-1} & \tau_{34}^{-1} + T_{34}^{-1} & -\tau_4^{-1} - T_4^{-1} & \tau_{54}^{-1} + T_{54}^{-1} & \tau_{64}^{-1} + T_{64}^{-1} & \tau_{74}^{-1} + T_{74}^{-1} \\ \tau_{15}^{-1} + T_{15}^{-1} & \tau_{25}^{-1} + T_{25}^{-1} & \tau_{35}^{-1} + T_{35}^{-1} & \tau_{45}^{-1} + T_{45}^{-1} & -\tau_5^{-1} - T_5^{-1} & \tau_{65}^{-1} + T_{65}^{-1} & \tau_{75}^{-1} + T_{75}^{-1} \\ \tau_{16}^{-1} + T_{16}^{-1} & \tau_{26}^{-1} + T_{26}^{-1} & \tau_{36}^{-1} + T_{36}^{-1} & \tau_{46}^{-1} + T_{46}^{-1} & \tau_{56}^{-1} + T_{56}^{-1} & -\tau_6^{-1} - T_6^{-1} & \tau_{76}^{-1} + T_{76}^{-1} \\ \tau_{17}^{-1} + T_{17}^{-1} & \tau_{27}^{-1} + T_{27}^{-1} & \tau_{37}^{-1} + T_{37}^{-1} & \tau_{47}^{-1} + T_{47}^{-1} & \tau_{57}^{-1} + T_{57}^{-1} & \tau_{67}^{-1} + T_{67}^{-1} & -\tau_7^{-1} - T_7^{-1} \end{pmatrix} \times \begin{pmatrix} \rho_1 \\ \rho_2 \\ \rho_3 \\ \rho_4 \\ \rho_5 \\ \rho_6 \\ \rho_7 \end{pmatrix} = \begin{pmatrix} 0 \\ 0 \\ 0 \\ 0 \\ 0 \\ 0 \\ 0 \end{pmatrix}$$

(2.2)

where τ_{ij} is the intersubband scattering time between states i and j in one module, T_{ij} is the tunneling time between states i and j when they are not in the same module. The tunneling time, T_{ij} represents the time for carriers to tunnel from level i of the current module (n^{th} module) to the level j of the next adjacent module ($n+1^{th}$ module) and to level j of the previous adjacent module ($n-1^{th}$ module), such that

$$T_{ij}^{-1} = T_{in \to jn+1}^{-1} + T_{in \to jn-1}^{-1}$$

(2.3)

Second order tunneling between states *i* and *j* was also assumed, in which the rate of tunneling is dependent on the distribution of carriers in each state [51][52]. The tunneling time can be calculated as follows:

$$T^{-1} = {T_{RL}}^{-1} + {T_{LR}}^{-1}$$

(2.4)

where T_{RL} and T_{LR} represent the different tunneling times between two states, including the reversed directions, and which are determined by the detuning the energy between the two levels (Δ_{LR}). In the case of $\Delta_{LR} > 0$, all electrons in the left subband (left state) can flow to the right subband (right state), while the electrons at the bottom of the right subband (with the energy levels lower than that of the bottom of left subband) cannot flow back to the left subband. Only the hot electrons in the right subband with higher energy have a chance to flow back to the left subband, as shown in the Figure 2.2.

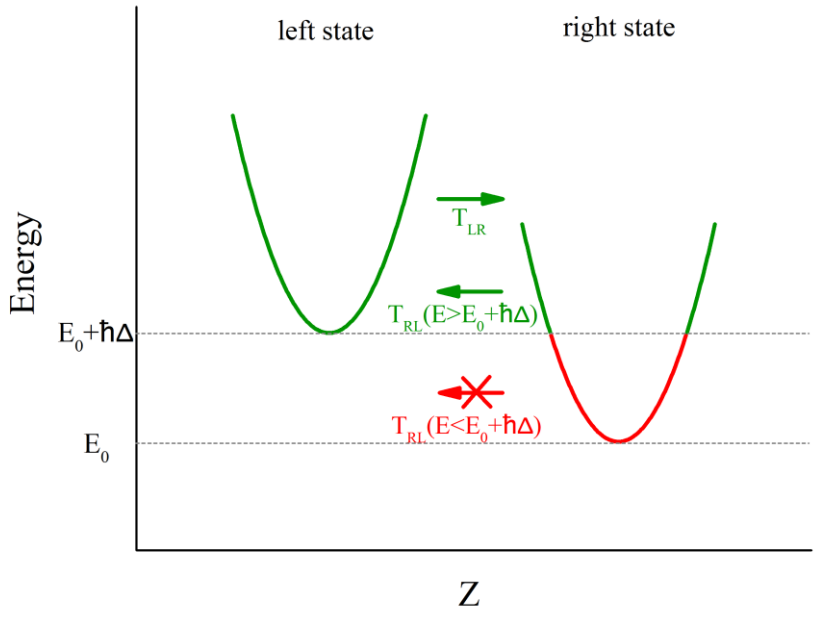

Figure 2.2 An example of tunneling cases between two states while considering the distribution of electrons on each state. In this case, the detuning energy is positive ($\hbar\Delta > 0$), all electrons from the left state can flow to the right state while only electrons with energy above $E_0 + \hbar\Delta$ can tunnel back from the right state to the left.

The second order tunneling time can be calculated by introducing an effective coupling parameter σ:

$$T_{\mathrm{RL}} = \frac{1 + \Delta_{\mathrm{RL}}^2 \tau_{\|\mathrm{RL}}^2}{2\Omega_{\mathrm{RL}}^2 \tau_{\|\mathrm{RL}}} \cdot \frac{1}{\sigma_{\mathrm{RL}}}$$

$$T_{\mathrm{LR}} = \frac{1 + \Delta_{\mathrm{LR}}^2 \tau_{\|\mathrm{RL}}^2}{2\Omega_{\mathrm{LR}}^2 \tau_{\|\mathrm{RL}}} \cdot \frac{1}{\sigma_{\mathrm{LR}}} \qquad (2.5\text{-}2.6)$$

where $\tau_{\|\mathrm{RL}}$ is the pure dephasing time between two states. The effective coupling parameter σ can be explained by a function of detuning energy and the distribution of the electrons in two states [53],

$$\sigma_{\mathrm{RL}} = \Theta(\Delta_{\mathrm{RL}}) + \Theta(-\Delta_{\mathrm{RL}}) N_{\mathrm{R}}^{-1} D_{\epsilon} \int_{\hbar\Delta_{\mathrm{RL}}}^{\infty} f_{\mathrm{R}}(\epsilon) d\epsilon$$

$$\sigma_{\mathrm{LR}} = \Theta(\Delta_{\mathrm{LR}}) + \Theta(-\Delta_{\mathrm{LR}}) N_L^{-1} D_\epsilon \int_{\hbar\Delta_{\mathrm{RL}}}^{\infty} f_{\mathrm{L}}(\epsilon) d\epsilon$$

$$\Delta_{\mathrm{RL}} = -\Delta_{\mathrm{LR}}$$

(2.7-2.9)

where Θ is the Heaviside step function. D_ϵ is the density of states, and N_{R} and N_{L} are the total population of carriers in the right and left states, which can be calculated as follows:

$$N_{\mathrm{R}} = D_\epsilon \int_0^{\infty} f_{\mathrm{R}}(\epsilon) d\epsilon$$

$$N_{\mathrm{L}} = D_\epsilon \int_0^{\infty} f_{\mathrm{L}}(\epsilon) d\epsilon$$

(2.10-2.11)

where, in Fermi-Dirac distribution $f(\epsilon) = 1/(1 + \exp(\epsilon/(k_{\mathrm{B}}T)))$, the temperature T is the combination of lattice and electron temperature ($T = T_{\mathrm{lattice}} + T_{\mathrm{electron}}$. For simplicity, instead of using a self-consistent model to calculate the electron temperature of each subband, we use $T_{\mathrm{electron}} = 100$ K for all subbands in the second order tunneling time calculation.

After solving the rate equation matrix Equation 2.2, the current density between any two states, i and j, can be determined with the calculated carrier populations, ρ_i and ρ_j, using a second order current density model:

$$J_{\mathrm{ij}} = \frac{2\Omega_{\mathrm{ij}}\tau_{\|\mathrm{ij}}}{1 + \Delta_{\mathrm{ij}}^2\tau_{\|\mathrm{ij}}^2}(\overline{\Omega_{\mathrm{ij}}}\rho_{\mathrm{i}} - \overline{\Omega_{\mathrm{ji}}}\rho_{\mathrm{j}})$$

(2.12)

where $\overline{\Omega_{\mathrm{ij}}}$ and $\overline{\Omega_{\mathrm{ji}}}$ are the effective coupling coefficients that describe the different coupling strength from states i to j, and from j to i. By adding up the current density of each channel, the total current density of the model was calculated as follows:

$$J = \sum_{\mathrm{i}=1}^{N}\sum_{\mathrm{j}=1}^{N} \frac{2\Omega_{\mathrm{ij}}\tau_{\|\mathrm{ij}}}{1 + \Delta_{\mathrm{ij}}^2\tau_{\|\mathrm{ij}}^2}(\overline{\Omega_{\mathrm{ij}}}\rho_{\mathrm{i}} - \overline{\Omega_{\mathrm{ji}}}\rho_{\mathrm{j}})$$

(2.13)

where N is the number of states included in the model. In most designs, carrier transport channels that involve higher energy states (e.g. J_{ij} with i, j>7) do not contribute

significantly to carrier transport due to the limited number of carriers distributed in those states. They do, however, occupy the same amount of time and resources in simulation. Thus, in the present case, only the lowest 7 states in one module are considered in the model.

The optical gain of our designed structure can be estimated by multiplying the dipole momentum, calculated from the wavefunctions of two lasing states, and their respective carrier population inversions by using Fermi's golden rule [54]:

$$\alpha(\hbar\omega) = \frac{\pi e^2}{n_r c \varepsilon_0 (m^*)^2 \omega} \frac{2}{V} \sum_{ki} \sum_{kj} \left|\hat{e} \cdot P_{ij}\right|^2 \delta(E_i - E_j - \hbar\omega)(f_i - f_j) \tag{2.14}$$

where ω is the frequency of the optical field, n_r is the refractive index of the material, ε_0 is the permittivity in vacuum, V is the volume of the active region interacting with the optical field, and P_{ij} is the momentum matrix element, and c is the speed of light. For simplicity, the delta function in Equation 2.14 is then replaced by a Lorentzian function, which yields:

$$\alpha(\hbar\omega) = \frac{\pi e^2}{n_r c \varepsilon_0 (m^*)^2 \omega} \frac{2}{V} \sum_{ki} \sum_{kj} \left|\hat{e} \cdot P_{ij}\right|^2 \frac{\Gamma/2}{(\omega_{ij} - \hbar\omega)^2 + (\Gamma/2)^2} (f_i - f_j) \tag{2.15}$$

where Γ represents the full-width-half-maximum (FWHM) of the Lorentzian function. In the BTC design discussed in this thesis, we use a Γ of 1 meV to estimate the broadening of the lasing frequencies, which has been proved to be reasonable [44].

2.2 Numerical simulation of broad-band THz QCLs

To investigate the usefulness of our rate equation model for broadband THz QCLs design, we applied it to an existing broad-band THz QCL design available in the literature [44] [55]. The design has an ultra-broad gain bandwidth from 1.64 THz to 3.35 THz, which is achieved using a heterogeneous structure comprised of three sections, each with a different

active region (with central frequencies at 2.9 THz, 2.6 THz, and 2.3 THz), in one THz QCL device. Each active region originates from a BTC design [56], but is re-modified to include lasing frequencies that cover a broader frequency bandwidth and a lower doping concentration to achieve CW operation. BTC design comprises multiple lower states that form a small mini-band, which helps extend the gain profile bandwidth, and makes the BTC scheme one of the most promising candidates for developing active regions that can effectively support comb operation.

The growth materials for all three BTC active regions are based on GaAs/$Al_xGa_{1-x}As$ with an aluminum fraction of 15% (x=0.15). The layer sequences for each of the three active regions are (starting from the injection barrier, in Angstrom) **55**/110/**18**/115/**38**/94/**42**/184 for the 2.9 THz active region (Section A); **55**/113/**18**/113/**38**/94/**42**/184 for the 2.6 THz active region (Section B); **55**/120/**18**/105/**38**/94/**42**/184 for the 2.3 THz active region (Section C), where bold font indicates the barriers. The phonon wells (184 Å) in all three active regions are homogeneously Si-doped to $n_s=3.1\times10^{10}$ cm^{-2}.

Figure 2.3 shows the calculated conduction band diagram and the moduli wavefunctions for each of the three active regions at the alignment electric field for each, which is defined as the electric field at which the injection state of the module n-1 (state 1' in green) is aligned with the upper lasing state of module n (state 5 in red). The wavefunction of the lower states (states 2,3, and 4 in blue) spans the entire length of one module and generates a mini-band. This architecture has several advantages:1. The large spatial difference between the upper lasing state and the injection state (state 1) is separated by a mini-band region, which reduces the wrong direct coupling between them, and, thus, helps retain high population inversion between upper and lower lasing states. 2. The alignment condition of the phonon assist carriers' depopulation from the mini-band to the injection state is relaxed compared to that from a single extraction state. 3. The mini-band formed lower state provides an inherent broad gain profile.

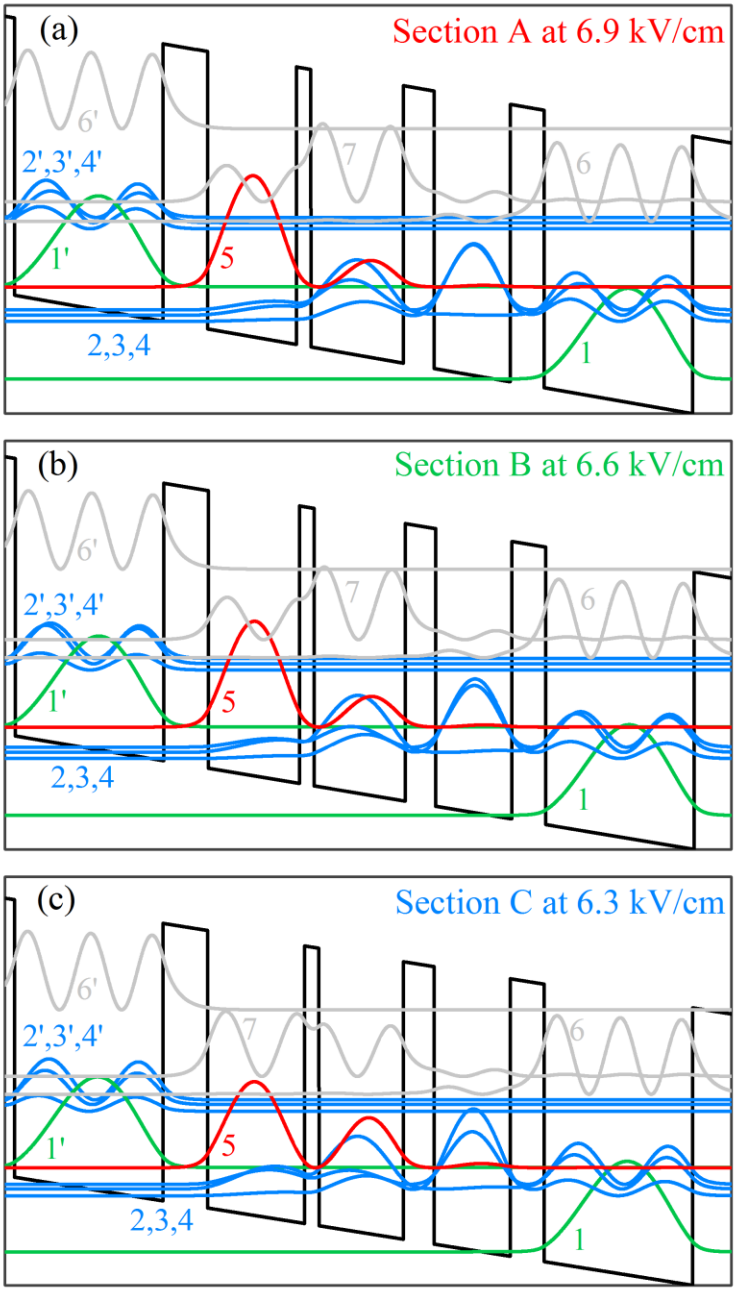

Figure 2.3 Conduction band diagrams and the moduli squared wavefunctions for Section A, B, and C active regions ((a), (b), and (c), respectively), showing the alignment electric field for each (6.9 kV/cm for Section A, 6.6 kV/cm for Section B, and 6.3 kV/cm for Section C).

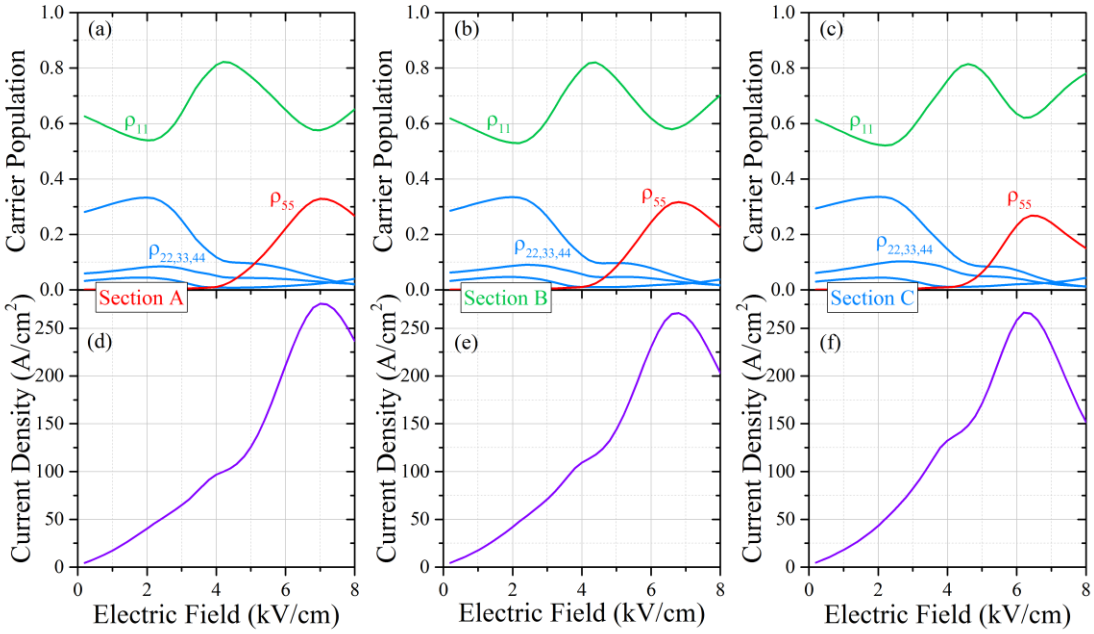

Figure 2.4 (a), (b), and (c) Calculated carrier populations in the lowest five states of the three different active regions, Section A, B, and C, respectively. (d), (e), and (f) Calculated JV curves for the three active regions, respectively. All simulations are conducted under non-lasing conditions and at a lattice-temperature of 25 K.

Figure 2.4 (a), (b), and (c) show the calculated carrier populations in the five lowest energy states for the three active regions in non-lasing condition and at a lattice temperature of 25 K. Carrier populations in parasitic states (state 6 and 7) are negligible at low temperature, thus are not plotted. It is clear that all three active regions have quite similar subband carrier population dependence on the electric field due to their similarities in quantum design. The population of the injection state, ρ_{11}, recovers from the wrong extraction channel from injection state (state 1) to mini-band (states 2, 3, and 4) at ~ 2 kV/cm, and reduces again while approaching the alignment electric field. Meanwhile, the upper lasing state (5) begin to be populated through resonant tunneling T_{15}, and the carrier populations in the mini-band (states 2,3, and 4) drop simultaneously through phonon assisted carrier relaxation, causing a population inversion between the upper lasing state and the lower mini-band. Based carrier population data for each state, the JV curves for all three active regions are calculated under non-lasing condition, as shown in Figure 2.4 (d),

(e), and (f). The three active regions exhibit consistent JV curve shape, with a relative close negative differential resistance (NDR) electric field (~6.5 kV/cm) and maximum current density (~250 A/cm^2), which benefits operation of the heterogeneous active region design. To understand the importance of this benefit we need only compare single active region designs against heterogeneous active region designs. Heterogeneous schemes are much more challenging to develop, largely because the electric field for each active region is controlled by the current passing through them. Thus, combining multiple active regions with relatively different JV characteristics in a single device may prevent the sections from simultaneously reaching their alignment electric field, and even create problems in the electric field domain across the heterogeneous structure [57][58].

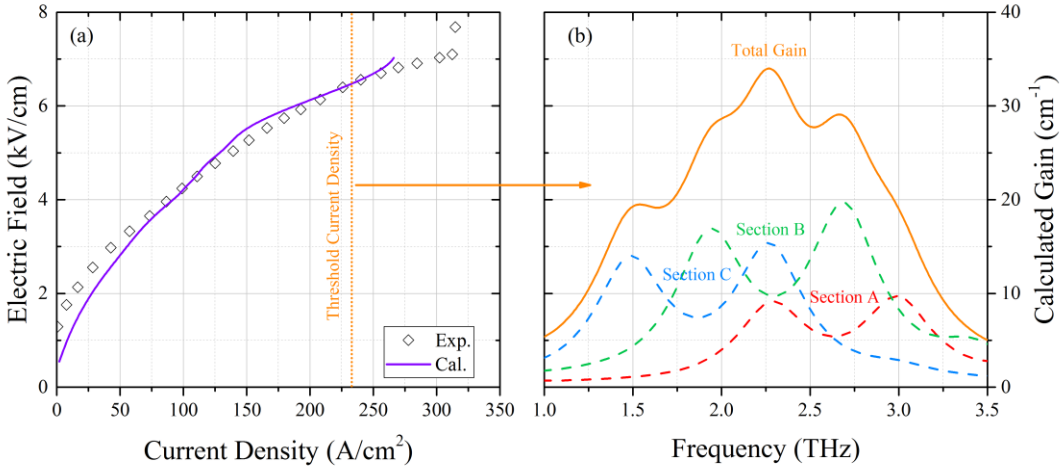

Figure 2.5 (a) Calculated JV curve across the heterogeneous active region (purple curve), and the experimental JV data extracted from [44]. (b) Calculated total gain profile of the heterogeneous active region under the threshold condition.

To further investigate the operation of the heterogeneous active region design, we calculated the overall JV curve for the entire active region by stacking the electric fields across each section of the active region under the same current injection, at a temperature of 25 K, and according to the thickness of each section in the device (40 repeats of Section A, 80 repeats of Section B, and 80 repeats of Section C), as shown in Figure 2.5(a). For comparison, the experimental JV curve for this heterogeneous active region is also plotted in the same figure. According to the light-current-voltage result in [44], the threshold current density of the published heterogeneous THz QCL is around 226 A/cm^2 at a

temperature of 25 K (orange line, Fig. 2.5 (a)). Although we are using a rather simple method to calculate the overall JV curve, which doesn't consider the electric field domain between different active regions, the calculated curve (purple curve) can accurately predict the trend of the experimental JV data (void diamonds) below the threshold condition. In this case, we can roughly estimate the total gain profile at the threshold condition by stacking gain profiles of independent active regions at the threshold current density. Since the lateral distribution of the electric field in a metal-metal waveguide is close to uniform [35], the contribution to the optical gain from each section of active region is estimated to be approximately proportional to the number of repeats for each section. Thus, the overall gain profile of this heterogeneous structure is calculated thus:

$$G_{\mathrm{tot}}(\omega) = \sum_{i=1}^{3} \Gamma_{\mathrm{i}} G_{\mathrm{i}}(\omega)$$

$$\Gamma_{\mathrm{i}} = \frac{N_{\mathrm{i}}}{\sum_{\mathrm{i}=1}^{3} N_{\mathrm{i}}}$$

(2.18-2.19)

where N_{i} is the number of repeats for the i^{th} section of the active region, $G_{\mathrm{i}}(\omega)$ is the gain profile of each individual active region calculated from Equation 2.17 with a broadening coefficient of $\Gamma/2 = 1\, meV$. Figure 2.5(b) shows the calculated total gain of the heterogeneous structure under threshold condition at temperature 25 K (orange curve), which predicts a broad frequency band from 1.7 THz to 3.0 THz (FWMH). The contribution of gain profiles from the three sections' active regions are plotted with dashed curves, demonstrating a central frequency of 2.6 THz for Section A, 2.3 THz for Section B, and 1.9 THz for Section C. For each active region gain calculation, we consider all the lasing transitions from the upper lasing state (state 5) to the lower states in the mini-band (states 2, 3, and 4). We observed that the transitions 5→4 and 5→3 dominate over the transition 5→2 at the electric field close to and above the threshold condition due to their relatively larger oscillation strengths [59] (f_{54}~0.26, f_{53}~0.26, and f_{52}~0.04 for Section A; f_{54}~0.26, f_{53}~0.31, and f_{52}~0.05 for Section B; f_{54}~0.32, f_{53}~0.42, and f_{52}~0.03 for Section C), which generate double peaks in their gain profile as a result. As expected, the inherent broad double peak gain profile from each active region benefits device operation, allowing it to achieve the target ultra-broad and continuous total gain spectrum.

2.3 Active region design of THz QCLs with ultra-broad bandwidth from 2-4 THz

As discussed in Chapter 1, in order to realize ultra-broad band comb operation in a THz QCL device, we must optimize both active region design, based on a heterogeneous structure that can achieve a broad-band gain profile with less gain-induced dispersion, and the waveguide design, incorporating a chirped DBR to reduce the cold cavity dispersion. However, the lower confinement factor of the metal-metal waveguides at the low frequency band (< 2 THz) introduces enormous difficulties to the design of novel chirped DBR waveguides (will be discussed in Chapter 4). Therefore, in this section, we focus on the design of a new heterogeneous active region structure to lasing frequencies between 2 and 4 THz.

2.3.1 Heterogeneous active region based on BTC transition

We re-designed the heterogeneous structure described in section 2.2 to include three different active regions based on a similar material system used in the original design, namely GaAs/$Al_{0.15}Ga_{0.85}As$. The layer sequences of the three active regions are (starting from the injection barrier, in Angstrom): **55**/103/**18**/120/**40**/94/**42**/184 for 3.6 THz (central frequency) active region (Section A); **55**/106/**18**/117/**39**/93/**42**/184 for 3.1 THz (central frequency) active region (Section B); and **55**/111/**18**/112/**38**/94/**42**/184 for 2.5 THz (central frequency) active region (Section C), where the bold font indicates the barriers. The phonon wells (184 Å) in all three active regions are homogeneously Si-doped to $n_s=3.1\times10^{10}$ cm^{-2} as well. In order to balance the peak gain across the entire target frequency range (2-4 THz), we redistributed the number of repeats for each active region across the entire heterogeneous structure according to the following composition: 40%:30%:30% (Section A: Section B: Section C).

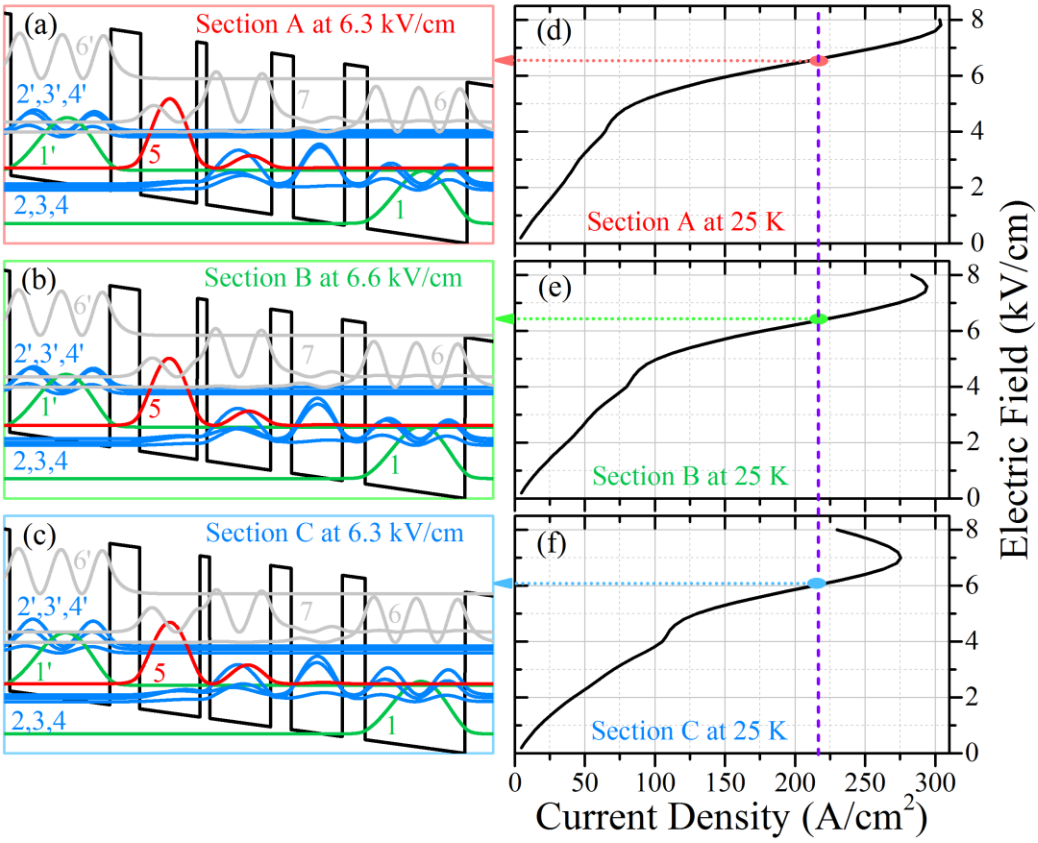

Figure 2.6 (a), (b), and (c) Conduction band diagrams and the corresponding moduli squared wavefunctions of the three active regions (Sections A, B, and C) at the near threshold electric field for each (6.3 kV/cm for Section A, 6.6 kV/cm for Section B, and 6.3 kV/cm for Section C, respectively). (d), (e), and (f) Calculated JV curves for three active regions, respectively. All simulations consider a lattice temperature of 25 K and non-lasing condition.

In order to reduce interference caused by gain-induced dispersion of the electric field at high injection conditions, we optimized the gain profile of our heterogeneous structure at the threshold region. For simplicity, we supposed the optical loss (including the waveguide loss and mirror loss) for the new device is consistent to the original heterogeneous structure discussed in Figure 2.5(b), which means, the new design has the same threshold gain of (~30 cm^{-1}). After calculating the gain profiles at different injected currents (where the peak of the gain increases with the injected current), we estimated the estimated threshold current density of the design to be at ~220 A/cm^2.

Figure 2.6(a), (b), and (c) shows the calculated conduction band diagrams and the moduli wavefunctions for the three sections of active regions at the estimated threshold condition. Similar to the heterogeneous structure presented in section 2.2, the new active region designs are based on BTC transitions, however, the energy spacing between the upper lasing state (state 5) and the lower lasing mini-bands (states 2, 3, and 4) are adjusted to the broader range of target lasing frequencies, between 2 THz and 4 THz. Also, the oscillation strengths of transitions 5→4 and 5→3 have been optimized to be comparable with each other at near threshold condition (f_{54}~0.23 and f_{53}~0.22 for Section A; f_{54}~0.25 and f_{53}~0.23 for Section B; f_{54}~0.28 and f_{53}~0.29 for Section C), which results in a balanced double peak gain profile and further improved the broad gain bandwidth.

The JV curves corresponding to our three active regions (at a lattice-temperature of 25 K) are plotted in Figure 2.6(d), (e), and (f). As expected, the three JV curves show similar trends across the entire electric field. At the estimated threshold current injection of 220 A/cm^2, the three active regions show very similar drops in electric field (6.3 kV/cm for Section A, 6.6 kV/cm for Section B, and 6.3 kV/cm for Section C), which not only prevents the formation of an electric field domain across the different active regions, but also benefits the simultaneous operation among the three active regions such that they reach the lasing threshold at same time. Finally, we predicted an overall JV curve for our new heterogeneous structure designs using an approach similar to that discussed in Section 2.2 (shown in Figure 2.7).

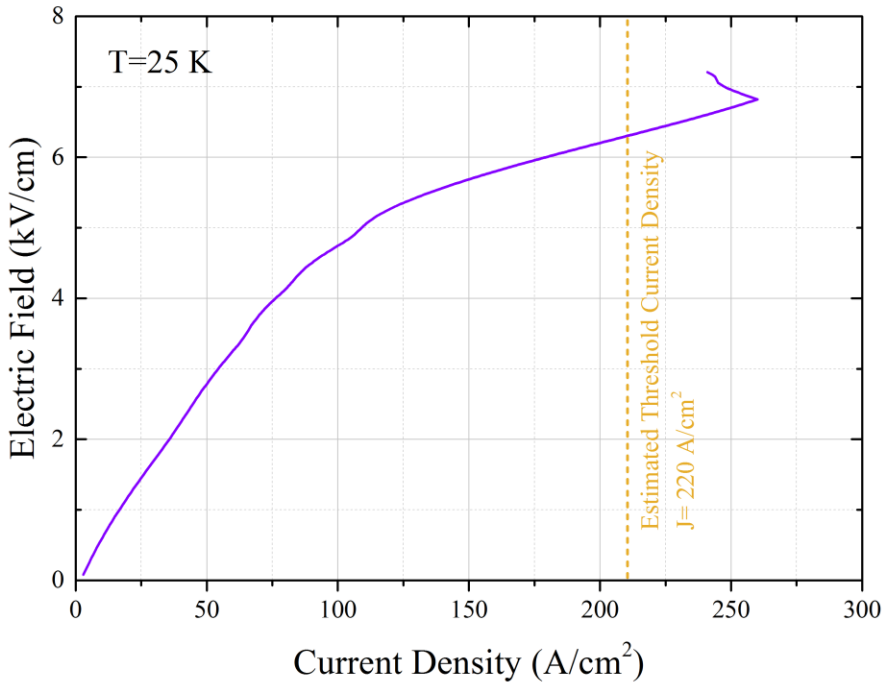

Figure 2.7 Calculated JV curve of the heterogeneous active region (purple curve). The orange dashed line marks the estimated threshold current.

The overall gain profile of the heterogeneous structure at the estimated threshold current density (at a temperature of 25 K) was also calculated, as shown in Figure 2.8. The resulting ultra-broad total gain profile (orange curve) includes contributions from three different active regions with central frequencies of 3.6 THz (Section A, red dashed curve), 3.1 THz (Section B, green dashed curve), and 2.6 THz (Section C, blue dashed curve). The FWHM of the total gain profile is approximately 1.7 THz (from 2.2 THz to 3.9 THz). The frequency bandwidth of the gain profile will be further extended at higher current-injection above the threshold condition, however, the shape of it cannot be accurately predicted with the current rate equation model at strong lasing conditions.

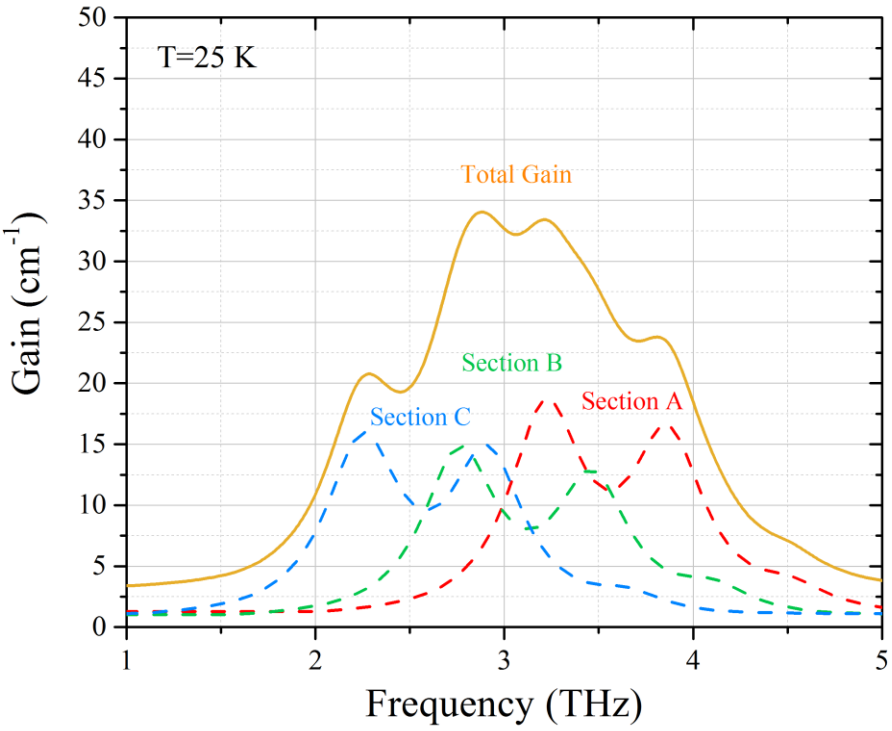

Figure 2.8 Calculated total gain profile of the new designed heterogeneous active region design under the threshold condition and at a lattice-temperature of 25 K. The dashed curves show the contribution of the individual gain profile from each section.

The finalized design parameters of our heterogeneous structure based on three different BTC active regions, are provided in Table 2.1.

Table 2.1 Design parameters of heterogeneous structure based on BTC ($GaAs/Al_{0.15}Ga_{0.85}As$)

Layer Sequences (starting from injection barrier in Å, barriers in bold fonts)	**Doping Concentration (homogeneously in well of 184 Å)**	**Number of Repeating Modules**	**Central Frequency**	**Designed Bias at Threshold Condition**
55/103/**18**/120/**40**/94/**42**/184	3.1×10^{10} cm^{-2}	61	3.6 THz	6.3 kV/cm
55/106/**18**/117/**39**/93/**42**/184	3.1×10^{10} cm^{-2}	46	3.1 THz	6.6 kV/cm
55/111/**18**/112/**38**/94/**42**/184	3.1×10^{10} cm^{-2}	46	2.5 THz	6.3 kV/cm

2.3.2 Heterogeneous active region based on RP transition

Although the BTC active region can provide an inherently broad gain bandwidth at low temperatures, its performance (including the peak gain and the gain bandwidth) drops quickly in response to increases in operating temperature due to fast non-radiative carrier depopulation from the upper lasing state. This shortcoming is compounded when different active regions are stacked in a single heterogeneous structure, which extends the gain at the expense of reducing the original peak gain. However, high operating temperatures, especially ones that reach the liquid nitrogen temperature (77 K), are also important to THz QCLs comb operation. This is because THz QCLs can potentially be mounted in a continuous flow liquid nitrogen dewar, which benefits from significantly reduced environmental interference and, thus, greatly improved stability (particularly for comb operation) by comparison with traditional mounts inside a pulsed helium-recycling cryostat, which is exposed to intensive noise from mechanical vibration [60]. To achieve this goal, we focus on an existing active region design comprised of 3-well RP structures, which broke the world record for highest operating temperature in the world [32].

In order to compensate the relatively narrow gain bandwidth from RP active regions (compared to that of BTC active regions), we designed the second heterogeneous structure with four different active regions based on the GaAs/$Al_{0.15}Ga_{0.85}As$ material system. The layer sequences of the four active regions are (starting from the injection barrier, in Angstrom): **45**/88/**30**/83/**44**/159 for the 2.4 THz (central frequency) active region (Section A); **45**/87/**29**/84/**44**/159 for the 2.8 THz (central frequency) active region (Section B); **45**/85/**28**/83/**44**/159 for the 3.2 THz (central frequency) active region (Section C), and **45**/84/**28**/84/**44**/159 for the 3.6 THz (central frequency) active region (Section D), where the bold font indicates the barriers. The injection barrier (45 Å) in all four active regions are delta-doped with Si to $n_s=2\times10^{10}$ cm^{-2}. In order to balance the gain across the entire target frequency range (2-4 THz), we distributed the number of repeats for each active region in the whole heterogeneous structure according to the following composition: 30%:25%:25%:20% (Section A: Section B: Section C: Section D).

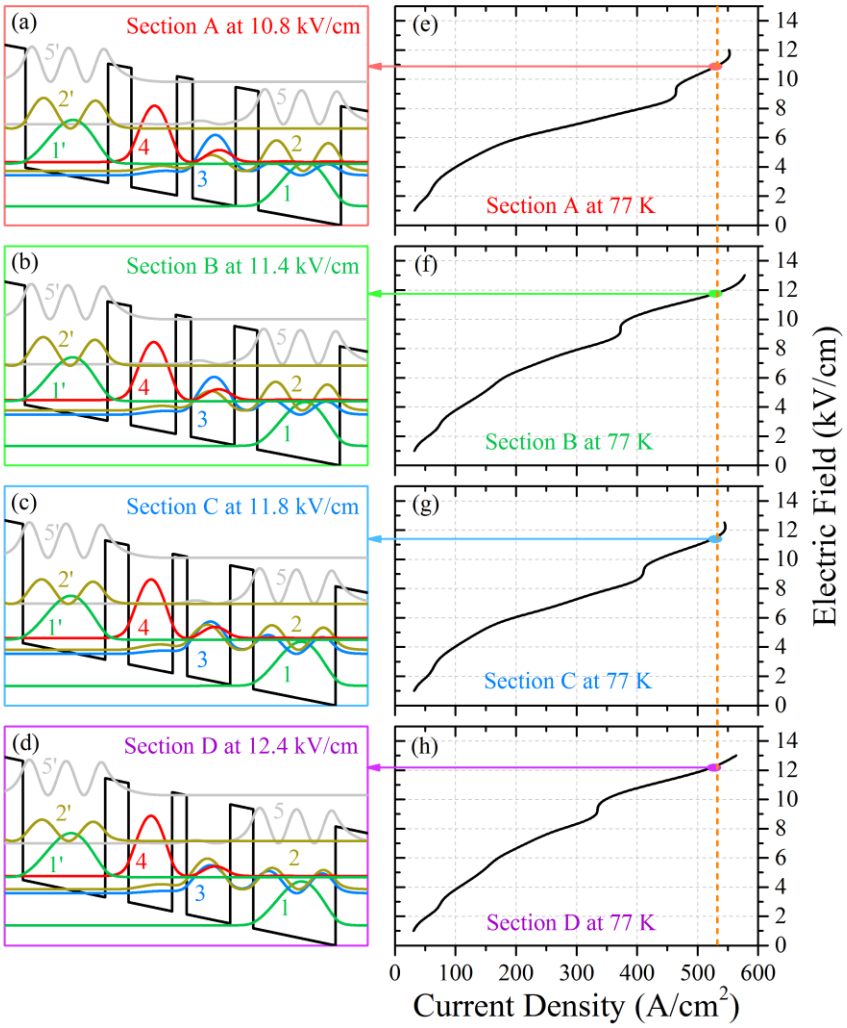

Figure 2.9 (a), (b), (c), and (d) Conduction band diagrams and the corresponding moduli squared wavefunctions of the four active regions (Sections A, B, C and D) at the near threshold electric field of each (10.8 kV/cm for Section A, 11.4 kV/cm for Section B, 11.8 kV/cm for Section C, and 12.4 kV/cm for Section D, respectively). (e), (f), (g) and (h) Calculated JV curves for the four active regions, respectively. All simulations are conducted under a lattice-temperature of 77 K and non-lasing condition.

For the same reasons discussed in section 2.3.1, the gain profile of this heterogeneous structure was optimized at threshold condition and the optical losses including the waveguide loss and the facet-mirror loss, was estimated to be around 30 cm^{-1} as well. The calculated threshold current density of this structure is at around 530 A/cm^2 as shown with the orange dashed line in Figure 2.9(e), (f), (g), and (h).

Figure 2.9(a), (b), (c) and (d) show the conduction band diagrams and corresponding moduli wavefunctions for the four active regions at the estimated threshold electric field. The four RP active regions show a similar large overlap between the mixed lower lasing state (state 3 in blue) and upper phonon state (state 2 in yellow), demonstrating fast carrier extraction from the lower lasing state. This is followed by a carefully designed downstream extraction phonon well, where the carriers are quickly relaxed to the injection state (state 1 in green) for the next module. In all four active regions, the transition 4→3 contributes marginally to the oscillator strength at the electric field close to and above the threshold condition, and since there is a large population inversion between these two states, the transition 4→3 provides the major contribution to the gain. As discussed in [61], a more diagonal design with lower oscillation strength (diagonal radiative transition) in a 3-well RP active region may sacrifice the current-carrying capacity through the lasing channel (4→3) and cause electric-field domain formation or even completely switch off the lasing transition. On the other hand, a too strong oscillation strength may increase threshold current density and prevent CW operation for comb THz QCLs. Therefore, we carefully controlled the lasing double wells of all four active regions to obtain moderate oscillation strengths with f_{43}~0.37 for Section A, f_{43}~0.36 for Section B, f_{43}~0.39 for Section C, and f_{43}~0.40 for Section D.

The calculated JV curves for the four active regions at a temperature of 77 K are plotted in Figure 2.9(d), (e), and (f). At the estimated threshold current injection of 530 A/cm^2, the four active regions show similar drops in electric fields (10.8 kV/cm for Section A, 11.4 kV/cm for Section B, 11.8 kV/cm for Section C, and 12.4 kV/cm for Section D). The first negative differential resistance region of the electric field (for all four active regions) occurs at ~9 kV/cm. This is due to the surpassing of alignment of energy state 1' (in previous module) and state 2, where the state 1' approaches alignment with state 4 and reaches the threshold condition. For the convenience of CW operation for our comb application, we also reduced the doping concentration in all four designs to decrease the threshold current density.

The overall gain profile of the heterogeneous structure at the estimated threshold

current density (at a lattice-temperature of 77 K) is shown in Figure 2.10. The ultra-broad total gain profile (orange curve) includes contributions from the four different active regions, with central frequencies of 2.4 THz (Section A, red dashed curve), 2.8 THz (Section B, green dashed curve), 3.2 THz (Section C, blue dashed curve), and 3.6 THz (Section D, purple dashed curve). The FWHM of the total gain profile is around 1.6 THz (from 2.2 THz to 3.8 THz).

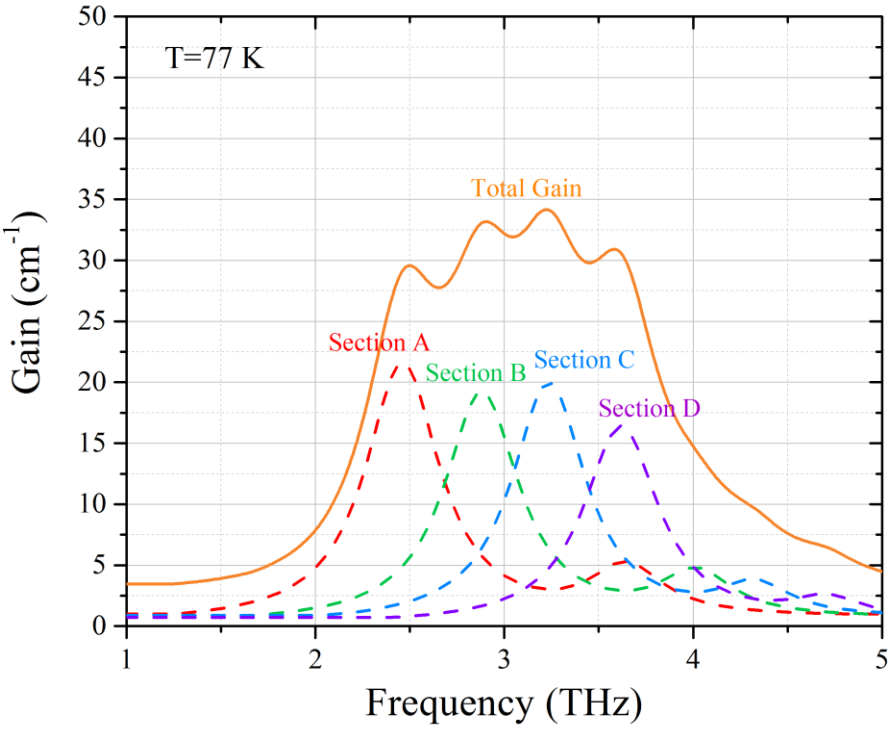

Figure 2.10 Calculated total gain profile of new designed heterogeneous active region based on four RP active regions at threshold condition and at a lattice temperature of 77 K. The dashed lines indicate the individual gain profile from each section.

The finalized design parameters of this heterogeneous structure based on four different RP active regions are show in Table 2.2.

Table 2.2 Design parameters of heterogeneous structure based on RP ($GaAs/Al_{0.15}Ga_{0.85}As$)

Layer Sequences (starting from injection barrier in Å, barriers in bold fonts)	Doping Concentration (delta doping at center of injection barrier)	Number of Repeating Modules	Central Frequency	Designed Bias at Threshold Condition
45/88/**30**/83/**44**/159	2×10^{10} cm^{-2}	67	2.4 THz	10.8 kV/cm
45/87/**29**/84/**44**/159	2×10^{10} cm^{-2}	56	2.8 THz	11.4 kV/cm
45/85/**28**/83/**44**/159	2×10^{10} cm^{-2}	57	3.2 THz	11.8 kV/cm
45/84/**28**/84/**44**/159	2×10^{10} cm^{-2}	45	3.6 THz	12.4 kV/cm

2.4 Summary

In this chapter, a rate equation model was presented as a tool for designing the broad-band active region to serve our comb THz QCL. The model was firstly applied to an existing heterogeneous structure design described in the literature, comprised of three different BTC active regions lasing from 1.64~3.35 THz at a lattice-temperature of 25 K. The model predictions showed good agreement with the JV characteristics and the gain profile of the previously published active region design.

A new heterogeneous structure with three different BTC active regions was designed to address a broader range of lasing frequencies, from 2~4 THz. The new design demonstrates similar temperature performance as the previously published heterogeneous structure (up to 25 K), but may improve the gain bandwidth at a different frequency region. A second heterogeneous structure was then designed, based on four different RP active regions. This second design targets the same lasing frequency band as our first (2~4 THz), but demonstrates greatly improved operating temperature performance (up to 77 K). This breakthrough in temperature performance may help the THz QCL achieve comb operation at the liquid nitrogen temperature. Both two new heterogeneous structures will be adopted for making the final THz frequency comb devices.

Chapter 3

Modeling of Chirped DBR Structures in THz QCLs

Frequency comb operation was first achieved in MIR quantum cascade lasers by Hugi and Faist et al. in 2012. Specifically, the Faist team used an active mode-locking technique to demonstrate broad-band comb (60 cm^{-1}) operation in a MIR QCL [62]. Compared to MIR QCLs, achieving comb operations in THz QCLs is much more challenging because their lasing frequencies are close to the reststrahlen band of the device material (GaAs/AlGaAs), where the EM wave couples to the lattice and causes strong GVD in the broad lasing frequency band. As a result, the GVD shifts the lasing mode frequencies inside the cavity and prohibiting formation of the frequency comb. To solve this problem, one effective strategy is to fabricate a chirped DBR mirror along THz QCL' metal-metal waveguide sidewall, which compensates the GVD caused by the rest of the un-chirped flat-ridge waveguide [45]. Much work has already been done to compensate the GVD in optical fiber lasers using chirped DBRs [63][64], however, the technique has yet to be properly adapted to THz QCLs due to the long wavelength of the EM waves and the non-uniform distribution of modes inside the metal-metal waveguide. In this chapter, we present a theoretical study on building models in support of chirped DBR structure designs. A 1D model based on the transfer matrix method is firstly demonstrated to reveal the fundamental behaviors and characteristics of chirped DBR structures. A more accurate, 3D model is then deployed using a COMSOL RF package to verify the 1D simulation results and to systematically investigate chirped DBR structures.

3.1 1D Modeling of chirped DBR structures based on the transfer matrix method

3.1.1 GVD of terahertz waves in GaAs material

The intensive dispersion of EM waves at the terahertz frequency range in GaAs based material is caused by strong coupling to the lattice at a frequency close to the reststrahlen region. The relation of the dispersion can be simply explained as follows [65]:

$$\varepsilon(\omega,T)=\varepsilon_{\infty}(T)+\frac{\omega_{\mathrm{TO}}^{2}(T)[\varepsilon_{0}(T)-\varepsilon_{\infty}(T)]}{\omega_{\mathrm{TO}}^{2}(T)-\omega^{2}+\mathrm{i}\gamma_{\mathrm{p}}\omega} \tag{3.1}$$

where ε_{∞} is the high frequency (optical) dielectric constant, ε_0 is the low frequency (optical) dielectric constant, ω_{TO} is transverse optical (TO) phonon energy, and γ_{p} is the damping coefficient. According to the equation above, at a frequency lower than $\omega_{\mathrm{TO}} \approx 8$ THz, where most published THz QCLs operate [24], the group velocity of the EM wave suffers significant GVD, as shown in Figure 3.1.

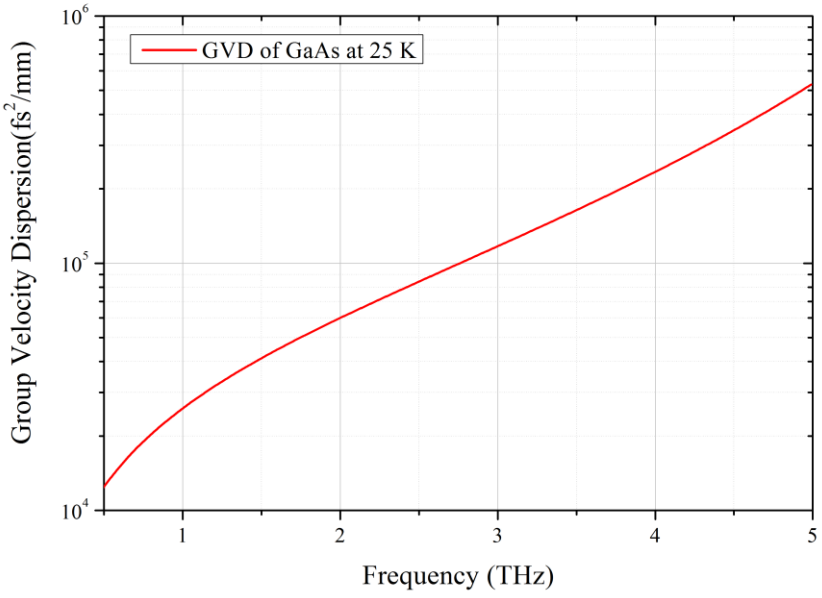

Figure 3.1 Calculated GVD in GaAs material at a temperature of 25 K and within a frequency range between 0.5 THz and 5 THz.

3.1.2 Transfer matrix method for chirped DBR structures

To overcome this dispersion, one strategy is to fabricate a chirped DBR along the ridge of the metal-metal waveguides. The period of the DBR tapers from a short one to a long one while its corrugation depth increases, as shown in Figure 3.2.

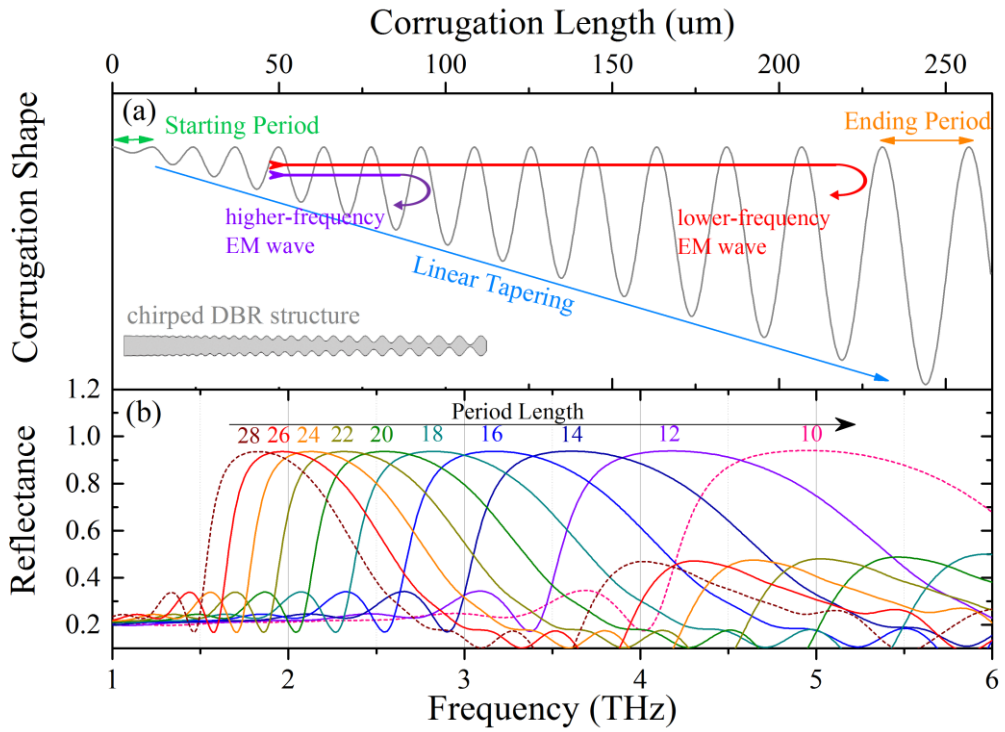

Figure 3.2 (a) Example of the corrugate shape of a chirped DBR structure. The period lengths of the sinusoidal shape gradually increase from left to right, while the corrugation depth tapers linearly from the starting period to the ending period. (b) The 1D simulation result of the relationship between the period length of sinusoidal shape and its frequency band of reflectance. (The simulations were made with structures that were similar to that in (a), however with a constant period length in the corrugation structure). The peak reflectance frequency shifts from 1.8 THz to 5 THz while the corrugation period length was shortened from 28 μm to 10 μm.

Considering a first order Bragg grating, the reflected wavelength is determined by the period of the perturbation such that [66]:

$$\lambda_i = 2n_{eff}\Lambda_i$$

(3.2)

where λ_i is the reflected wavelength in free space, n_{eff} is the effective index of the waveguide, and Λ_i is the length of corrugation period. In this case, the length of the starting and ending periods determine the upper and lower frequency reflection limit of the chirped DBR, as shown in Figure 3.2(b). Also, the shorter-wavelength waves which suffer stronger group delays are reflected closer to the starting (short) period, while longer- wavelength waves travel to the ending (long) period, as demonstrated in Figure 3.2(a). Through careful design of the distribution of the corrugated periods, the chirped DBR forces the EM waves with different frequencies to take an almost equal round trip travelling time, thereby compensating for the group delay dispersion.

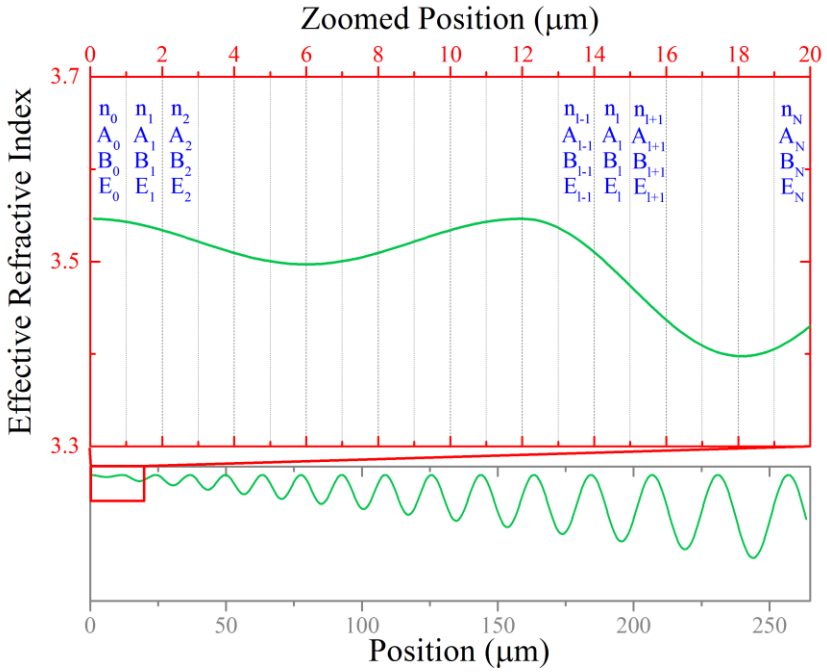

Figure 3.3 Schematic of a chirped DBR structure (bottom figure) and the zoomed region (top figure) of it. The structure is divided into multi-slices in the model using the transfer matrix method.

To understand the fundamental behaviors and to investigate the performance of chirped DBR structures, we built a simplified 1D model based on transfer matrix method [67]. In this model, the chirped DBR structure is divided into multiple tiny slices, and the optical parameters (e.g. refractive index) inside one individual slide are assumed to have constant value, as shown in Figure 3.3.

The electric field in each slide can be written as

$$E_{\mathrm{l}}(\omega) = A_{\mathrm{l}}(\omega)\mathrm{e}^{-\mathrm{i}k_{\mathrm{l}}(\omega)x_{\mathrm{l}}} + B_{\mathrm{l}}(\omega)\mathrm{e}^{\mathrm{i}k_{\mathrm{l}}(\omega)x_{\mathrm{l}}}, \quad x_{\mathrm{l}-1} < x < x_{\mathrm{l}-1} \tag{3.3}$$

where k_{l} is the wave vector in slide l, and

$$k_{\mathrm{l}}(\omega) = n_{\mathrm{l}}\frac{\omega}{c} \tag{3.4}$$

where ω is the angular frequency of the EM wave. If the two amplitudes of E (A and B) are represented as column vectors, the adjacent column vector are related by the equation,

$$\begin{pmatrix} A_{\mathrm{l}}(\omega) \\ B_{\mathrm{l}}(\omega) \end{pmatrix} = P_{\mathrm{l}}(\omega)D_{\mathrm{l}}^{-1}(\omega)D_{\mathrm{l}}(\omega)\begin{pmatrix} A_{\mathrm{l}+1}(\omega) \\ B_{\mathrm{l}+1}(\omega) \end{pmatrix} \tag{5.5}$$

where the matrix

$$D_{\mathrm{l}}(\omega) = \begin{pmatrix} 1 & 1 \\ n_{\mathrm{l}}(\omega) & -n_{\mathrm{l}}(\omega) \end{pmatrix} \tag{5.6}$$

and

$$P_{\mathrm{l}}(\omega) = \begin{pmatrix} \mathrm{e}^{i\phi_{\mathrm{l}}(\omega)} & 0 \\ 0 & \mathrm{e}^{-i\phi_{\mathrm{l}}(\omega)} \end{pmatrix} \tag{5.7}$$

with

$$\phi_{\mathrm{l}}(\omega) = k_{\mathrm{l}}(\omega)\Delta x \tag{5.8}$$

The relation between $A_0(\omega)$, $B_0(\omega)$ and $A_{\mathrm{N}}(\omega)$, $B_{\mathrm{N}}(\omega)$ can be written as

$$\begin{aligned} \begin{pmatrix} A_0(\omega) \\ B_0(\omega) \end{pmatrix} &= D_0^{-1}(\omega)\left[\prod_{\mathrm{l}=1}^{N-1} D_{\mathrm{l}}(\omega)P_{\mathrm{l}}(\omega)D_{\mathrm{l}}^{-1}(\omega)\right]\begin{pmatrix} A_{\mathrm{N}}(\omega) \\ B_{\mathrm{N}}(\omega) \end{pmatrix} \\ &= \begin{pmatrix} M_{11}(\omega) & M_{12}(\omega) \\ M_{21}(\omega) & M_{22}(\omega) \end{pmatrix}\begin{pmatrix} A_{\mathrm{N}}(\omega) \\ B_{\mathrm{N}}(\omega) \end{pmatrix} \end{aligned} \tag{5.9}$$

and the reflection coefficient is defined as

$$r(\omega) = \frac{M_{21}(\omega)}{M_{11}(\omega)} \tag{5.10}$$

For an EM wave with specific frequency ω travelling through a round trip in the chirped DBR, the changing rate of its phase shift with respect to angular frequency represents the group delay, such that

$$\tau_g(\omega) = \frac{\arg(r(\omega))}{\omega} \tag{5.11}$$

The 1D model is firstly performed to estimate the GVD in GaAs material. The round-trip group EM wave delays in flat-ridge waveguides with lengths of 4.9 mm, 5 mm and 5.1 mm, and a frequency range from 2 THz to 3 THz are calculated from equation 5.11, as shown in Figure 3.4.

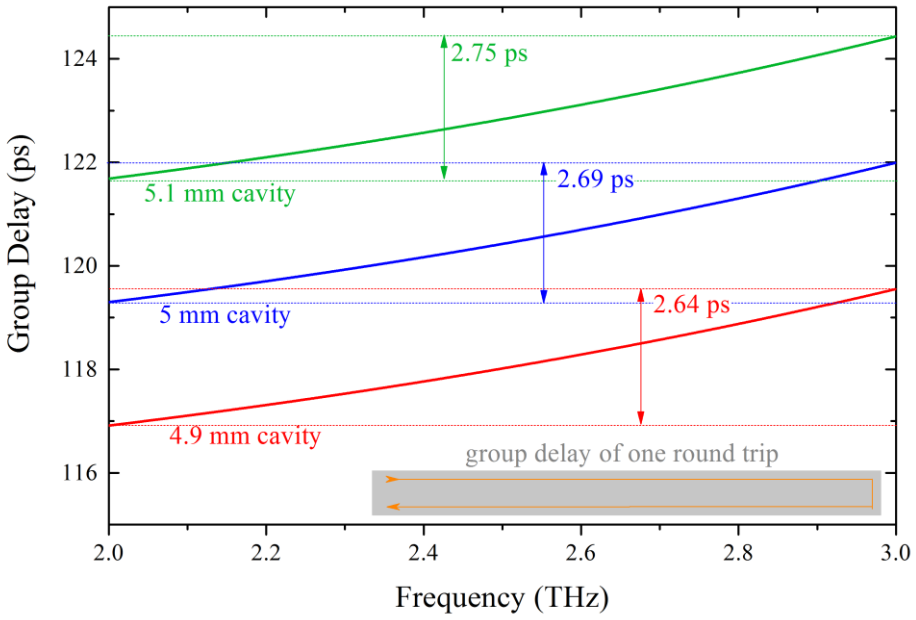

Figure 3.4 Calculated round-trip EM wave group delays in GaAs flat-ridge waveguides with cavity lengths of 4.9 mm, 5 mm, and 5.1 mm.

EM waves with lower frequencies travel faster than higher frequency in GaAs material, and which results in a group delay dispersion in the cavity. The results in Figure 3.4 indicates a stronger dispersion occurs with a longer waveguide, which becomes a serious shortcoming for achieving comb operation in a THz QCL. In a flat-ridge waveguide, the repetition frequency (spacing frequency between two adjacent lasing modes) is inversely proportional to the length of the waveguide. In this case, a longer flat-ridge

waveguide can involve a larger number of lasing modes within the limited gain bandwidth of the laser, and thus benefit for the strength of the FWM effect among the lasing modes to achieve broad-band comb operation [45]. However, as a counter effect, the stronger dispersion in longer waveguide shifts the lasing mode frequencies inside, thereby destroying the formation of frequency comb. Thus, a chirped DBR is even more desirable in THz QCLs with long waveguides to alleviate this critical drawback.

3.1.3 Basic behavior of chirped DBR structures

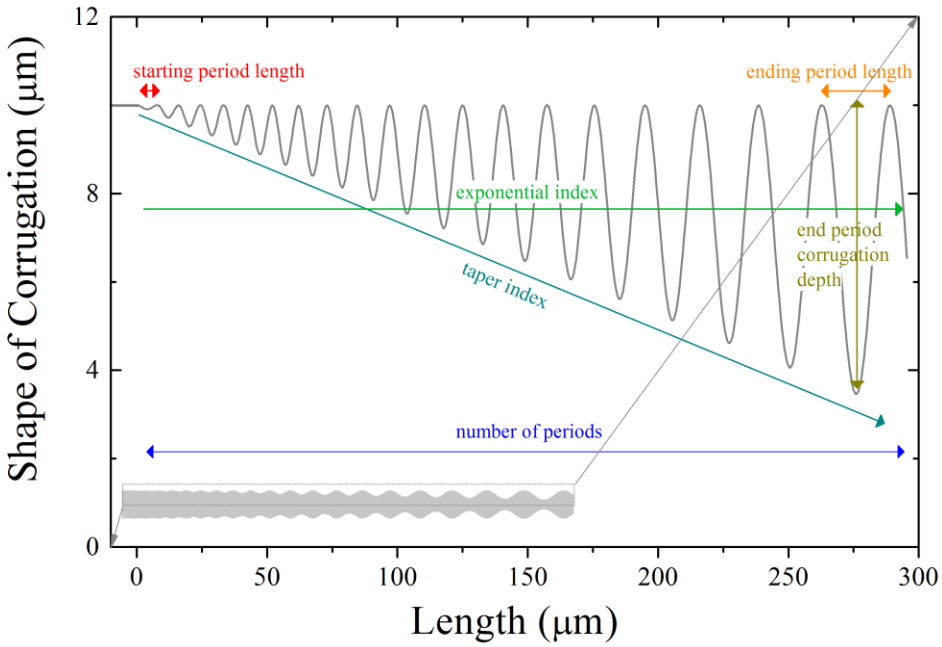

Figure 3.5 The most important geometric parameters that define the chirped DBR design.

To fulfill this purpose, the 1D model is then deployed to the chirped DBR structure to acquire the conceptual result of the performance on compensating the GVD of EM wave caused by long flat-ridge waveguide. However, even using a simplified 1D model, the investigation on chirped DBR is still quite complicated, because there are quite a few geometric parameters interfering the performance of GVD compensation. Figure 3.5 illustrates the major geometric parameters of a chirped DBR structure that determine the

performance of GVD compensation, which are starting period length, ending period length, exponential index, taper index, ending period corrugation depth, and number of periods.

The *starting period length* (L_1) determines the upper limit of the frequency band chirped DBR structure operation.
The *ending period length* (L_N) determines the lower limit of the frequency band for chirped DBR structure operation.
The *ending period corrugation depth* (D_N) describes the depth of corrugation at the ending period.
The *shift index (α)* describes how the period length evolves from the starting period to the ending period. In our model, a function of $L_i = L_1 + (L_i - L_i)(i/N)^{\alpha}$ is used, where L_i is the length of the i^{th} period with the total number of periods equal to N.
The *taper index (β)* describes how corrugation depth tapering from the starting period to the ending period. In our model, a function of $D_i = D_N \times [(\sum_1^i L_i - 0.5L_i)/\sum_1^N L_i]^{\beta}$ is used, where D_i is the corrugation depth of the i^{th} period.
The *number of periods* (N) determines the amount of compensation in group delay.

To systematically investigate the effect of these parameters, a series of simulations were carried out, in which only one of these parameters is tuned while all others remain unchanged. In order to remove the interference of high-order transverse modes, we set the width of the un-chirped waveguide (before the starting period) to be 20 μm.

I). Tuning the starting period length

Table 3.1 Geometric parameters of chirped DBR: tuning the starting period length

Starting Period length (μm)	Ending Period length (μm)	Ending period corrugation depth (μm)	Shift index	Taper index	Number of periods
6	26	9	2	1	30
8	26	9	2	1	30
10	26	9	2	1	30

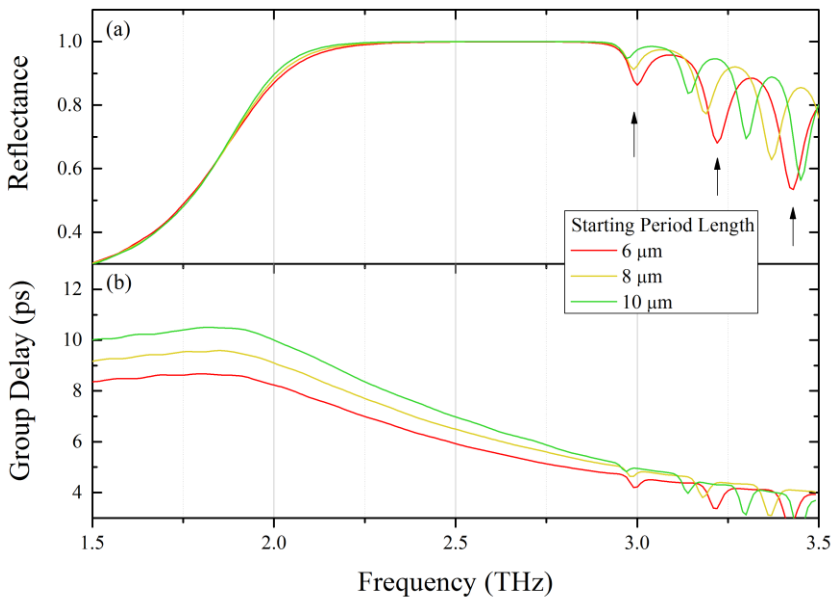

Figure 3.6 Reflectance spectra and group delay of chirped DBR structures, calculated based on the geometric parameters listed in Table 3.1.

Shorter starting periods push the upper frequency limit of the reflection band towards higher frequencies [~2.9 THz to ~3.0 THz in Figure 3.6(a)]. However, they also spread the distribution of the lengths of all periods in the chirped structure (because the number of periods is fixed at 30), which results in stronger ripples [as shown by arrows in Figure 3.6(a)] on the group delay curve at frequencies above 3 THz [as shown in Figure 3.6(b)]. In the chirped DBR structure, the corrugation depths in the starting period region are shallower than those in the ending period region. As a result, the optical reflection of the DBR is weaker at high frequencies (corresponding to shorter periods) than that at lower ones (corresponding to longer periods). To counteract the quick drop of the reflection at high frequencies, more corrugation periods must be allocated to the starting period region. This would extend the reflectance spectra [Figure 3.6(a)] to higher frequencies.

II). Tuning the ending period length

Table 3.2 Geometric parameters of chirped DBR: tuning the ending period length

Starting Period length (μm)	Ending Period length (μm)	Ending period corrugation depth (μm)	Shift index	Taper index	Number of periods
8	24	9	2	1	30
8	26	9	2	1	30
8	28	9	2	1	30

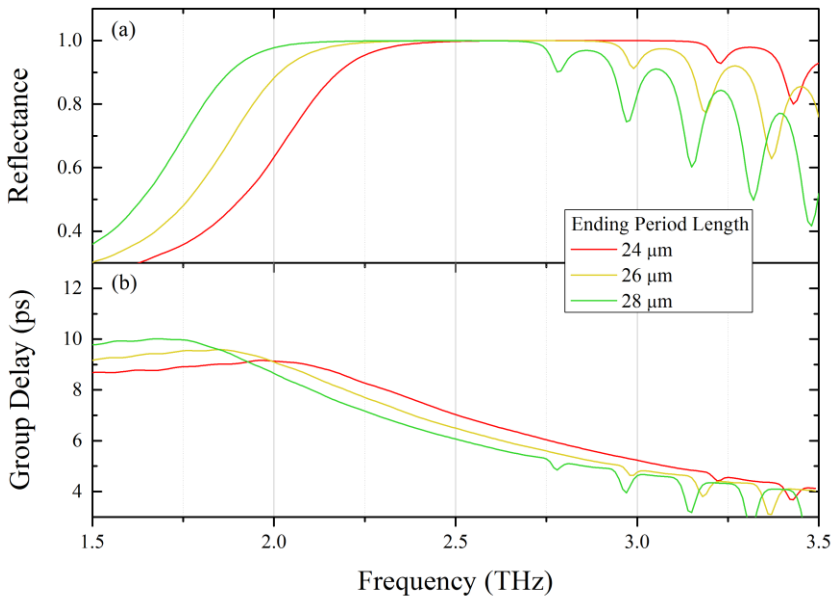

Figure 3.7 Reflectance spectra and group delay of chirped DBR structures, calculated based on the geometric parameters in listed Table 3.2.

Similar to the effects of starting period tuning, a longer ending period moves the lower frequency limit of the reflection band towards lower frequencies. However, this phenomenon is more sensitive to changes in period length (~2.3 THz to ~1.9 THz with ending period length switching from 24 μm to 28 μm) due to the deeper corrugation depth at the ending period side. Also, we observed a red shift in the frequency of the high frequency limit caused by the redistribution of the lengths of all periods in the chirped structure. Since the total number of periods is fixed to be 30, increasing the length of the ending period results in less allocation of the shorter period corrugations.

III). Tuning the ending period corrugation depth

Table 3.3 Geometric parameters of chirped DBR: tuning the ending period corrugation depth

Starting Period length (μm)	Ending Period length (μm)	Ending period corrugation depth (μm)	Shift index	Taper index	Number of periods
8	26	9	2	1	30
8	26	8	2	1	30
8	26	7	2	1	30

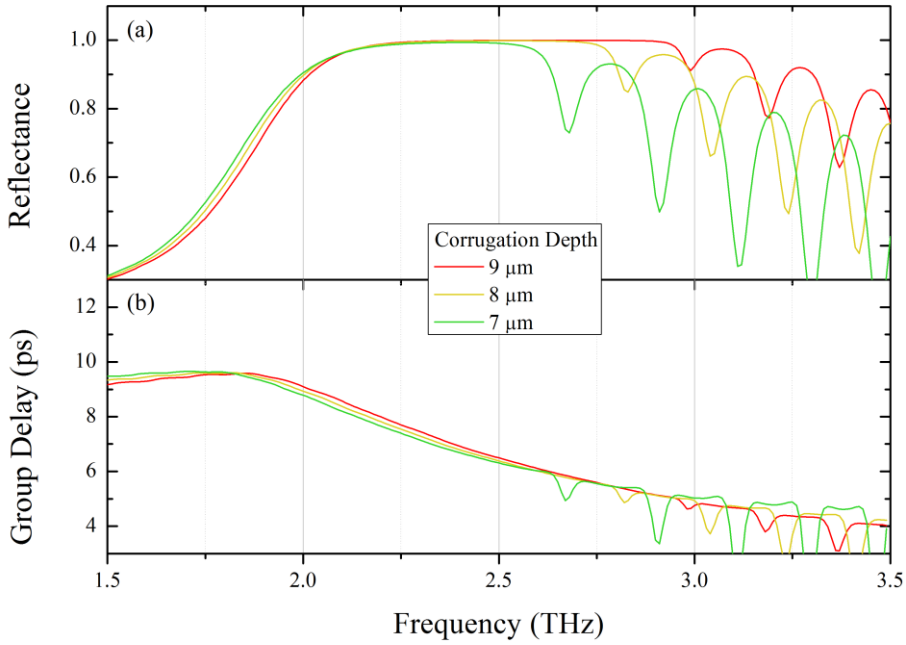

Figure 3.8 Reflectance spectra and group delay of chirped DBR structures, calculated based on the geometric parameters in Table 3.3.

For the simplicity of explanation, we introduced a fixed taper index of 1 in this group of simulation, which means, the corrugation depths increase linearly from the starting period to the ending period. Thus, a deeper ending period corrugation depth increases the depth of corrugation for all periods along the sidewall of the structure. Reflectance in the high frequency region benefits most from the deeper corrugation depth, as shown in Figure 3.8. However, the reflectance at the lower frequency region does not show much improvement due to the already sufficiently deep corrugation depths of the periods at the ending period region.

IV). Tuning the shift index

Table 3.4 Geometric parameters of chirped DBR: tuning the shift index

Starting Period length (μm)	Ending Period length (μm)	Ending period corrugation depth (μm)	Shift index	Taper index	Number of periods
8	26	9	1	1	30
8	26	9	2	1	30
8	26	9	3	1	30

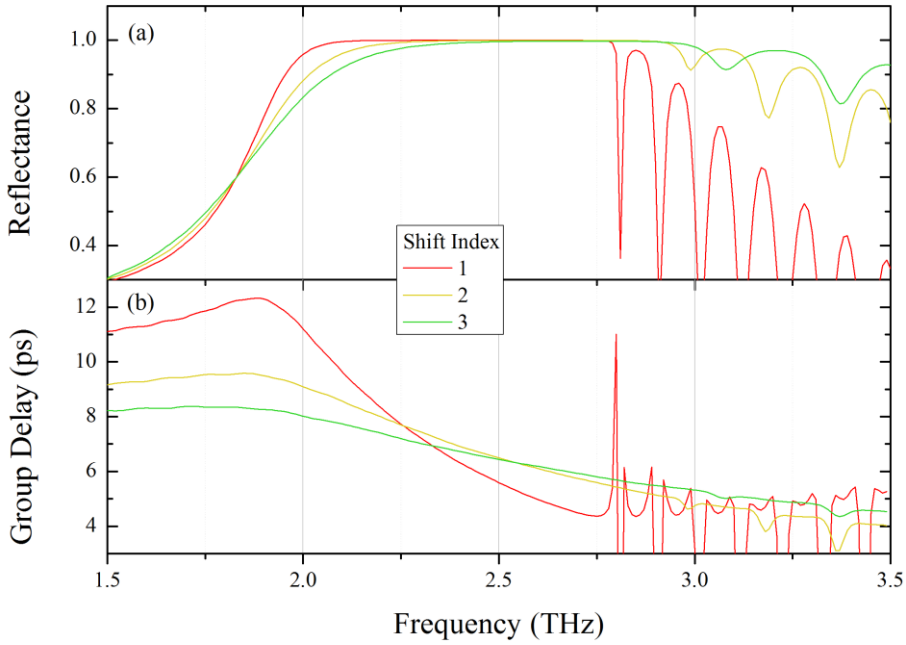

Figure 3.9 Reflectance spectra and group delay of chirped DBR structures, calculated based on the geometric parameters listed in Table 3.4.

The shift index (α) describes the changing rate of period length from the starting period to the ending period. With an increased shift index from 1 to 3, more corrugation periods are distributed to the starting period side, which results in an improvement of reflectance at the higher frequency region at the expense of that at the lower frequency side, as shown in Figure 3.9(a). The shift index also affects the group delay dispersion (which is equal to the slope of group delay curve, as shown in Figure 3.9(b)). This redistribution of the period length forces longer frequency waves to be reflected earlier in the chirped DBR structure. As a result, the efficiency of group delay compensation drops.

V). Tuning the taper index

Table 3.5 Geometric parameters of chirped DBR: tuning the taper index

Starting Period length (μm)	Ending Period length (μm)	Ending period corrugation depth (μm)	Shift index	Taper index	Number of periods
8	26	9	2	1	30
8	26	9	2	2	30
8	26	9	2	3	30

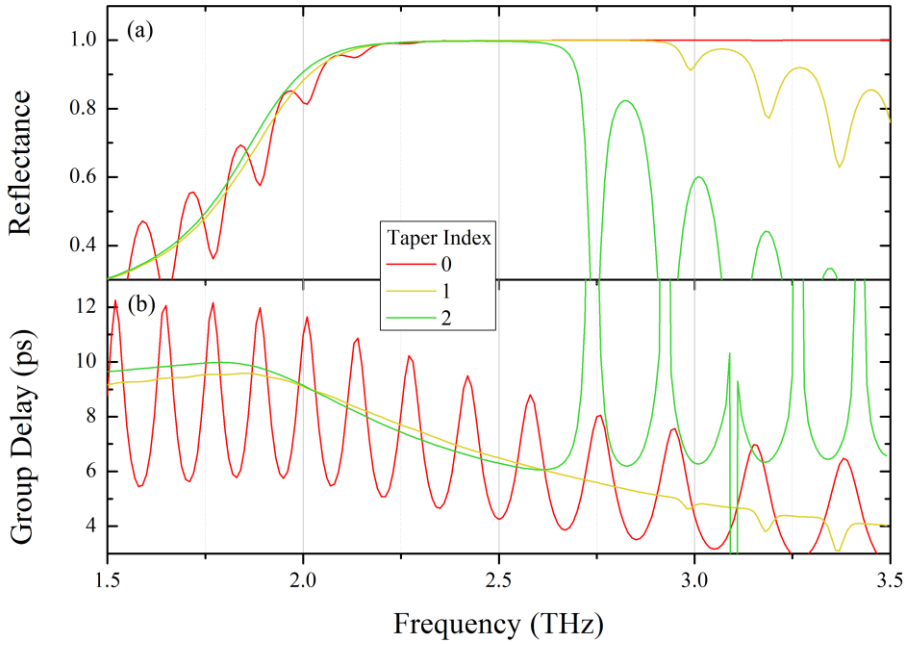

Figure 3.10 Reflectance spectra and group delay of chirped DBR structures with the geometric parameters listed in Table 3.5.

The taper index (β) parameter describes how corrugation depth evolves from the starting period region to the ending period region. A taper index of 0 represents an equally deep corrugation depth for all the periods in the DBR structure, which provides a strong reflectance across the entire reflection band (as shown in Figure 3.10(a)). However, this may generate strong ripples on the group delay curve [as shown in the red curve in Figure 3.10(b)] because the EM wave behaves like a Gires-Tournois interference [68], which will be discussed in detail in section 3.2.2. The results of 1D simulation show that a linear tapering (taper index=1) is capable of providing enough reflection within a wide frequency

range while maintaining a more monotonic group delay curve.

VI). Tuning the number of periods

Table 3.6 Geometric parameters of chirped DBR: tuning the number of periods

Starting Period length (μm)	Ending Period length (μm)	Ending period corrugation depth (μm)	Shift index	Taper index	Number of periods
8	26	9	2	1	20
8	26	9	2	1	30
8	26	9	2	1	40

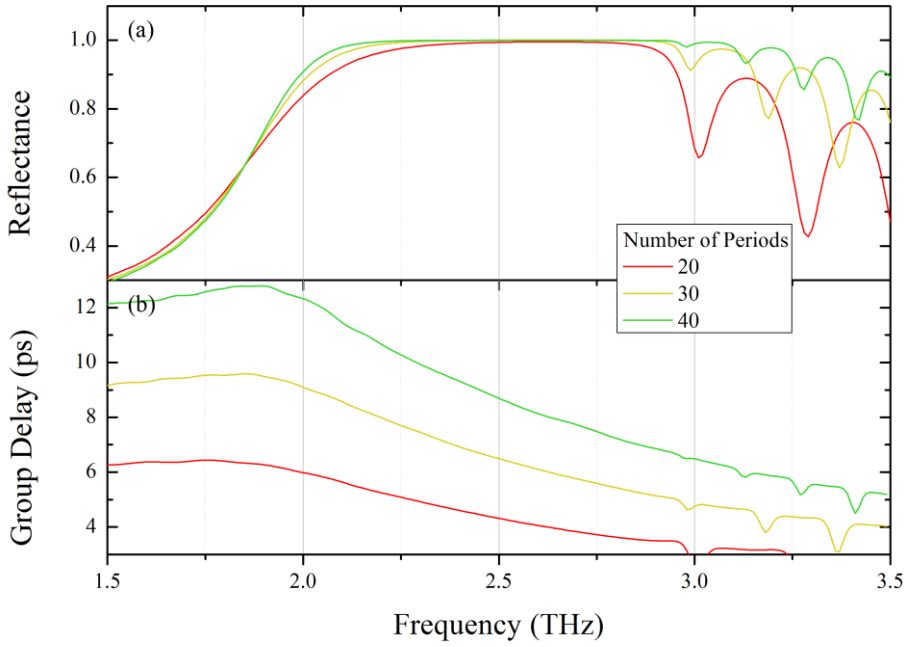

Figure 3.11 Reflectance spectra and group delay of chirped DBR structures, calculated based on the geometric parameters listed in Table 3.6.

Increasing the number of periods provides a limited improvement to the frequency bandwidth of reflectance. Figure 3.11 shows the reflectance at high frequencies, which is associated with the starting period region with shallower corrugation depth, and benefits more from the increased number of periods than reflectance at lower frequencies. However, the number of periods also determines the group delay dispersion (slope of the group delay curve) within the desired frequency band, which needs to be carefully adjusted to provide

accurate compensation as needed.

In conclusion, the above systematic study with 1D modeling gives us a brief strategy for defining the geometric parameters of chirped DBR structure in the following design work. The starting period and ending period lengths are used to define the upper and lower frequency limit of the GVD compensation frequency band. Also, based on the 1D modelling results, we conclude that an ending period corrugation depth of 9 μm (with an un-chirped-waveguide-width of 20 μm) provides sufficient reflection across the entire target frequency band; a shift index of 2 provides a balanced reflection at both higher and lower frequencies. A taper index of 1 produces a monotonic shape in the GVD curve across the entire target frequency band. The number of periods is used to control the amplitude of GVD compensation within the target frequency band.

3.2 3D Modeling of chirped DBR structures in COMSOL Multiphysics

The 1D model based on transfer matrix method provides a convenient way to grasp fundamental behavior of the group delay dispersion of terahertz wave in GaAs based ridged waveguide and its compensation by the chirped DBR structure. The DBR's geometric parameters including both the starting and ending period lengths, which determine the frequency bandwidth can be roughly estimated using the 1D model. However, the amplitude of the group delay dispersion across the target frequency bandwidth in either the un-chirped flat-ridge waveguide or chirped DBR structure cannot be accurately calculated with the 1D model because it oversimplifies approximations without considering the confinement factor. Therefore, building a 3D model using COMSOL Multiphysics to verify the preliminary results from the 1D model is essential to the chirped DBR structure design.

3.2.1 Geometric features of chirped DBR structures in 3D modeling

For simplicity, the geometry of the chirped DBR structure in the 3D model is built upon a GaAs slab (with rectangular cross section) and, is covered with perfect electric conductors on both the top and bottom facets, which serve as top and bottom metal contact layers. The chirped DBR corrugation is affixed along the two side walls of the waveguide, as shown in Figure 3. 12 (top view of the chirped DBR structure).

Figure 3.12 Top view of the chirped DBR structure in 3D model.

The chirped DBR structure is then embedded into a rectangular box of environmental material (air with relative permittivity of 1). The front and back facets are set as Port 1 and Port 2 respectively, as shown in Figure 3.13. The EM wave is injected from Port 1 at the starting (shorter) period side, while the port at the ending (longer) period side is set to be passive.

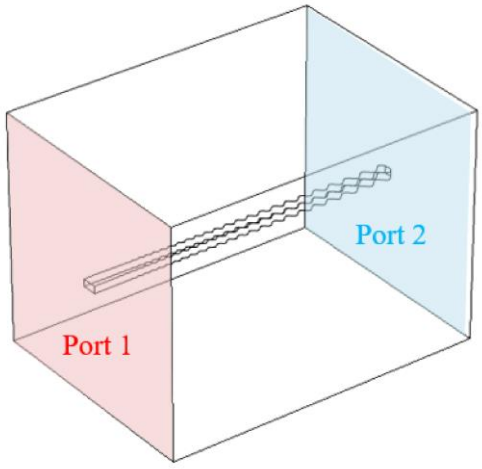

Figure 3.13 The chirped DBR structure is embedded in the surrounding material in the 3D model. The front (red) and back (blue) facets are set as port 1 and port 2 respectively.

The S-parameters of the chirped DBR waveguides are calculated as a function of frequency. Due to the narrow ridge width (20 μm) of the waveguide, only the TEM_{00} lateral mode is considered, and the reflectivity is determined by the S_{11} parameter. Then, the group delay is calculated as a function of frequency, as was done with the 1D model. When solving the EM waves in the 3D model, the boundaries of the structure need to be transparent, which means that the EM waves can penetrate through the boundaries of the structure without reflection. Thus, special attentions must be paid to the boundary conditions in the simulation. COMSOL Multiphysics offers one solution for this boundary setting, called Perfectly Matched Layers (PMLs) [69]. To obtain an accurate simulation result, all the chirped DBR structures discussed use PML as boundary conditions. The PMLs, which provide non-reflective boundaries, are added by attaching all the facets of the structure of Figure 3.13. The completed structure for the 3D simulation is shown in Figure 3.14.

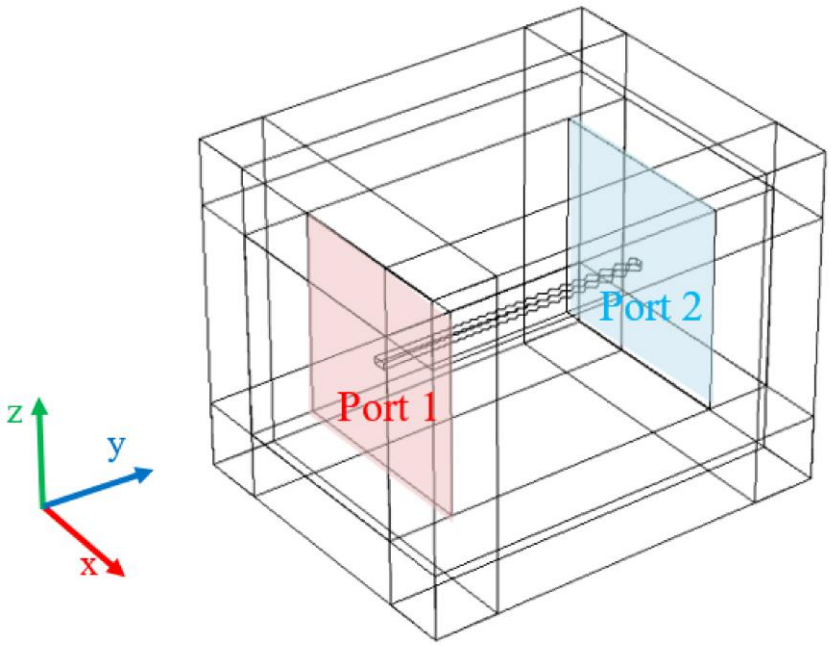

Figure 3.14 The structure is covered by PMLs at all the facets in the 3D model.

In the simulation, the EM field is calculated at a specific frequency in the structure as shown in Figure 3.14. To obtain the frequency dependent reflectance and group delays across a frequency band, the above calculation is repeated by sweeping the EM frequency.

This requires intensive computing and is very time consuming. Since the simulated structure is symmetric in the x and z directions, it is possible to save simulation time by employing an improved model with one-quarter of the structure and periodic, as shown in Figure 3.15.

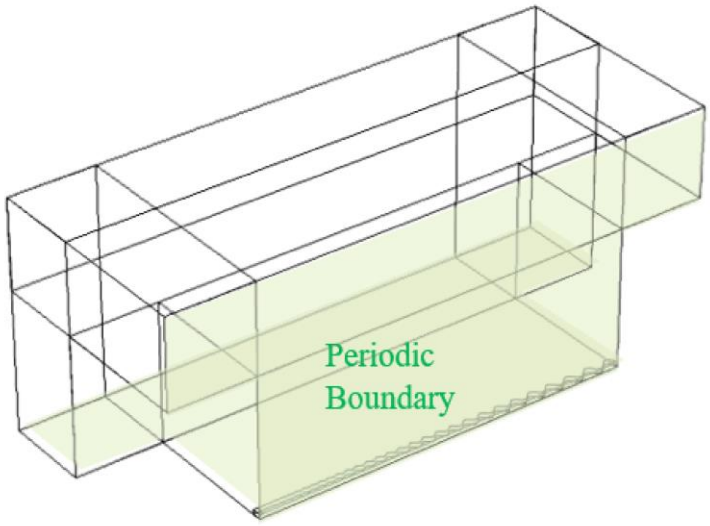

Figure 3.15 One-quarter of the full structure with periodic boundaries set at cross sections (green facets).

In this case, only the EM field in one-quarter of the full structure is calculated, which could cut the simulation time by more than half. To qualify the one-quarter 3D model, a chirped DBR structure is simulated in both the full structure model and the one-quarter structure model. The result in Figure 3.16 shows that the 3D one-quarter structure model can perfectly predict all the target behaviors of the reflectance and the group delay compensation in the chirped DBR originally revealed by the 3D full structure model.

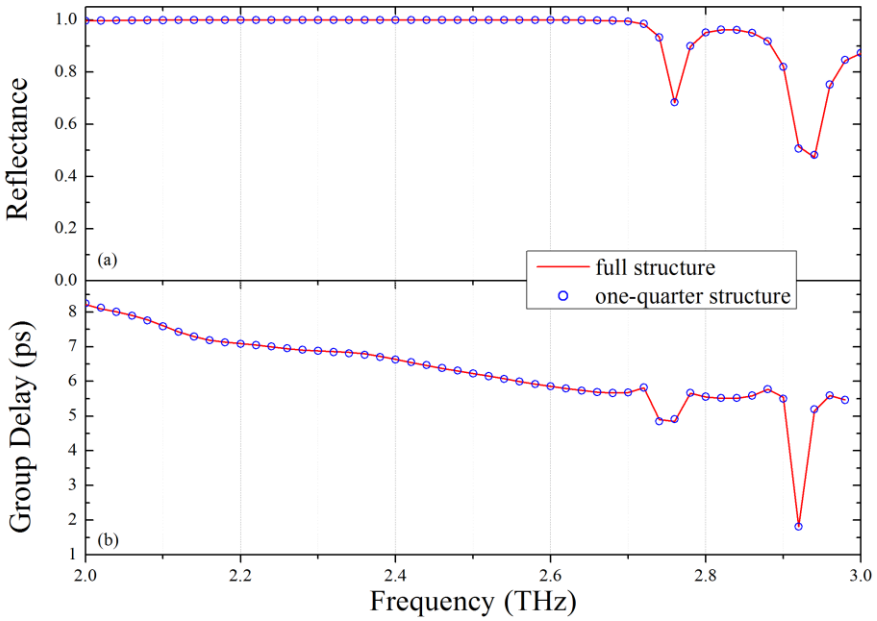

Figure 3.16 Calculated reflectance spectra (a) and group delay (b) of the chirped DBR structure in the 3D full structure model (red lines) and 3D one-quarter structure model (blue circles).

3.2.2 Mode distribution in chirped DBR structures

The distribution profile of the electric-magnetic field inside the waveguide can also be calculated using 3D models built with COMSOL Multiphysics, which helps us better understand the behavior of the chirped DBR structure. Figure 3.17(a) shows the calculated reflectance vs. frequency curve of a chirped DBR structure with the geometric parameters described in Table 3.7.

Table 3.7 Geometric parameters of a chirped DBR for 3D simulation

Starting Period length (μm)	Ending Period length (μm)	Ending period corrugation depth (μm)	Shift index	Taper index	Number of periods
8	26	9	2	1	30

The mode distribution profiles of the DBR structure at a frequency of 2.40 THz

(which is still within its reflection band with its reflectance close to unity) is shown in Figure 3.17(b), and at a frequency of 2.74 THz (which is just beyond the edge of the reflection band, where the reflectance begins to drop) is shown in Figure 3.17(c). Compared with the calculated mode distribution profiles at these two frequencies, it clearly reveals that the chirped DBR loses its ability to reflect the EM waves due to the too shallow corrugation depths at the starting period region which targets higher frequencies [~2.74 THz in Figure 3.17(a)]. As a result, parts of the EM waves leak out into the ending period side of the chirped DBR structure, and the travel distance of the EM waves at this frequency and higher are not fully under control as originally expected. Therefore, the group delay compensation is not achieved with this chirped DBR structure.

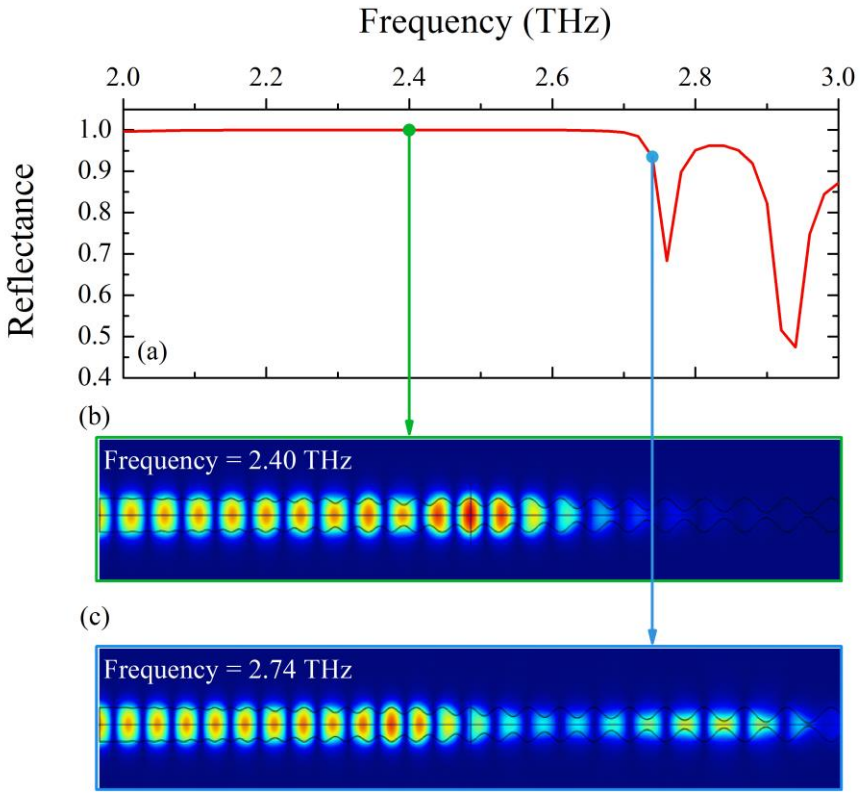

Figure 3.17(a) Reflectance spectra of a chirped DBR structure in 3D model, calculated using the geometric parameters be listed in Table 3.7. (b) Calculated mode distribution profile of EM waves at 2.40 THz in the chirped DBR. (c) Calculated mode distribution profile of EM waves at 2.74 THz in the chirped DBR.

Another critical feature of the chirped DBR, which strongly degrades its performance of group delay compensation is the so called Gires-Tournois interferometer like cavity. As discussed in the 1D modeling results (shown in Figure 3.10), if a taper index of 0 is used in the designed chirped DBR structure, the group delay compensation curve will have multiple ripples across the entire target frequency band. This phenomenon is due to the sudden change in passing cross-section area of the waveguide from the un-chirped ridge region into the chirped DBR region, which generates an abrupt change of effective mode index and traps the EM wave inside the chirped DBR.

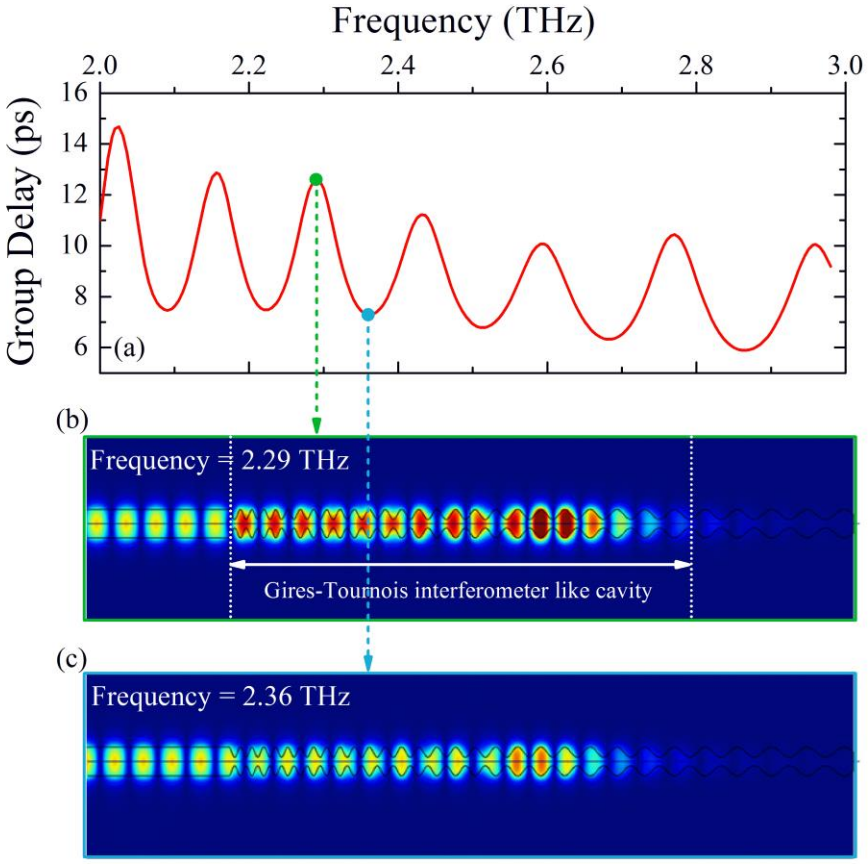

Figure 3.18 (a) Calculated group delay in 3D modeled chirped DBR structure with a taper index of 0. (b) Calculated mode distribution profile of EM wave at 2.29 THz in the chirped DBR. (c) Calculated mode distribution profile of EM wave at 2.36 THz in the chirped DBR.

From the calculated mode distribution profiles generated by our 3D model in Figure 3.18(b) and (c), it is clearly revealed that, at certain frequencies [e.g. 2.29 THz in Figure

3.18(b)] that meets the boundary condition of the small cavity (Gires-Tournois interferometer cavity), the mode is bounced back by the facet between the un-chirped rectangular waveguide and the chirped DBR. This creates a small cavity and further delays the EM wave travels. However, at an off-resonant frequency of 2.36 THz [as shown in Figure 3.18(c)), the EM wave can freely pass through this facet without reflection, thus experiencing reduced delay time. In the design of chirped DBR structure for real devices, the Gires-Tournois interferometer like cavity behavior can often be observed. To prevent this phenomenon from affecting the group delay compensation performance, we need to carefully adjust the geometric parameters of the chirped DBR.

3.3 Comparison between 1D model and 3D model for chirped DBR structures

3.3.1 Confinement factor of waveguides in 3D model

Different from the 1D model, in which the EM mode is approximated to be uniformly distributed in the lateral direction of the waveguide [as shown in Figure 3.19(a)], the EM mode in the 3D model is distributed as a close-to-Gaussian shape (supposing only the fundamental lateral mode is considered) inside the waveguide [as shown in Figure 3.19(b)]. Furthermore, the EM mode can partially distribute out of sidewalls of the waveguide, which results in a lower confinement factor.

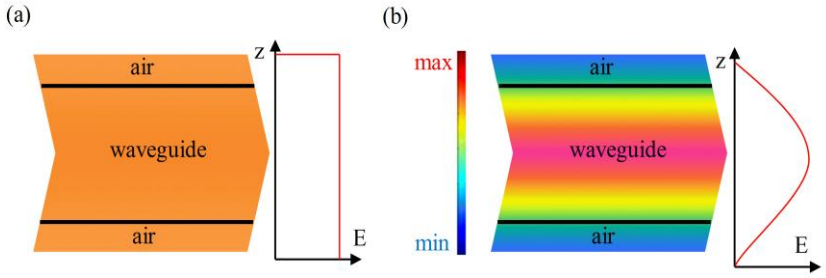

Figure 3.19 (a) Schematic of mode distribution in the 1D model (top view). (b) Schematic of mode distribution in the 3D model (top view).

The GVD inside the waveguide is actually caused by the dispersion in effective mode index of EM waves at different frequencies, and the effective mode index is highly sensitive to the confinement factor of the waveguide structure, thus the 3D model can provide a more accurate estimation of the travelling behavior of EM wave traveling in both un-chirped rectangular waveguides and chirped DBR structures.

3.3.2 Revised group delay dispersion and reflectance with 3D model

Figure 3.20 shows the calculated one-round trip group delay curve of EM waves from 2.5 THz to 3.5 THz in a 250 μm long un-chirped flat-ridge waveguide using the 3D (red) and 1D (blue) model. It is clear that the calculated group delays in the 1D model are stronger (from 6.03 ps at 2.5 THz to 6.21 ps at 3.5 THz) than those calculated by the 3D model (from 4.73 ps at 2.5 THz to 5.03 ps at 3.5 THz). A cross section area with a height of 10 μm and a width of 20 μm is set for the flat-ridge waveguide in the 3D model. This can be explained by the oversimplified approximation of the confinement factor in the 1D model, where the EM wave is supposed to uniformly stay inside the waveguide. Instead, in the 3D model, the EM mode can partially distribute outside of the waveguide (into air) and results in a drop in the effective mode index. Thus the EM wave travels faster (with lower group delay) in the structure with a 3D model calculation.

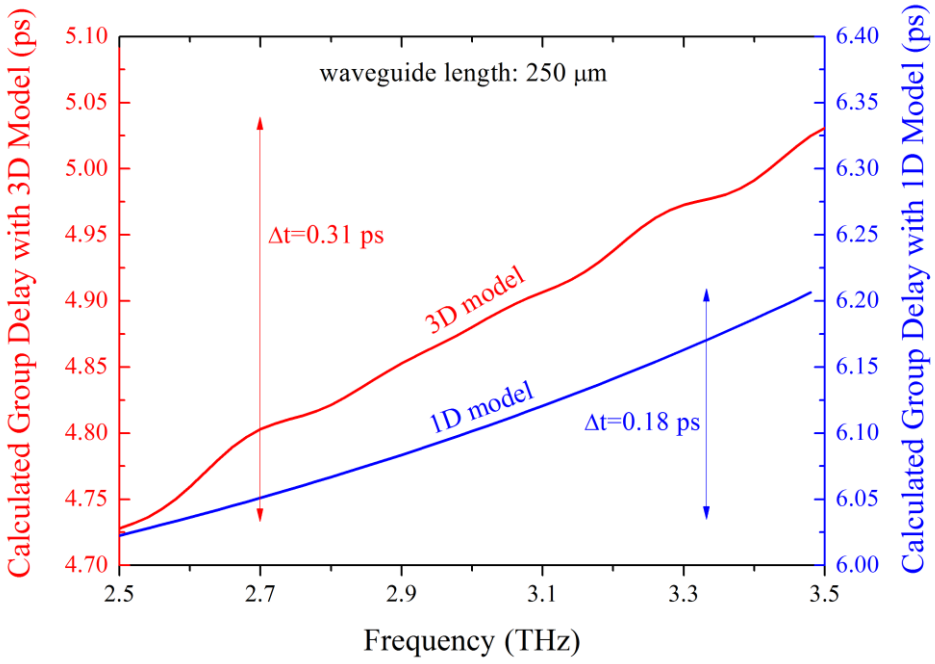

Figure 3.20 Calculated group delay (one round trip) of the EM waves of frequencies between 2.5 THz and 3.5 THz in a 250-μm-long flat-ridge waveguide by the 1D (blue) and 3D (red) models.

Another interesting phenomenon, which is revealed in Figure 3.20, is the different group delay dispersion (defined as the differential group delay time between EM waves with 2.5 THz and that of 3.5 THz) calculated from the 1D and 3D models. A much stronger group delay dispersion of 0.31 ps is obtained in a 250 um long flat-ridge rectangular waveguide from the 3D model simulation, which is almost twice of that obtained from the 1D model simulation. The reason for this is revealed through further investigation into the evolving effective mode indexes of the waveguide structure with the EM wave frequencies.

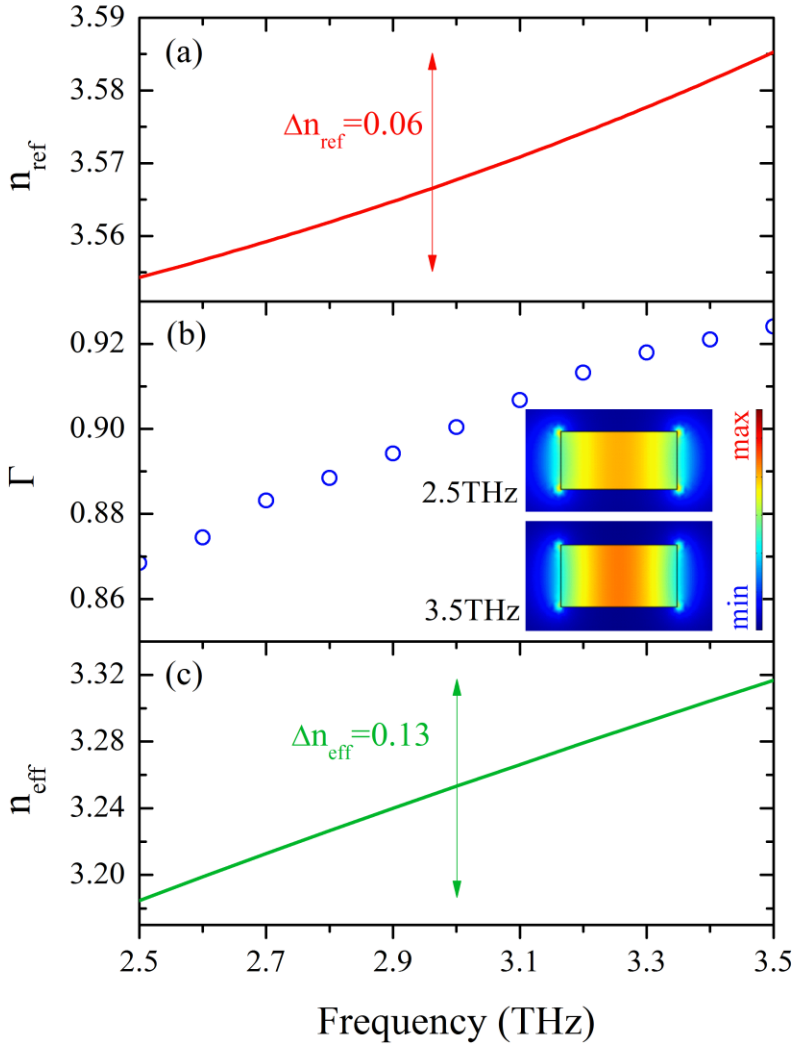

Figure 3.21 (a) The effective mode indexes in a flat-ridge waveguide, calculated with the 1D model without considering the mode confinement factor. (b) Mode confinement factor in a flat-ridge waveguide, calculated using the 3D model. Inset: the 2D mode distribution profile of EM waves at 2.5 THz and 3.5 THz in a waveguide (cross-section view). (c) Effective mode indexes in a flat-ridge waveguide, calculated with the 3D model by considering mode confinement factor.

Since the 1D model oversimplifies the mode distribution, the difference in effective mode indexes for EM waves at 2.5 THz and at 3.5 THz is the same as the difference in material refractive indexes, which is 0.06 (as shown in Figure 3.21(a). However, in the 3D

model, the frequency dependent mode confinement is considered, the distribution of EM waves with higher frequencies are more concentrated inside the waveguide (as shown in inset figures in Figure 3.21(b)). In this case, the EM waves with lower frequencies leak out to the surrounding air and further decreases their effective mode index. As a result, by considering the mode confinement factor, the difference in effective mode indexes between higher frequency EM waves and lower frequency EM waves is expanded (as shown in Figure 3.21(c)) and generates a stronger group delay dispersion. In this case, the simplified 1D model under-estimates the GVD in a flat-ridge rectangular waveguide and may misguide the designing work of chirped DBR structures. For a typical terahertz comb QCL, the length of its waveguide can be 20 times longer than 250 μm, and the discrepancy in the group delay dispersion is also 20 times larger.

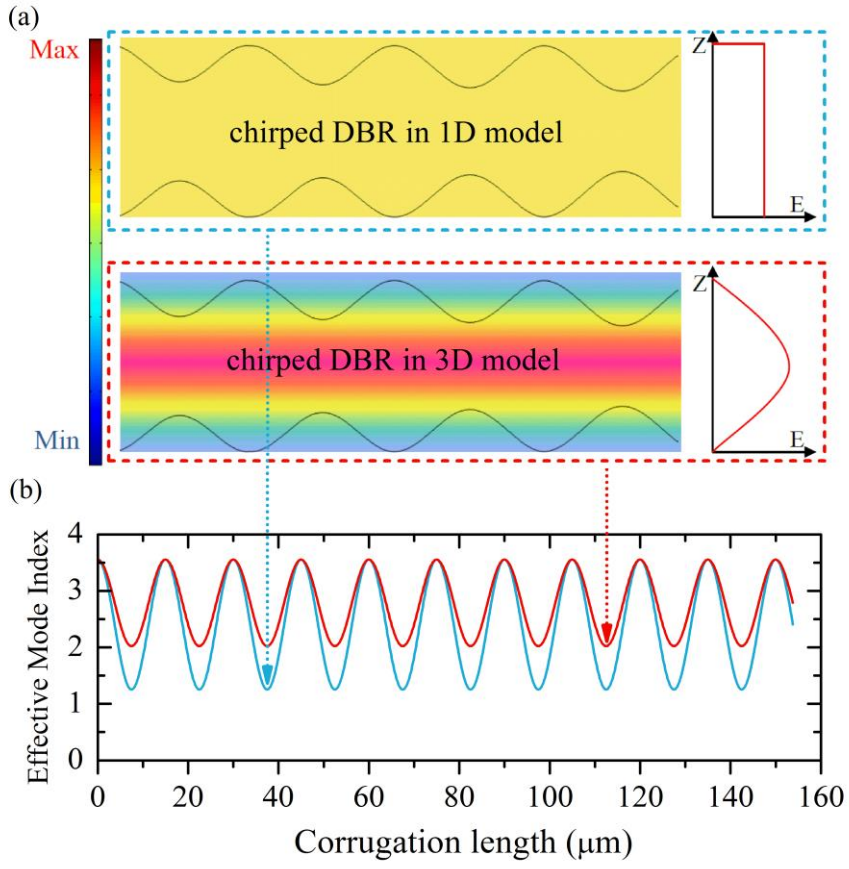

Figure 3.22 (a) Schematics of mode distributions in chirped DBR structure with 1D model (blue box) and 3D model (red box). (b) Effective mode indexes in chirped DBR structure with 1D model (blue curve) and 3D model (red curve).

The confinement factor of EM mode also interferes with the group delay compensation in chirped DBR structure. As being introduced in Section 3.1, the chirped DBR waveguide is constructed with a structure with varying ridge width of waveguide (sinusoidal shape at both side walls of the waveguide) and which results in periodic variation in the effective refractive index in the waveguide. The variation of effective refractive index generates a partial reflection of the EM wave with a certain wavelength.

In the 1D model, the mode distribution of the EM wave is uniform across the lateral direction of the waveguide. Thus the variation in the effective refractive index can be considered as proportional to the variation in the ridge width of the waveguide, as shown in Figure 3.22. In contrast to the 1D mode, where the EM wave is uniformly distributed in the waveguide structure, the EM wave in the 3D model is mostly distributed in the middle of the waveguide and the reduced portion of the mode, distribute at the sidewall region, can be affected by the chirped corrugation shape. As a result, the variation of the effective mode index is much weaker in the 3D model than that in the 1D model. The simulation result of the reflectance and the group delay curve (as shown in Figure 3.23) prove this effect. The geometrical parameters of the chirped DBR structure used in Figure 3.23 are listed in Table 3.8.

Table 3.8 Geometric parameters of chirped DBR for 1D and 3D model comparison

Starting Period length (μm)	Ending Period length (μm)	Ending period corrugation depth (μm)	Shift index	Taper index	Number of periods
7	22	9	2	1	40

Due to the weak variation of the effective mode index in the 3D model, the band width of the reflectance is much narrower than that calculated with the 1D model. At frequencies above 3 THz, many dips are observed due to the weak reflectance, which distort the group delay curve (red curve in Figure 3.23 (b)) with multiple ripples being generated at the corresponding frequencies (grey dashed curves in Figure 3.23).

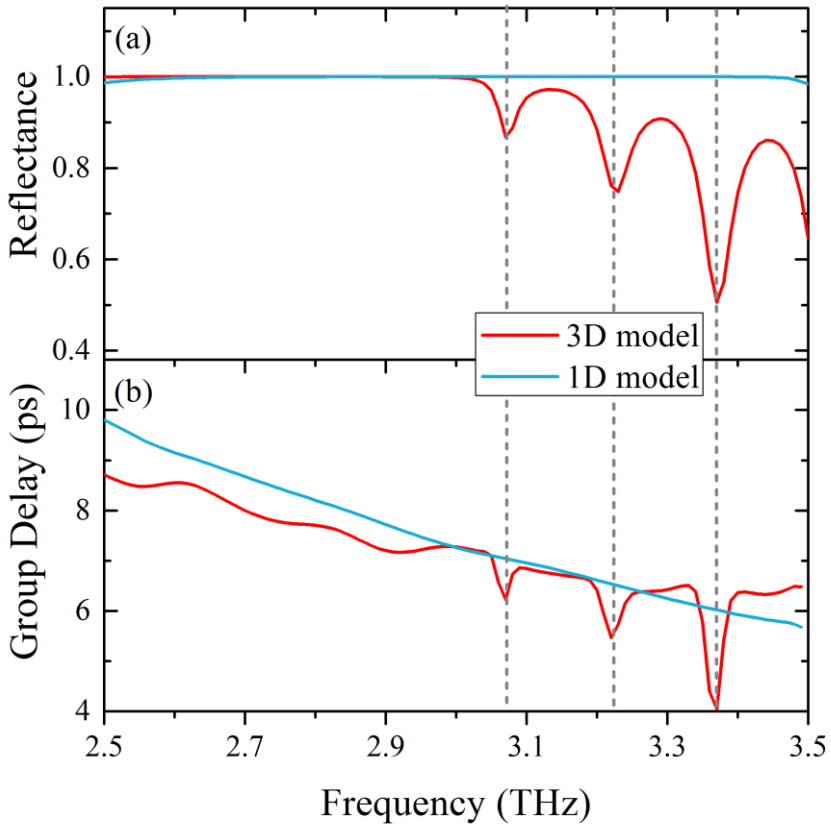

Figure 3.23 (a) Reflectance spectra of chirped DBR structure, calculated with the 1D model (blue) and 3D model (red). (b) Group delay curves of chirped DBR structure, calculated with the 1D model (blue) and the 3D model (red).

3.4 Summary

Due to the stronger GVD in GaAs material system at the terahertz frequency range, designing a chirped DBR structure that can compensate for the GVD generated by long flat-ridge metal-metal waveguides is essential for achieving and stabilizing comb formation in THz QCLs. For this purpose, we introduced both an efficient 1D model, based on transfer matrix method and an accurate 3D model, with the help of COMSOL, to estimate the GVD in the flat-ridge waveguide and GVD compensation in the chirped DBR structure. To quantitatively investigate and optimize the corrugation shape of the chirped

DBR for better performance, we introduced a series of important geometric parameters for the chirped DBR structure and revealed their behaviors through systematic simulation. Results presented in this chapter will support the design of real chirped DBR structures in THz QCL device, discussed in Chapter 4.

Chapter 4

Design of Chirped DBR Structures for Group Delay Compensation in THz QCLs with Metal-metal Waveguides

Following the modeling approaches and results for the chirped DBR structures described in Chapter 3, we will present strategies for the designing of a chirped DBR for practical THz QCLs with metal-metal waveguides. The geometric parameters of the chirped DBR structures, such as the corrugation depth of the chirped periods and the distribution profile of the period length, play a critical role in determining the extent of GVD compensation in practical waveguides. As shown earlier, the ripples in the group delay curves may become quite substantial if the chirped DBR structures are not properly designed. To eliminate these ripples, which result from the abrupt transition from the flat-ridge waveguide section to the chirped DBR section, a two-section chirped DBR structure is proposed [70].

4.1 Strategy for controlling group delay dispersion in THz QCLs with metal-metal waveguides

In order to achieve zero dispersion inside a long THz QCL metal-metal waveguide, one strategy is to fabricate a chirped DBR structure along the ridges of the waveguide, which introduces non-zero waveguide dispersion to compensate for the material dispersion introduced by the flat ridge waveguide section, as shown in Figure 4.1(a).

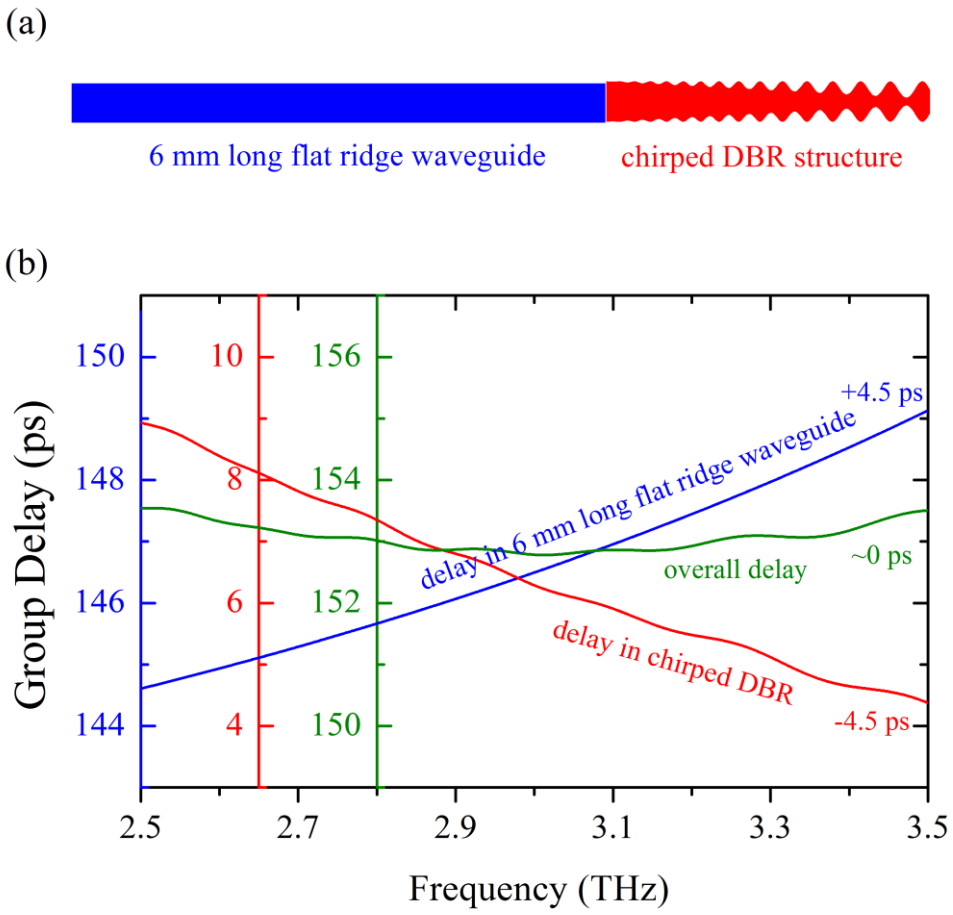

Figure 4.1 (a) Schematic of a full waveguide consisting of a chirped DBR structure (red) and a flat-ridge waveguide section (blue). (b) The group delay from a 6-mm-long flat-ridge waveguide (~ +4.5 ps, blue curve) within 2.5 to 3.5 THz is compensated by a carefully designed chirped DBR structure (~ -4.5 ps, red curve), resulting in a close to zero overall group delay (green curve).

Figure 4.1(b) provides an example to demonstrate how GVD compensation is achieved in a chirped DBR. The material group delay (one round trip) in a 6 mm-long rectangular ridge waveguide increases monotonically with frequency (the blue curve with ~ +4.5 ps from 2.5 to 3.5 THz). The monotonically-decreasing waveguide group delay (one round trip) of the chirped DBR (the red curve with ~ -4.5 ps from 2.5 THz to 3.5 THz in this chirped DBR structure) can therefore compensate for the monotonically-increasing material group delay partially or even completely, depending on the group delay

differences between the lower and higher frequencies. The contributions of GVD from the flat-ridge section and from the chirped DBR section match exactly, but with opposite signs. The green curve in Figure 1(b) is the total group delay dispersion that combines the red and blue curves, showing ~ 0 ps group delay from 2.5 THz to 3.5 THz.

4.2 Design of chirped DBR structures for F-series THz QCLs

4.2.1 Group delay dispersion in F-series THz QCLs

F-series THz QCLs with RP based three-well design [32] were chosen as our first attempt in engineering GVD control via a chirped DBR structure. There are several reasons for this choice. First, F-series THz QCLs demonstrate excellent temperature performance (with maximum lasing temperatures of 184 K for F26, 199.3 K for F30, 197 K for F35, 187 K for F41, and 199.5 K for F47), which ensure the THz QCLs have sufficient optical gain to achieve lasing even with a narrow-ridge waveguide for eliminating the high-order modes at the expense of higher optical loss; Second, F-series THz QCLs have relatively low threshold current (0.5 kA/cm^2 for F26, 0.66 kA/cm^2 for F30, 0.66 kA/cm^2 for F35, 0.94 kA/cm^2 for F41, and 0.97 kA/cm^2 for F47, all data were collected at 10 K) due to the reduced leakage current associated with diagonal design, which allows the device to be operated under CW mode. Third, the lasing spectrums of F-series THz QCLs spread from 2.5 THz to 3.5 THz at 10 K (as shown in Figure 4.2), which provides a relatively broad-band of lasing frequency for GVD investigation.

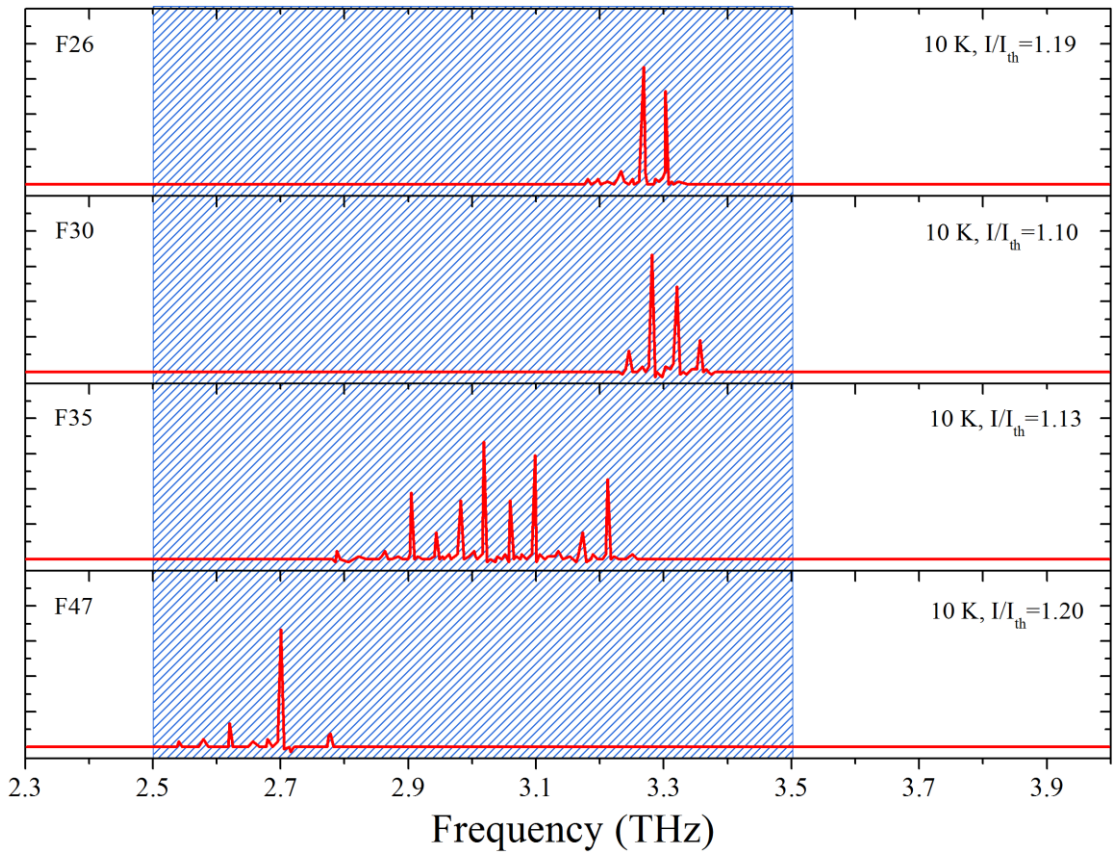

Figure 4.2 Lasing spectrums of the F-series THz QCLs (F26-F47) tested with metal-metal flat-ridge waveguides at a heat sink temperature of 10 K. The shadowed area indicates a frequency range (2.5 THz to 3.5 THz) covering all lasing Fabre-Perot modes from the F-series lasers [61].

Before designing the chirped DBR structure for the F-series THz QCLs, it is necessary to estimate the group delay dispersion in the long flat-ridge metal-metal waveguide, upon which we can determine how much compensation is needed in the chirped DBR structure. The estimation of GVD in the flat-ridge waveguide within the frequency range of 2.5 THz to 3.5 THz is calculated with the 3D model in COMSOL. The cross-section area of the metal-metal flat-ridge waveguide is set to be 20 μm wide and 10 μm high, while the length of the flat-ridge waveguide varies in the simulation (300 μm, 500 μm, and 1000 μm) to investigate the relationship between the group delay dispersion and the waveguide length. Group delay dispersion of three samples between 2.5 THz and 3.5 THz were calculated and presented in Figure 4.3, which shows the time delay (in unit

of Pico-second) of the EM wave with a frequency of 3.5 THz to that of 2.5 THz in one-round-trip. It is clear that the group delay dispersion increases perfectly linearly with increases in the length of the flat-ridge waveguide (0.282 ps for 300-μm-long waveguide, 0.693 ps for 500-μm-long waveguide, and 1.382 ps for 1000-μm-long waveguide). In this case, a group delay dispersion of 6.906 ps between 2.5 THz and 3.5 THz can be accurately predicted for a flat-ridged metal-metal waveguide with a length of 5000 μm, and the waveguide length can then be used to test the comb operation in future. This is proved to be an effective strategy to estimate the group delay dispersion in an arbitrary long waveguide, for which saves the calculating time and computer resources during the 3D model simulation.

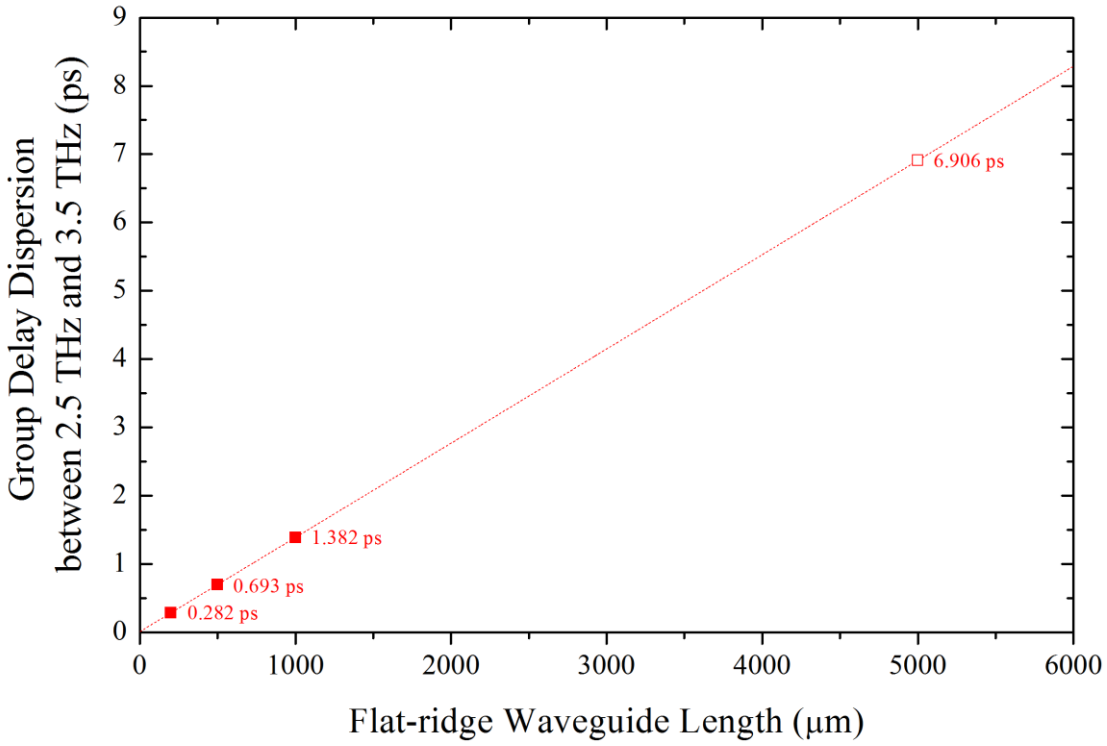

Figure 4.3 Calculated group delay dispersion of EM waves with frequencies between 2.5 THz and 3.5 THz (round-trip) in a flat-ridge metal-metal waveguide with the cross-section area of 20 μm × 10 μm and three different waveguide lengths (300 μm, 500 μm, and 1000 μm, in solid squares). The group delay dispersion for a 5000-μm-long waveguide is predicted (in void square).

4.2.2 Design of chirped DBR structures for F-series THz QCLs

After estimating the group delay dispersion in flat-ridge waveguides within the target frequency range, we undertook design of a chirped DBR to compensate for such dispersions. Based on the discussion in Chapter 3, a starting period length of 13 μm and an ending period length of 20 μm is first chosen to ensure the chirped DBR structure will cover the frequency range from 2.5 THz to 3.5 THz.

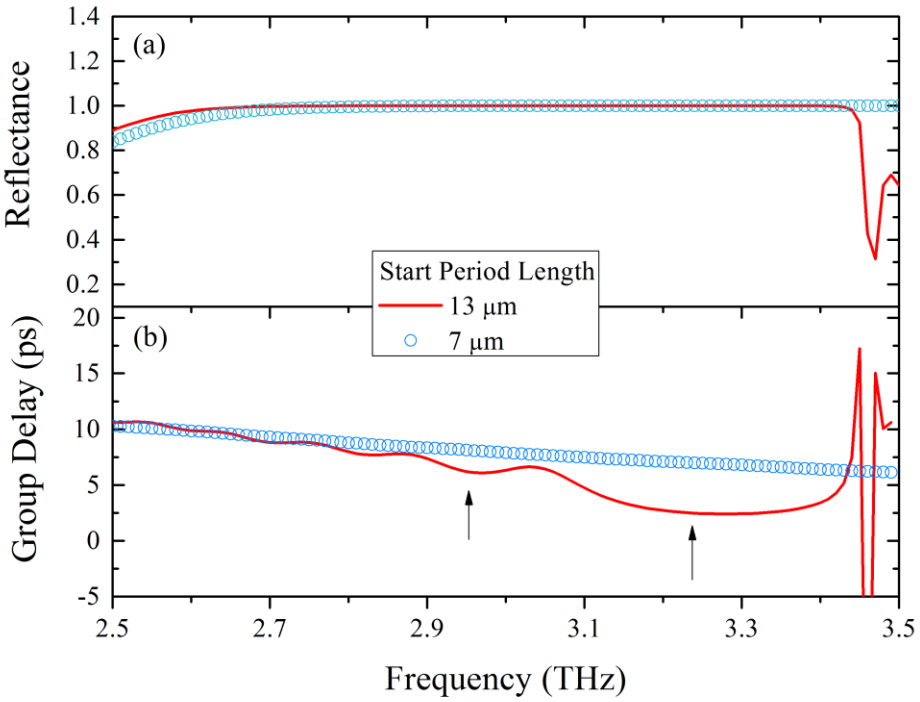

Figure 4.4 Calculated reflectance spectra (a) and group delay (b) in chirped DBR structures with different starting period lengths of 7 μm (blue circles) and 13 μm (red line). The ending period lengths of these two structures are fixed at 20 μm.

The group delay dispersion of the chirped DBR structure is calculated and presented in Figure 4.4(b) (curves in red color). At frequencies above ~3.0 THz, strong ripples (as shown by black arrows) merge on the compensation curve. When comparing the calculated group delay curve [Figure 4.4(b)] to the reflectance curve [Figure 4.4(a)], we found that such distortion in the group delay curve at higher frequencies is due to the

insufficient reflectance provided by the chirped DBR. Further investigation shows that reflectance drops at higher frequencies due to the shallow corrugation depth in the starting period region. Because the corrugating periods in the starting period region targets the reflectance of high frequency EM wave, however, the shallow corrugation depths in this region are not able to reflect all high-frequency EM waves and cause leakage that leads to distortion on the group delay curve. To solve this problem, one strategy is to set the starting period at a shorter length in the chirped DBR structure, as discussed in Chapter 3. As shown in Figure 4.4(a), after shortening the starting period length to 7 μm, the reflection from the chirped DBR structure remains at close to unity value at 3.5 THz (blue curve). Also, the corresponding group delay curve becomes much smoother across the entire target frequency range (2.5 THz to 3.5 THz).

In order to accurately compensate the group delay dispersion generated from the flat-ridge waveguide with certain waveguide lengths, chirped DBR structures with different number of corrugation periods were simulated, as shown in Figure 4.5. All the geometric parameters (starting period length, ending period length, etc) except the number of periods are kept as constants. The calculated time delay for EM waves to travel round-trip with frequencies between 2.5 THz to 3.5 THz increases linearly with increases in the number of corrugation periods (from -3.163 ps for 40 periods to -9.523 ps for 120 periods in chirped DBR), which makes it very convenient to adjust the extent of group delay compensation by simply tuning the number of corrugation periods.

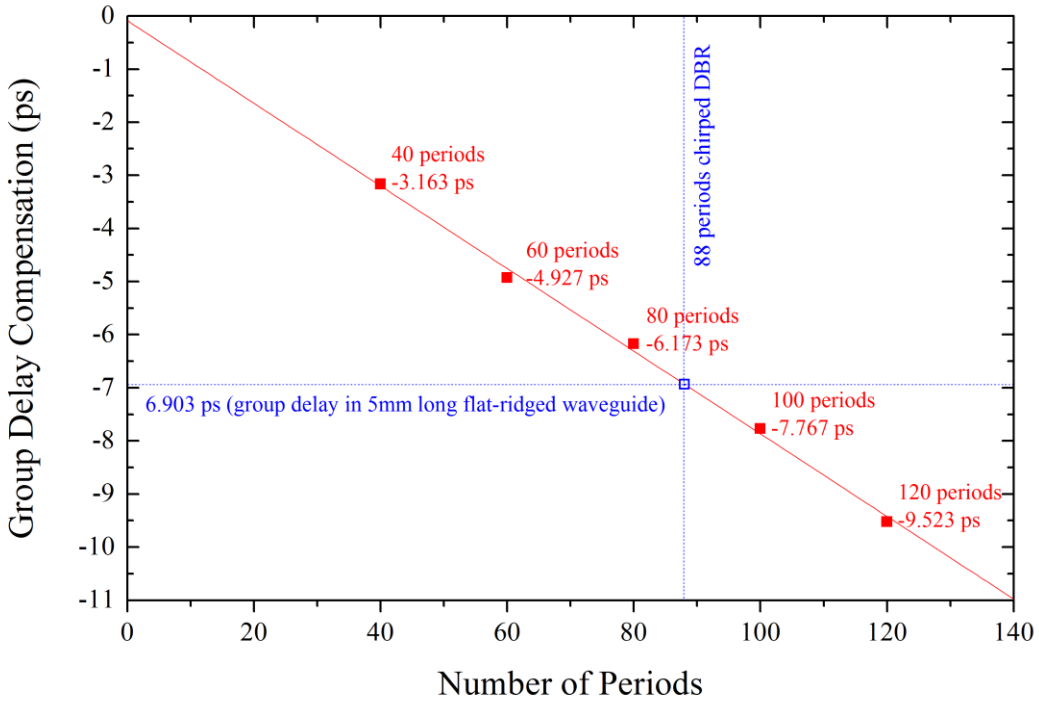

Figure 4.5 Calculated group delay compensations of EM waves after travelling round-trip with frequencies from 2.5 THz to 3.5 THz in chirped DBR structures with varying numbers of corrugation periods (solid red squares). The time delay of the group delay dispersion of a 5000-μm-long flat-ridge waveguide is marked in the figure as well (6.903 ps, blue void square). In order to compensate for such group delays in the flat-ridge waveguide, a chirped DBR with 88 corrugation periods is designed.

The calculated time delay of group delay compensation is marked as a negative value (as shown in Figure 4.5 with red solid squares) showing the one-round-trip travel time of EM waves with higher frequencies are shorter than that with lower frequencies. The negative sign is to offset the calculated group delay dispersion from the flat-ridge waveguide (in Figure 4.3). Therefore, in order to compensate for the group delay dispersion of 6.903 ps from a 5000-μm-long flat-ridged waveguide, a chirped DBR structure with 88 periods of corrugation periods is designed to ensure the whole waveguide structure has a close to zero group delay dispersion. The geometric parameters of the designed chirped DBR structure for compensating the F-series THz QCLs is listed in Table 4.1.

Table 4.1 Geometric parameters of chirped DBR for F-series THz QCLs

Starting Period length (μm)	Ending Period length (μm)	Ending period corrugation depth (μm)	Shift index	Taper index	Number of periods
7	20	9	2	1	88

4.3 Chirped DBR structures for group delay compensation in broad frequency band

4.3.1 The strategy of extending the frequency bandwidth of group delay compensation in chirped DBR structures

For a conventional DBR mirror, the strength of reflection at the corresponding frequency becomes stronger either by increasing the repeating number of the corrugation periods or etching a deeper corrugation for the periods. To examine the extent of group delay dispersion compensation for with an extended broad operation band from 2 THz to 4 THz, a series of chirped DBR structures (Sample A-F) with ridge widths of 20 μm are proposed and simulated. The key geometric parameters of the structures are listed in Table 4.2.

Table 4.2 Geometric parameters of chirped DBR structure Samples A-F

Structure Number	Starting Period Length (μm)	Ending Period Length (μm)	Number of Periods	Starting Period Corrugation Depth (μm)	Ending Period Corrugation Depth (μm)
Sample A	10	26	30	0	8.5
Sample B	10	26	35	0	8.5
Sample C	10	26	40	0	8.5
Sample D	10	26	30	1	8.5
Sample E	10	26	30	2	8.5
Sample F	10	26	30	3	8.5

Samples A, B, and C are chirped DBR structures that share the same parameters, except the number of corrugation periods (thus the total length). Samples A, D, E, and F are almost identical except the starting corrugation depth. The starting period length in these six DBR designs is 10 μm, which corresponds to an upper reflection cutoff frequency of ~ 4 THz, as shown in Figure 4.6.

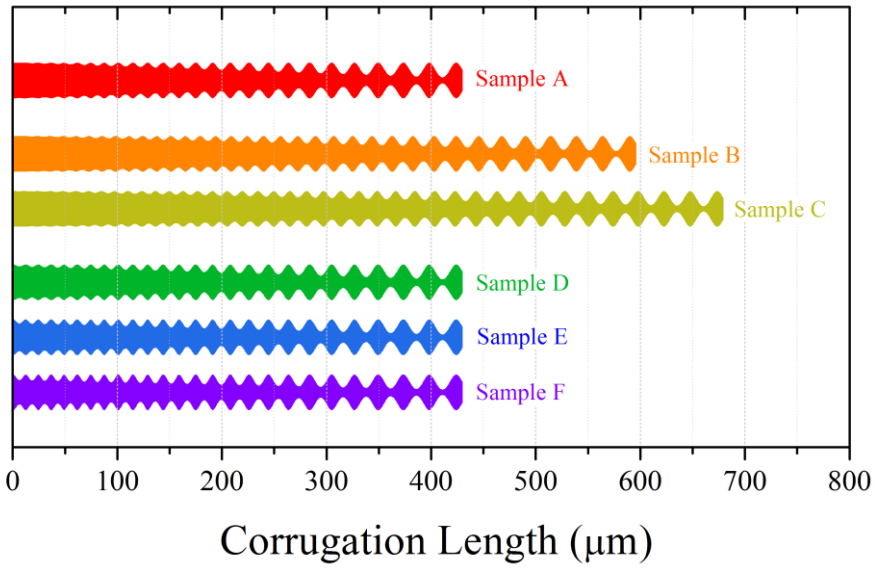

Figure 4.6 Six 20-μm-wide chirped DBR structures are simulated using the 1D model. Sample A (red) is set as a baseline sample with the following parameters: starting period length (10 μm), ending period length (26 μm), number of periods (30), ending period corrugation depth (8.5 μm), and starting period corrugation depth (0 μm). Sample B (orange) and Sample C (yellow) have the same parameters as those in Sample A, except the number of periods (35 periods in Sample B and 40 periods in Sample C). Sample D (green), Sample E (blue), and Sample F (purple) have the same parameters as those in Sample A, except the starting period corrugation depth (1, 2, and 3 μm for Sample D, Sample E, and Sample F, respectively).

Figure 4.7(a) shows that the calculated reflectance of Sample A (red) drops to ~70% at ~ 3.2 THz, leading to a much-narrower-than-expected reflection band. This is because the corrugation of the first few periods in the starting period region of the chirped DBR structure are too shallow (starting from 0 μm), and the resultant reflectance at higher

frequencies is therefore very weak or even negligible. To overcome this deficiency, two different designing strategies were investigated, namely: -increasing the number of the periods and implementing deeper corrugation.

As shown in Figure 4.7(a), by increasing the period number to 35 (in Sample B) and 40 (in Sample C), the reflection band is extended moderately to higher frequencies (up to ~3.4 THz at ~70% of the reflectance), confirming that a larger number of corrugation periods helps strengthen the reflection and push the upper cutoff frequency to higher frequencies. However, the period number has to be much larger than 40 to further push the upper cutoff frequency to 4 THz. This would inevitably lead to a very long DBR cavity and introduce excess group delay dispersion within the target frequency range.

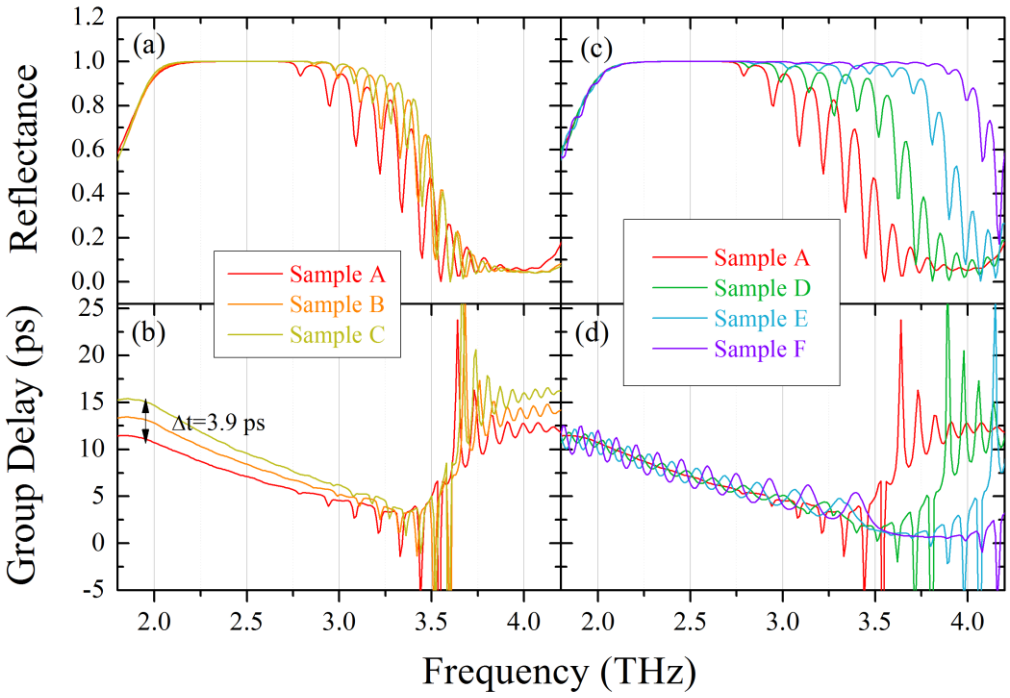

Figure 4.7 (a) The calculated reflectance spectra of Sample A (red), Sample B (orange) and Sample C (yellow). (b) The calculated group delay of Sample A (red), Sample B (orange) and Sample C (yellow). A difference of ~3.9 ps in group delay compensation between Sample B and Sample C is shown. (c) The calculated reflectance spectra of Sample A (red), Sample D (green), Sample E (blue) and Sample F (purple). (d) The calculated group delay of Sample A (red), Sample D (green), Sample E (blue) and Sample

F (purple).

The calculated group delay curves for Sample A, B, and C are plotted in Figure 4.7(b), which show a monotonic decrease in the corresponding reflection band. Note that longer DBR structures introduce larger group delay differences between the lower and higher frequencies. The longest structure (Sample C) introduces an additional 3.9 picoseconds of group delay by comparison with the shortest structure (Sample A). As revealed in Figure 4.1(b), the material group delay over the frequency range is predetermined by material properties and is fixed, while the waveguide group delay increases with the length of the DBR structure. As such, increasing the period number may partially address the insufficient reflection issue at higher frequencies, but it is unlikely to achieve exact dispersion compensation.

An alternative approach is to implement chirped DBRs with deeper corrugation depth, particularly at the starting periods. Figure 4.7(c) compares the calculated reflectance curves of the four chirped DBR structures with identical parameters except the starting period corrugation depths, which are 0 μm for Sample A (red), 1 μm for Sample D (green), 2 μm for Sample E (blue), and 3 μm for Sample F (purple). The upper-limit cutoff frequency (at ~70% of the reflectance) of the reflectance band is effectively extended from ~3.2 THz to ~3.5 THz, ~3.8 THz, and ~4.1 THz as the corrugation depth of the starting period increases from 0 to 3 μm. Clearly, by modifying the corrugation depth to 3 μm in the starting period of the chirped DBR, the reflection band can extend to meet the range, from 2 to 4 THz. It seems the implementation of deeper corrugation is a good solution. However, deeper corrugation of the DBRs also generates a substantial and detrimental side effect. Figure 4.7(d) shows the calculated group delay curves of Sample A, Sample D, Sample E, and Sample F. Over the frequency range within its reflection band, the group delay curve of Sample A is monotonically decreasing and almost smooth. Starting with Sample D, periodic ripples can be observed in the group delay curves in the frequency range of interest even though the overall decreasing trend is retained. Modulation of the periodic ripples becomes stronger as the corrugation depth of the DBRs increases. These periodic ripples clearly disrupt the GVD compensation as the material group delay can be

cancelled out only at some discrete frequencies.

4.3.2 Two-section chirped DBR structures

The ripples observed in Figure 4.7(d) can be explained by the Gires-Tournois interferometer effect. At the interface between the flat rectangular waveguide section and the chirped DBR section (see the Sample G blue curve in Figure 4.8), there is an abrupt change in effective refractive index. This discontinuity yields the formation of an internal cavity, leading to the emergence of ripples (the fast modulations in the group delay curves). To minimize the ripples, one should eliminate the refractive index discontinuity. One effective approach is to insert a buffer structure between the flat rectangular waveguide section and the chirped DBR section. The buffer structure is a linearly-chirped DBR in which the corrugation depth of the starting period is zero [see the Sample H red curve in Figure 4.8].

The Sample H structure consists of two sections – a short chirped DBR structure with its corrugation depth linearly increasing from 0 to 4 μm (buffer section) and a much longer chirped DBR, attached right behind the buffer section, with a starting period corrugation depth of 4 μm (compensation section). The compensation section ensures that strong reflectance is achieved over a wide frequency range, while the buffer section provides a transition to eliminate the abrupt change in refractive index and thus minimizes the ripples in the group delay curve. Simulation results confirm these benefits. Ripples in the group delay curve almost completely eliminated in Sample H (as shown in Figure 4.9 (a)).

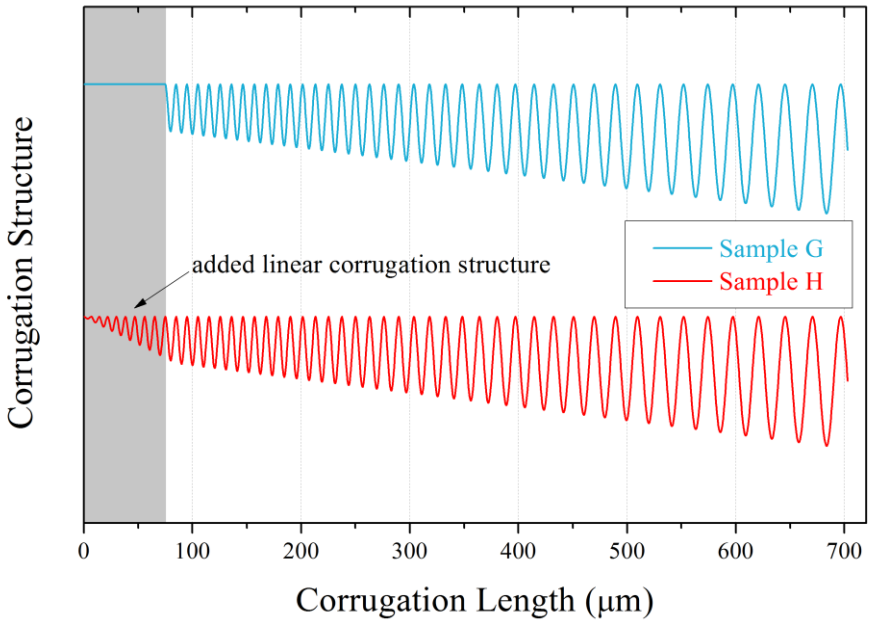

Figure 4.8 Comparison of the corrugation shape of two 20-μm-wide chirped DBR Sample G and H. These two structures share the same parameters, including starting period length (10 μm), ending period length (26 μm), number of periods (40), starting period corrugation depth (4 μm), and ending period corrugation depth (8.5 μm). However, different from Sample G, Sample H has an additional 10 periods of corrugations as a transition buffer from the flat-ridge section to the chirped DBR section.

A group of two-section DBRs similar to SH has been simulated. The number of periods (N) in the buffer section of these DBRs increases from 3 to 15, while the structures of their compensation sections remain unchanged. By increasing the period number, the ripples in the calculated group delay curves quickly diminish and the modulations of group delays (which is defined by the standard deviation of the calculated group delay data that deviate from a fitted smooth group delay curve) drops from 0.33 ps (for N=3) to ~0.07 ps (for N=15) (as shown in Figure 4.9(b)). Simulation results clearly reveal that such a two-section DBR with a period number of N=10 in the buffer section produces a satisfactorily smooth group delay curve (with a deviation of 0.1 ps) in the octave frequency range of 2 to 4 THz.

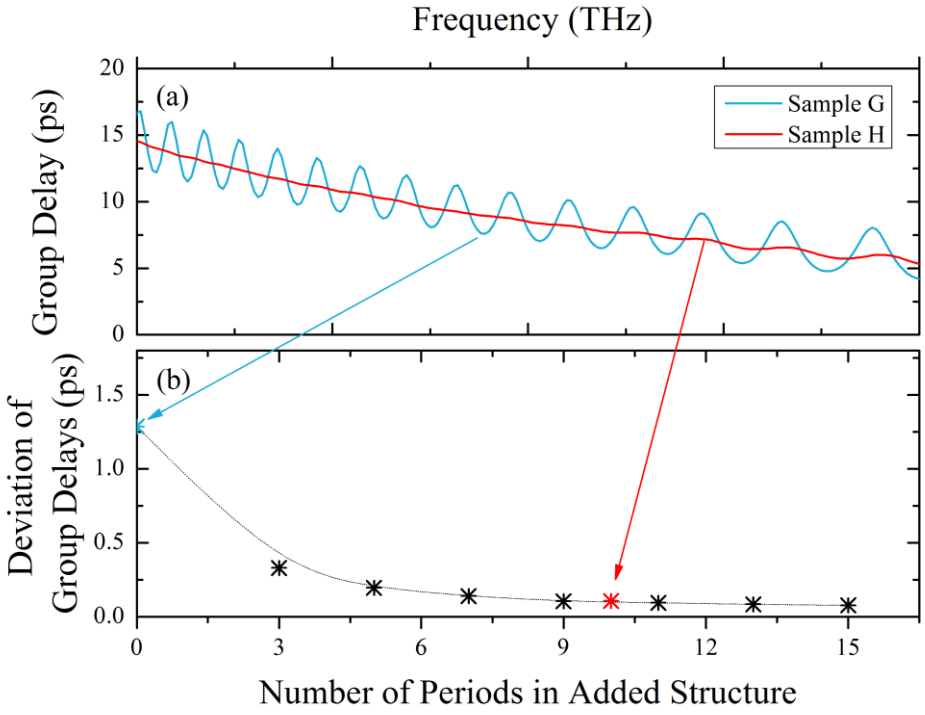

Figure 4.9 (a) Calculated group delay of Sample G (blue) and Sample H (red). The buffer region provides Sample H with a smoother group delay curve between 2 THz and 4 THz with less modulation, but still retains the same decaying trend (~7 ps) as that in Sample G. (b) Calculated modulations of the group delays within the frequency band for DBR structures with different number of periods in the buffer region. All other geometric parameters are the same as those in Sample H.

Although the above results obtained from the transfer matrix method present a basic understanding of chirped DBRs in terms of group delay compensation in a metal-metal THz waveguide, the 1D model is oversimplified for simulating the EM wave transmission processes. In particular, the 1D model can't predict at all the impact of the less-than-unity confinement factor on DBR's reflection and dispersion performance. It simply assumes a uniform mode distribution inside the waveguide. As a result, the effective refractive index contrast in the corrugated section of the chirped DBR is overrated in the 1D model, which leads to overestimation of the calculated reflectance. In this regard, a 3D model should be employed to improve simulation accuracy and finalize device design parameters.

As discussed in Chapter 3, 3D model based on COMSOL RF package is used to simulate the chirped DBR structures discussed above. Three chirped DBRs (Sample I, Sample J, Sample K), with a thickness of 10 μm and a ridge width of 20 μm, are designed and simulated using the 3D model. The dimensional parameters are listed in Table 4.3.

Table 4.3 Geometric parameters of Sample I, J, and K for the 3D model in COMSOL.

Structure	Starting Period length (μm)	Ending Period length (μm)	Number of Periods	Starting Period Corrugation Depth (μm)	Ending Period Corrugation Depth (μm)	Structure Before Start Period
Sample I	10	26	30	0	9	Flat ridge waveguide
Sample J	10	26	30	6	9	Flat ridge waveguide
Sample K	10	26	30	6	9	10 Periods of buffer corrugation

The Sample K structure is a chirped DBR waveguide with a buffer section of 10 corrugations, which is 75 μm long in total. The Sample I and Sample J structures are control designs, which both include a 75 μm long flat ridge waveguide section instead of a chirped DBR buffer section. The starting period corrugation depth of Sample J is 6 μm, the same as Sample K, while Sample I has a starting period with corrugation depth of 0 μm. Figure 4.10(a) and (b) show the calculated reflectance and group delay curves of the chirped DBR structures using the 3D model. Similar to the result from the 1D model, Sample I cannot provide adequate reflection at frequencies above ~2.8 THz due to the shallow corrugation depth of its starting periods. In contrast, both Sample J and Sample K have a close-to-unity reflectance even at a frequency of 4 THz or beyond. This is more clearly revealed in the mode distribution diagram shown in Figure 4.10(c) and (d). In Fig. 4(c), at a frequency of 3 THz, only part of the EM wave is bounced back by the corrugated periods of Sample I, which occurs at the middle of the chirped DBR structure. A substantial portion of the injected EM waves leaks to the right side. However, as shown in Figure 4.10(d), EM waves at 4 THz are strongly reflected back to the left at the first quarter of the waveguide and the mode is not present on the right side, indicating close-to-unity reflectance. Although both

Sample K and Sample J yield broadband reflectance spectra, the calculated group delay curves show multiple ripples are observed in Sample J, but not in Sample K within the frequency range from 2 to 4 THz [see Figure 4.10(b)]. As discussed earlier, this distortion comes from the undesired resonance of a Gires-Tournois interferometer like cavity.

To further under this phenomenon, the mode distribution at frequencies of 2.30 THz (ripple peak), 2.37 THz (ripple valley), 2.44 THz (next ripple peak) in Sample J are calculated, as shown in Figure 4.10(e). Due to the abrupt discontinuity in the effective mode index, the interface between the flat ridge waveguide section and the chirped DBR section acts as a reflection mirror that can reflect the EM waves backward from the right side. At resonance frequencies, such as 2.30 and 2.44 THz, the EM waves can be trapped in the chirped DBR structure, which is confirmed by the higher intensity in the corresponding section [Figure 4.10 (e)]. At off-resonance frequencies, such as 2.37 THz, mode trapping is much relieved and the mode intensity is thus much lower. As such, the group delay at the resonance frequencies is greater than that at the off-resonance frequencies. By inserting a buffer section (such as the one in Sample K), the abrupt mode transition from the flat ridge waveguide section to the chirped DBR section is pretty much removed and the Gires-Tournois interferometer effect is largely eliminated. A much smoother group delay curve is obtained in Sample K.

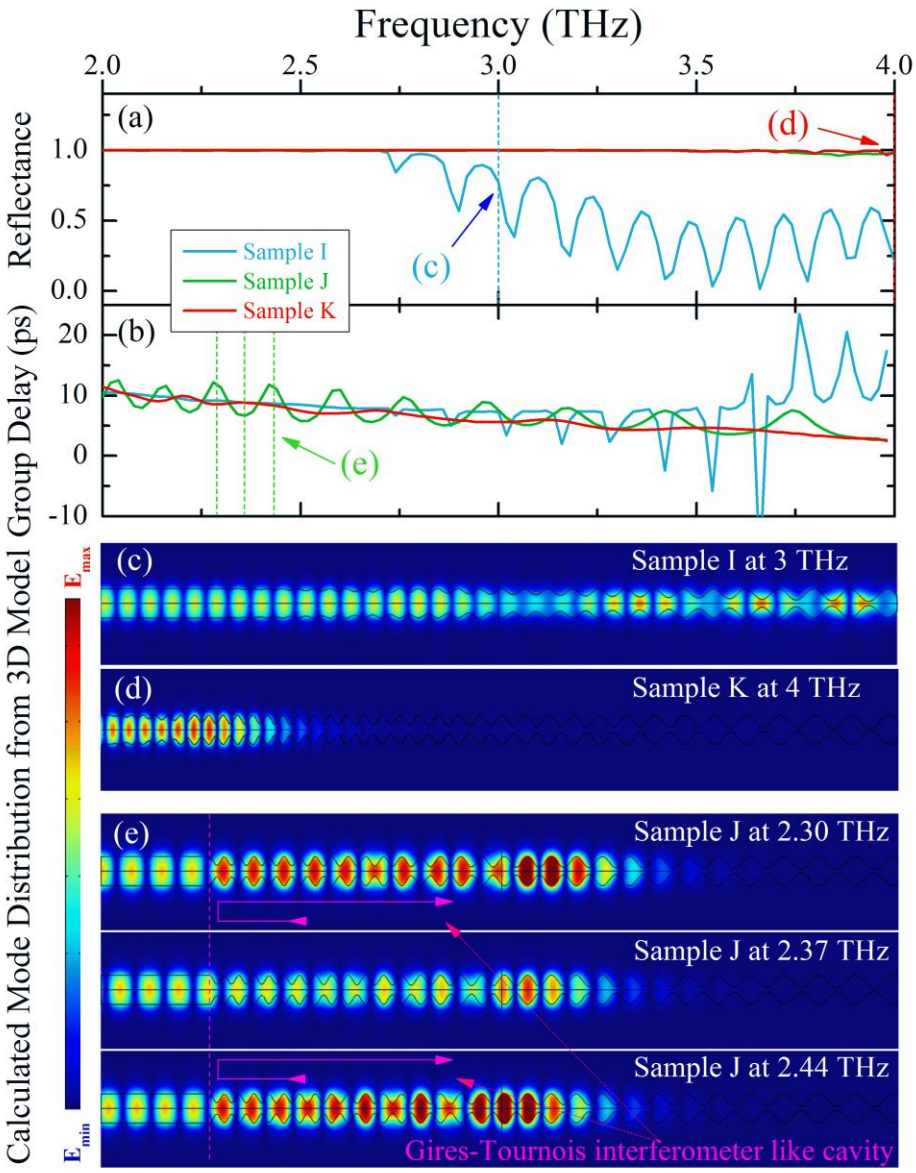

Figure 4.10 (a) Calculated reflectance spectra of three chirped DBR structures (Sample I (blue), Sample J (green), and Sample K (red)) within a frequency range of 2 - 4 THz from simulations based on the 3D model. The geometric parameters of the structures are listed in Table 4.3. Sample I only provides a sufficient reflectance frequency band from 2 THz to 3 THz, while Sample J and Sample K still have close-to-unity reflectance at 4 THz. (b)

Calculated group delay of Samples I (blue), J (green) and K (red). For Sample I, the modulation on its group delay curve appears with the frequency increasing beyond its cutoff frequency (~2.8 THz at ~70% of reflectance) from its reflectance spectra. (c) Calculated mode distribution in Sample I at 3 THz. (d) Calculated mode distribution in Sample K at 4 THz. (e) Calculated mode distribution in Sample J at 2.30 THz, 2.37 THz, and 2.44 THz corresponding to the resonance and off-resonance frequencies, labeled by vertical dashed lines in (b).

4.4 Design of chirped DBR structures for an octave frequency spanning THz QCL

4.4.1 Group delay dispersion in THz QCLs within the frequency range from 2 to 4 THz

The group delay dispersion in a flat-ridge waveguide with a cross-section area of 20 μm (width) × 10 μm (height) between frequencies of 2 THz and 4 THz is estimated in 3D COMSOL Multiphysics. By using the strategy discussed in Section 4.2, group delays in flat-ridged waveguides with different lengths (300 μm, 500 μm, and 1000 μm) are calculated, which still show a perfectly linear relationship between time delay and waveguide length. However, the amplitude of the group delay dispersion between frequencies 2 THz and 4 THz is more than two times stronger (11.177 ps between 2 THz and 4 THz compare to 5.527 ps between 2.5 THz and 3.5 THz) than that between frequencies of 2.5 THz and 3.5 THz. This phenomenon occurs because of the broader frequency spanning range, but also because of the stronger dispersion in material refractive index at a higher maximum frequency side (4 THz instead of 3.5 THz) which is closer to the reststrahlen band of the waveguide material (~8 THz).

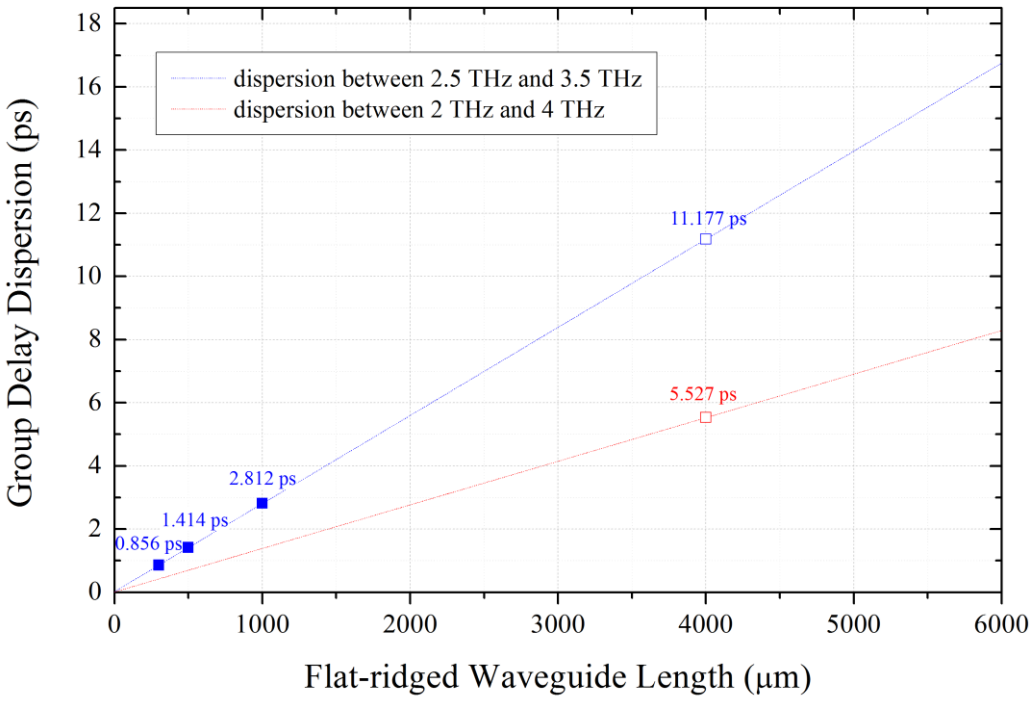

Figure 4.11 Calculated group delay dispersions of EM waves with frequencies from 2 THz to 4 THz (round trip) in the flat-ridge metal-metal waveguides with the cross-section area of 20 μm (width) × 10 μm (height) at various waveguide lengths (300 μm, 500 μm, and 1000 μm, in blue solid squares). The group delay dispersion of a 4000-μm-long waveguide is predicted (blue void square). The group delay dispersion of a 4000-μm-long waveguide between frequency of 2.5 THz and 3.5 THz is also indicated for comparison (red void square).

In this case, the much stronger GVD in octave-spanning frequency THz QCLs are more critical for achieving the comb operation, and a carefully designed chirped DBR structure that can compensate for such strong group delay dispersions is essential.

4.4.2 Design of chirped DBR structures for compensating group delay dispersions between 2 to 4 THz

In order to compensate for the group delay compensation within a broad frequency band from 2 THz to 4 THz, a series of two section chirped DBR structures are designed. As discussed in the previous section, 10 corrugation periods serve as a buffer region for the chirped DBR.

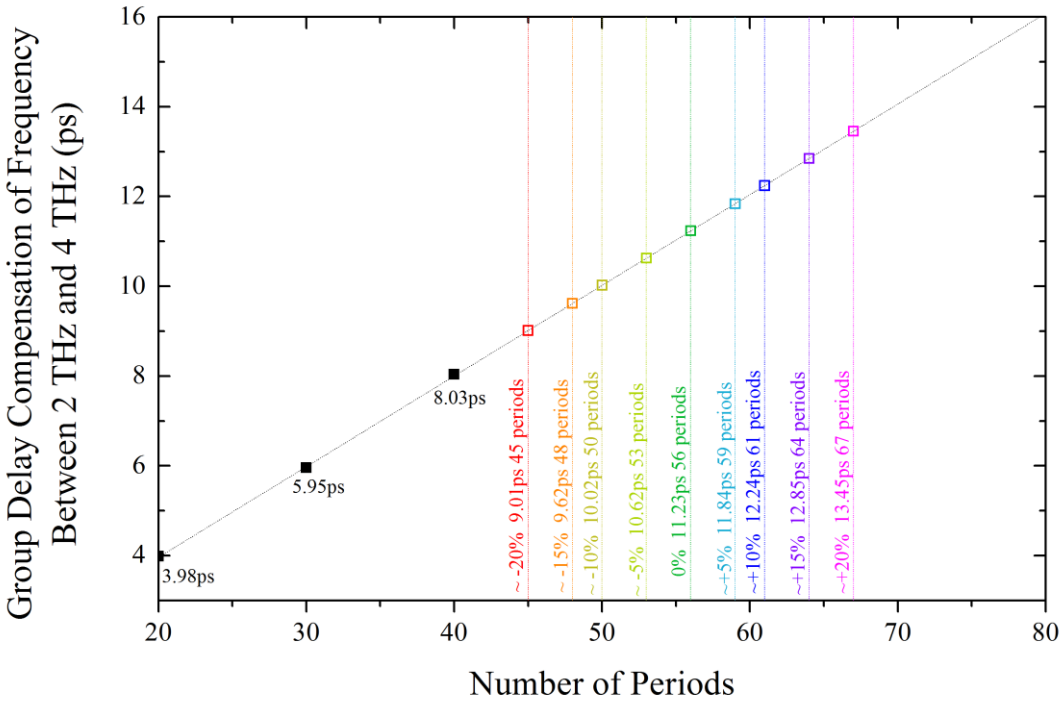

Figure 4.12 Calculated group delay compensations of EM waves with frequencies from 2 to 4 THz (round trip) in a series of chirped DBR structures with different numbers of corrugation periods (solid black squares). In order to compensate for the group delay in a 4000-μm-long flat-ridge waveguide (11.17 ps), a chirped DBR structure with 56 corrugation periods is designed to achieve ~0 ps overall group delay. In practical device fabrication, a series of two section chirped DBR structures with various group delays (-20%, -15%, -10%, -5%, 0%, +5%, +10%, +15%, and +20%, as shown with void squares in rainbow colors) covering the central group delay time (11.17 ps) are designed.

The time delay of the group delay compensation in the proposed two-section chirped DBR structure is controlled by tuning the number of periods in the compensation section, while the same buffer structure is used. In order to compensate for the group delay generated from a 4-mm-long flat-ridged double metal ridged waveguide (11.17 ps), a chirped DBR structure with 56 of corrugation periods in the compensation section is required. However, the uncertainties in the device fabrication process may interfere with the group delay dispersion in a real device. Thus nine chirped DBR structures with different numbers of corrugation periods in the compensation section are designed, which compensated for the group delay time by 9.01 ps with 45 periods (~-20%, below the targeted value), 9.62 ps with 48 periods (~-15%), 10.02 ps with 50 periods (~-10%), 10.62 ps with 53 periods (~-5%), 11.23 ps with 56 periods (~0%, exactly at the targeted value), 11.84 ps with 59 periods (~+5%, above the targeted value), 12.24 ps with 61 periods (~+10%), 12.85 ps with 64 periods (~+15%), and 13.45 ps with 67 periods (~+20%), as shown in the Figure 4.13. The geometric parameters of two-section chirped DBR for compensating broad-band THz QCLs from 2 to 4 THz (56 period structure) is listed in Table 4.4.

Table 4.4 Geometric parameters of a two-section chirped DBR for broad-band THz QCLs with frequency from 2 to 4 THz

Starting Period length (μm)	Ending Period length (μm)	Number of Periods	Starting Period Corrugation Depth (μm)	Ending Period Corrugation Depth (μm)	Structure Before Start Period
10	26	56	6	9	10 Periods of buffer corrugation

4.5 Summary

In this chapter, a chirped DBR structure is designed based on the 3D model introduced in Chapter 3, to compensate for the group delay dispersion introduced by a 5-mm-long flat

ridge metal-metal waveguide for F-series THz QCLs with their lasing frequency spanning from 2.5 to 3.5 THz based on the 3D model introduced in Chapter 3. A strategy to extend the operating frequency bandwidth of the chirped DBR structure is demonstrated by implementing deeper corrugation periods in the starting period region. Meanwhile, a novel buffer section that is located between the flat-ridge waveguide section and the chirped DBR section is proposed to eliminate the strong ripples observed in the group delay curves, which result from the abrupt transition from flat ridge waveguide to chirped DBR. Based on this strategy, a two-section chirped DBR structure was designed to compensate the group delay dispersion over an ultra-broad octave-spanning frequency range (2 to 4 THz). This structure will be deployed on the new THz QCL with heterogeneous active regions (designed in Chapter 2) to achieve comb operation.

Chapter 5

Devices Growth, Fabrication, and Characterization

Compared to the growth, fabrication, and characterization of a general THz QCL design equipped with a metal-metal waveguide [71], the various processes for developing a THz QCL comb laser are much more challenging due to the device's complicated structure and critical measurement requirements. For example, the heterogeneous structure consists of three or four different active regions, which dramatically increase the difficulty of device growth in MBE due to the increased number of parameters to be controlled and monitored during the growth. Also, a carefully modified device fabrication process is essential to making a chirped DBR waveguide that can achieve GVD compensation in a THz QCL comb laser. In the device characterization step, the RF beat note detection, as a fundamental technique for evaluating comb operation inside a THz QCL, requires a cryogenic light-current-voltage (LIV) system to support the transmission and detection of weak and high frequency (~GHz) signals. In this chapter, we present experimental results related to MBE growth, device fabrication and device characterization, and their importance towards building our first THz QCL frequency comb device.

5.1 THz QCL active region growth

Growth of THz QCL active regions for this project was undertaken in a recently built MBE system (Veecoo-GEN10) by Prof. Zbig Wasilewski's group in University of Waterloo

Quantum Nano Centre. Since the new MBE system is still under calibration and optimization, two THz QCLs were re-grown based on structures reported in the literature: 1. SA design (wafer G0216) from Prof. Sushil Kumar's group at Lehigh University [72]; 2. A heterogeneous design (wafer G0226) from Prof. Faist's group at Swiss Federal Institute of Technology in Zurich (ETH) [44]. For the MBE growth of G0216, high resolution X-ray diffraction (XRD) fitting results show the material suffered some discrepancies with the published growth parameters, where the actual grown layer thicknesses are around ~5% thinner (for both quantum wells and barriers) than our target, and the grown aluminum barrier composition was also missmatched by ~2% (17% instead of 15%). Before growth of the heterogeneous structure (G0226), the MBE system was further calibrated and optimized. Also, we modified the growth of the heterogeneous structure G0226 by shrinking the thickness to ~10 μm while keeping the ratio of the number of modules in the three different active regions consistent. The XRD fitting results match our target layer thicknesses and aluminum compositions fairly well, with maximum discrepancies of ~3% lower in layer thickness (for both quantum wells and barriers) and ~0.2% lower in aluminum compositions (14.8% instead of 15%).

5.2 Fabrication of THz QCLs

The fabrication of THz QCLs for this project was done in the Quantum Nano Centre clean-room in University of Waterloo. Before fabricating the THz QCLs for this project, the recipes for each step in the metal-metal waveguide fabrication process were tested and optimized, first on 6 dummy wafer pieces (GaAs wafer) and, subsequently, on 16 device wafer pieces (V0222-1 to 3, V0896-1 to 4, V0962-1 and 2, G0216-1 to 4, G0226-1 to 3).

5.2.1 Major fabrication steps

The MBE grown wafers were cut into ~1 cm×1.2 cm pieces (based on the size of designed

photolithography masks) and then cleaned with standard isopropanol (IPA), acetone, and deionized (DI) water to remove the organic contaminations. The cleaning step was followed by an oxidation removal process with HCl: H_2O (1:10) dip and a 5 min oxygen plasma treatment, in which the top surface (with MBE grown structure) was coated with a Ti/Au (200/2000Å) metal layer by electron-beam deposition. The deposited metal layer was then thickened up to 1 μm with gold through electro-plating with 434 RTU solution, and, then flipped and placed on top of an Indium coated (1 μm thick) GaAs carrier wafer piece (also called "receptor") for subsequent wafer bonding processing. The flipping and placing process requires extreme attention in order to: 1. align both edges (cleaved crystal lines) of the device wafer piece and the carrier wafer piece for subsequent cleaving of laser facet. 2, maintain the cleanness of both the attached surface, eliminating small contaminating particles, which may result in failure of the following fabrication steps. (e.g., V0962-1 was detached during the following surface lapping process due to this problem)

The thermal-compression wafer bonding (Au-In) step was done on a TRESKY die bonder (T-3000-FC3) under 0.5 MPa pressure at 250℃ for 1 hour. Different processing temperatures and times have been tested for the step. To avoid over-diffusing Indium into the active region of the device, the bonding temperature needs to be controlled below 350℃ (for our process). After the wafer bonding step, the 600-μm-thick GaAs substrate of the device wafer is thinned down to less than 100 μm thick by mechanical lapping, as shown in Figure 5.1.

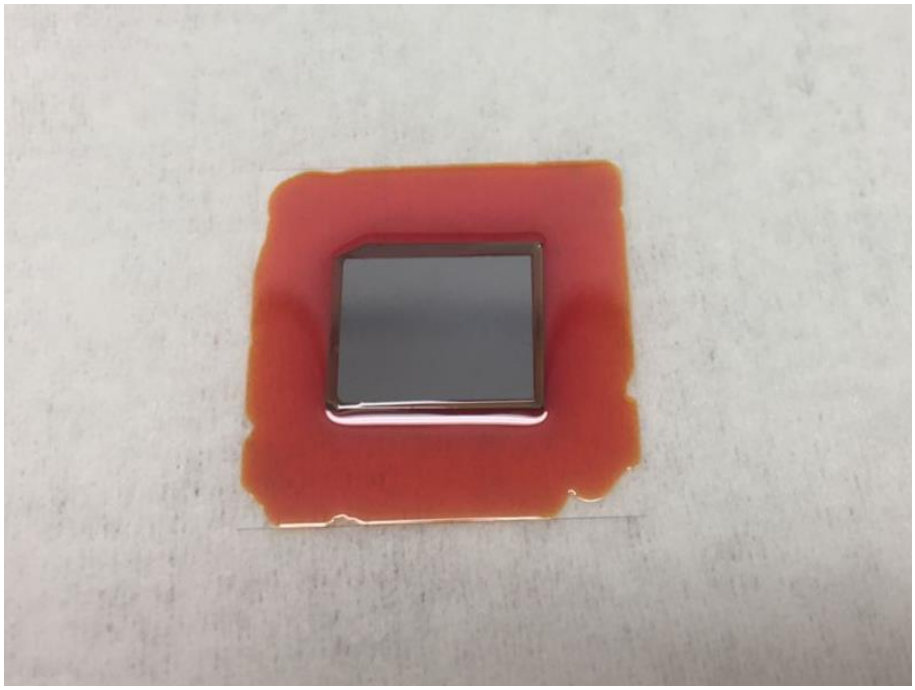

Figure 5.1 The device wafer piece with its substrate lapped to ~100 μm thick. The sidewall of the device's wafer is protected by a photoresist to prevent damage in following removal (wet etching) step.

The rest of the GaAs is removed through selective wet etching with a solution of citric acid: Hydrogen peroxide=5:1 (etch rate ~3000 Å/min). During the wet etching process, the side wall of the device wafer must be carefully protected by a photoresist to prevent destructive etching into the active region. The selective wet etching stops at the pre-grown etch stop layer ($Al_{0.55}Ga_{0.45}As$ or $Al_{0.97}Ga_{0.03}As$), and a shining surface is exposed. To maintain a uniform etching rate on the surface of the substrate and prevent damage to the etch stop layer, the solution must be under constant agitation through mild stirring. The successfully exposed etch stop layer shows a rainbow color as shown in Figure 5.2. The etch stop layer is then removed using concentrated hydrofluoric acid in 60 sec.

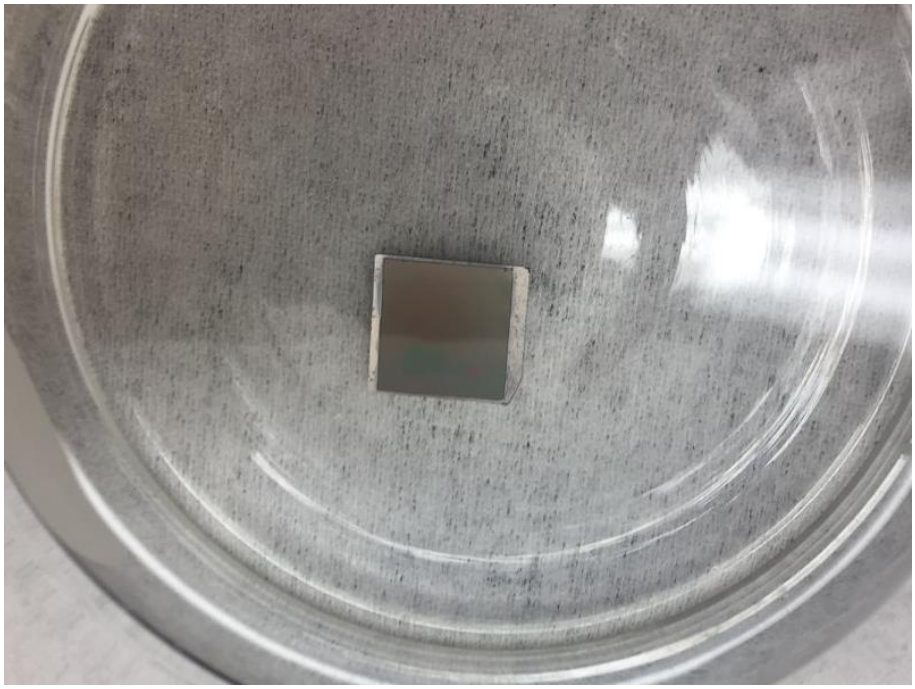

Figure 5.2 The device wafer piece with its substrate removed through wet etching. The surface shows a rainbow color.

The next step of the fabrication process is to define the metal-metal waveguide ridge on the device wafer piece through photolithography and metallization process. The photolithography mask that is designed for top metal deposition is used to pattern a bi-layer photoresist of 500 nm PMGI SF7 (lift-off resist) and 1400 nm S1811 (imaging resist). The bi-layer photoresist benefit for the following gold lift-off process, and protects the remaining gold pattern (top metal of the ridge). The bi-layer is then exposed by Suss MA6 for 5 s and developed through MIF 319 (60 s)/DI water procedure. Ti/Au (200/2000Å) is then deposited on top of the patterned photoresist, and lifted-off using PG-Remove at a temperature of 60 °C. The resulting pattern is shown in Figure 5.3.

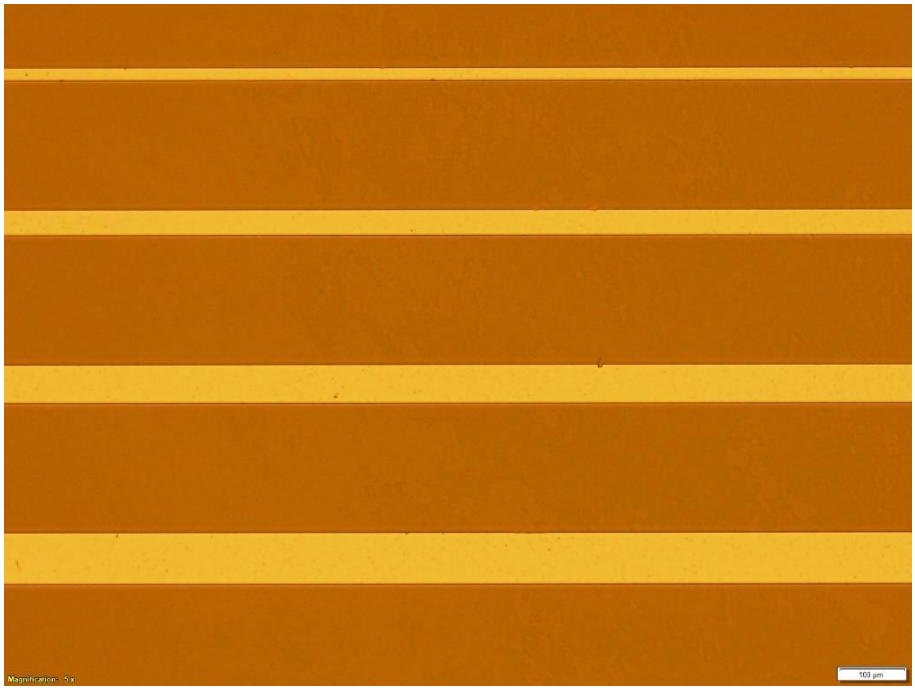

Figure 5.3 Microscopic view of the gold pattern, which becomes the top metal layer after the lift-off process. The widths of the 4 mesa ridges are 80, 60, 40, and 20 μm from bottom to top in the figure.

In order to define the mesa of the THz QCL, the AZP4621 was used as a mask material for the mesa ridge dry etching process. It is reported that the patterned top gold layer can be used as a self-aligned mask for mesa ridge etching [73][74], however, over-etching and re-deposition of the metallic layer were observed during the above process. Thus, we took the decision to use a thick layer of photoresist (AZP4621) as a mask instead. Since the AZP4621 layer will thin down during the dry etching, a14-μm-thick of AZP4621 was spun onto the wafer piece in order to guarantee the protection of the mesa beneath the mask during the dry etching process. The AZP4621 is then patterned through a second photolithography process with careful alignment of the ridge pattern, and the wafer piece is then cleaned by Oxygen plasma (5min) and prepared for the mesa ridge reactive ion etching (RIE) dry etching step.

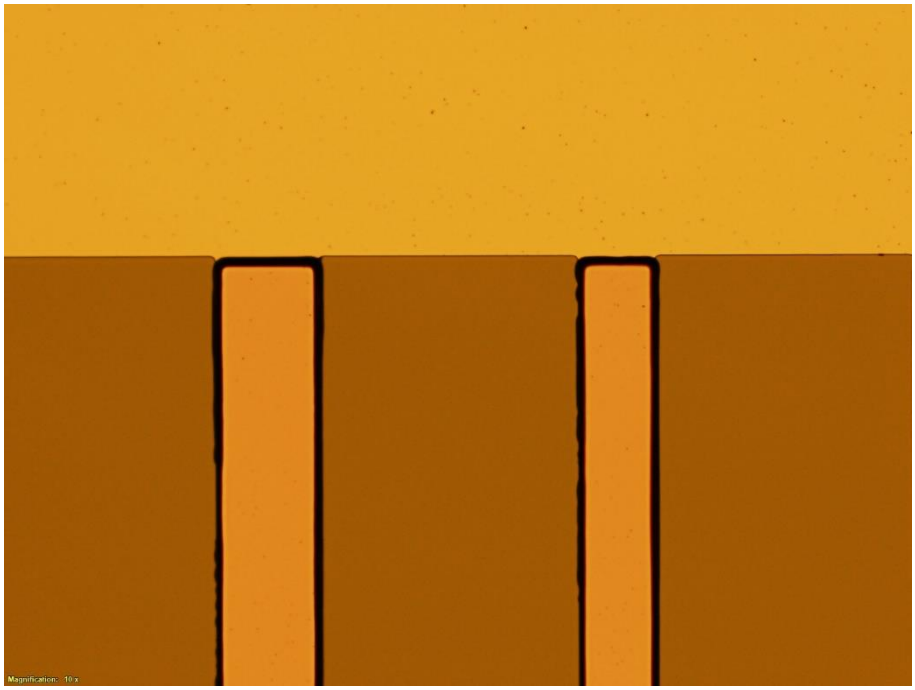

Figure 5.4 Microscopic view of patterned AZP4621, which serves as a mask for the RIE dry etching process.

5.2.2 Test of RIE dry etching for mesa ridge

The RIE dry etching process for our THz QCL mesa ridges was done using the Oxford Plasmalab System 100 ICP380 III-V & Metal chlorine etcher. The goal of this process is to etch 10-μm-deep active region with a smooth and vertical sidewall. The etching rate is not a critical parameter because the beneath In-Au bonding layer beneath the top layer will serve as an inherent etch stop layer. After several rounds of dry etching tests, two out of seven tested recipes were chosen to be used for our devices.

Table 5.1. Recipe of RIE dry etching on mesa ridges (high etching rate)

RF power (W)	ICP power (W)	Pressure (mTorr)	Temperature (℃)	Gas flow rate (sccm)	Time (sec)
200	600	5	10	BCl_3:50	30
115	600	7	10	Cl_2:80,BCl_3:30	180

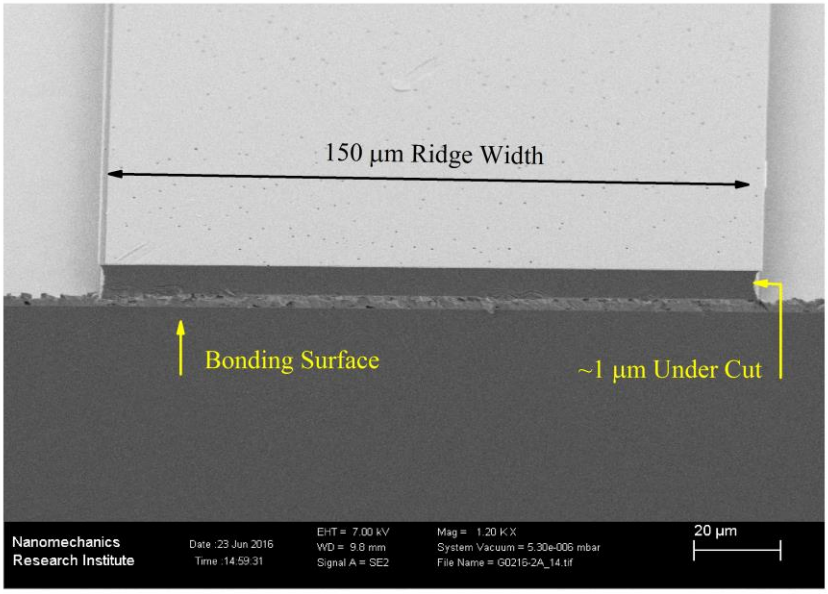

Figure 5.5 SEM picture of THz QCL G0216-2, taken after the RIE dry etching process on the mesa ridge (recipe from Table 5.1). The mesa ridge is 150-µm-wide with a slight undercut of around 1 µm at the two sidewalls.

The first successful recipe for RIE dry etching is listed in Table 5.1. which shows the advantage of a fast etch rate (~1.6 µm/min), while maintaining a small undercut at the sidewalls, as shown in the scanning electron microscope (SEM) picture of Figure 5.5. The 1 µm undercut at the sidewall region is acceptable for conventional wide-ridge THz QCLs because the EM mode inside the waveguide can barely reach the sidewall region [75]. However, for THz QCLs with narrow mesa ridges and chirped DBR structures, a 1 µm undercut might degrade the THz QCL performance.

Table 5.2. Recipe of RIE dry etching on mesa ridge (low etching rate)

RF power (W)	ICP power (W)	Pressure (mTorr)	Temperature (℃)	Gas flow rate (sccm)	Time (sec)
50	400	4	10	BCl_3:25, Ar:5	>4600

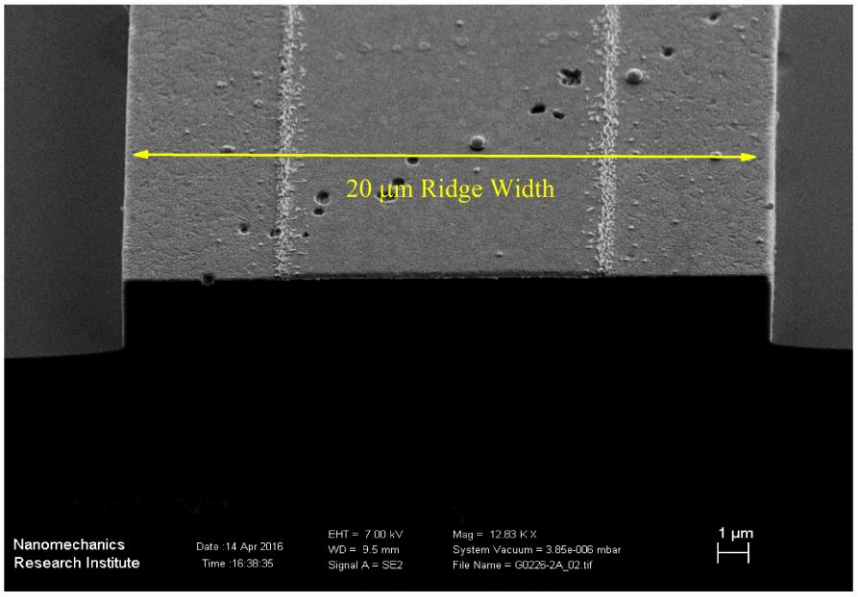

Figure 5.6 The SEM picture of THz QCL G0226-2, taken after a RIE dry etching test on mesa ridges (recipe listed in Table 5.2). The mesa is 20-µm-wide with perfectly vertical and smooth sidewalls. The etched depth is around 4.2 µm.

The second successful recipe is listed in Table 5.2. Different from the first recipe, this one has a slow etching rate (~0.13 µm/min) due to the low RF power, but provides a perfectly smooth and vertical sidewall on the mesa ridge, as shown in the SEM picture in Figure 5.6. However, etching time to achieve a 10-µm-deep mesa ridge is quite lengthy (~80 min), there is a chance the plasma chamber may become contaminated, which may degrade the quality of the mesa sidewall. Thus, the recipe can be further optimized to become one of the best candidates for RIE dry etching for our chirped DBR structure in future.

5.2.3 Device packaging and wire bonding

After the RIE dry etching process, the device is cleaned with PG Remove to remove the remaining AZP4621 photoresist. The device is then cleaved into ~1-mm-long laser bars, and Indium is bonded onto the homemade copper carrier package with the emission facet

of the laser ridge placed at the edge. Gold wires (Ø=15 μm) are bonded from the top gold metal layer of the device mesa to the pins on the package with K&S 4523 wire bonder, as shown in Figure 5.7.

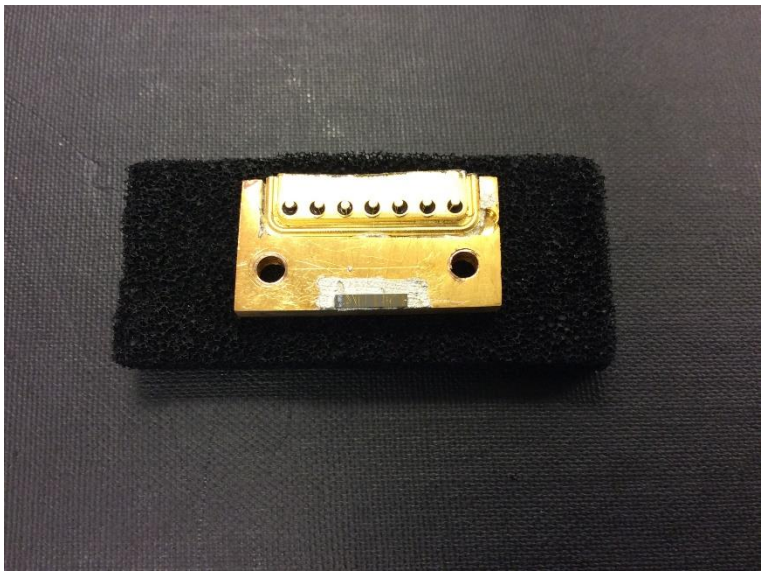

Figure 5.7 One laser bar is mounted on the homemade copper package with 7 pins. Six devices (mesa ridges) are wire-bonded to the pins, and the most-left pin serves as the ground.

5.3 Light-current density-voltage measurement of THz QCLs

The temperature dependent light-current density-voltage (LJV) measurement is a fundamental technique for characterizing the performance of a THz QCL, in which, the current (or current density) and the output power of the device are collected at different electric fields and different temperatures. The conventional setup for LJV measurement usually consists of a temperature controlled cryostat chamber with a cold finger for mounting the THz QCL, an electronic circuit for injecting the current to and reading the voltage from the THz QCL, and a THz wave detection system, called a Golay cell or bolometer. However, the LJV measurement for characterizing THz QCLs with comb operation has a much more critical experimental requirement. For example, in order to reduce the noise from the electrical power source, comb THz QCLs are always tested in

CW mode, which requires a much higher cooling power and temperature stability for the cryostat. Furthermore, the detection of RF beat notes generated from THz QCLs, which help monitor comb operation, requires that the electric circuit maintain a low loss to the signal in the gigahertz frequency band. In addition, an external feedback circuit may be added to the LJV system to further stabilize the THz QCL comb operation [45].

5.3.1 High power cooling system design

To achieve CW operation in our THz QCLs, a LJV system was built based on a high power cryostat (Zephyr CH-110), which provides strong cooling power (~20 W) at a temperature of 20 K. In addition, a high power disk heater was designed for this system to provide a sufficient temperature tuning range, as shown in Figure 5.8. The connection parts and cold finger were milled with oxygen- free high conductive copper, and carefully designed to incorporate the device mounting structure, circuit board, and temperature sensors.

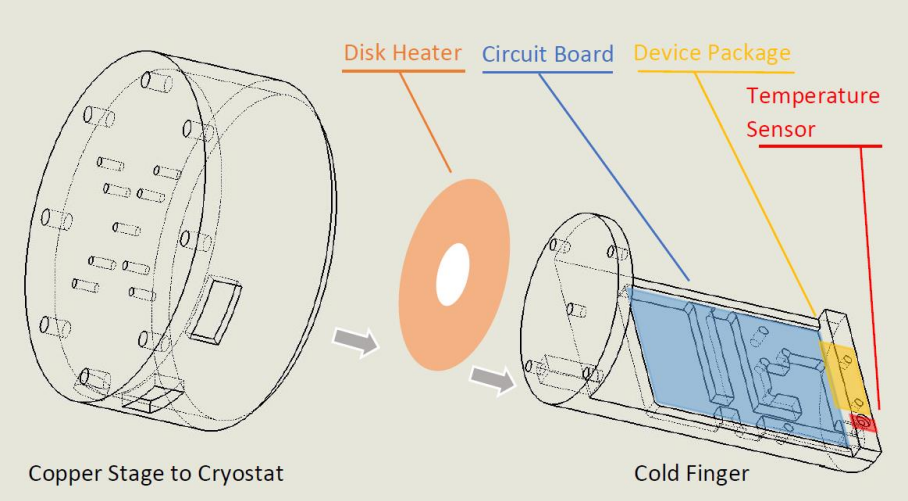

Figure 5.8 Schematic of homemade cold finger, the copper stage, disk heater and circuit board mounted on the new cryostat. The temperature sensor is placed close to the device package to ensure accurate temperature readings.

To test the new system set up, we deployed LJV measurements on FL175 MM3 (grown and fabricated from Qing Hu's group at MIT [76]) in CW mode. The measurements

were done in both the old cryostat (DE202 NE ARS) and the newly- built cryostat (Zephyr CH-110), as shown in Figure 5.9. For the measurement in DE202 NE ARS, the heat sink temperature begins to increase from the target temperature of 10 K at an electrical power injection of 0.56 W (0.07 A at 8 V in CW mode) due to the limited cooling power of the cryostat, and reaches 60 K at the threshold condition of the THz QCL with an electrical power injection of 3.3 W (0.3 A at 11 V in CW mode). However, for our newly built cryostat (Zephyr CH-110), the heat sink temperature was stabilized at 25 K of the target temperature even at the maximum power injection, which indicated our system convincingly achieved temperature stability.

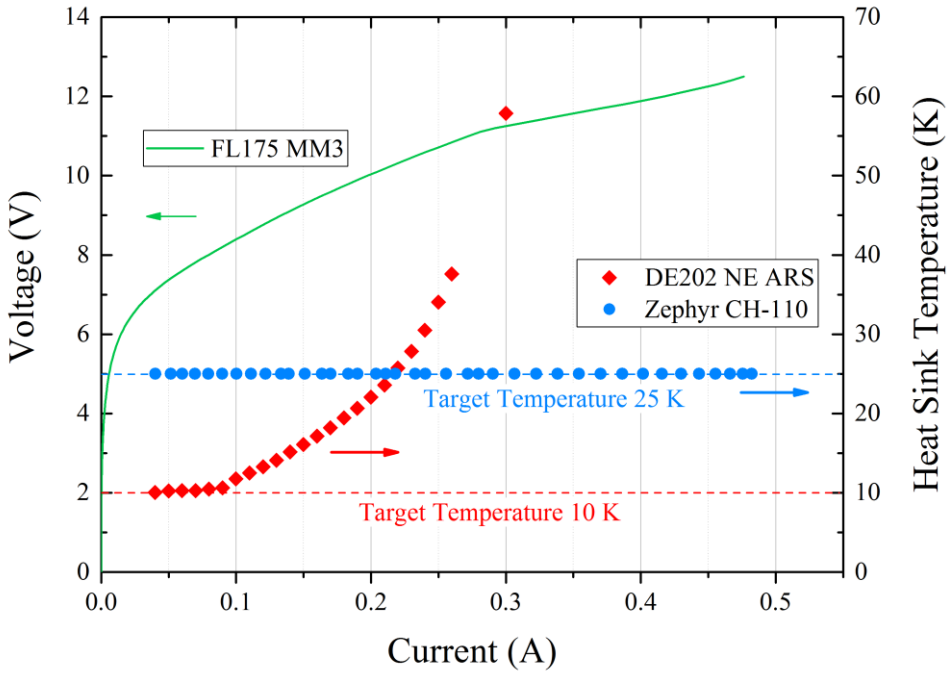

Figure 5.9 IV measurement results (green curve) and heat sink temperature readings (blue spots) of THz QCL FL175 MM3 during temperature stability testing in the newly built cryostat (Zephyr CH-110). For comparison, the heat sink temperatures of an IV measure from the same device when deployed in the old cryostat (DE202 NE ARS) are also plotted (red diamonds).

5.3.2 System optimization for RF beat note detection

In the cavity of a THz QCL, if two lasing modes with different optical frequencies are superimposed, then a beat note signal equal to the difference of the optical frequencies can usually be generated. Since the linewidth of the beat note is sensitively related to the correlation of the phase noise of the two lasing modes, a perfect optical frequency comb THz QCL with multiple pairs of phase stabilized lasing modes will generate a beat note signal with strong amplitude and narrow bandwidth [44][45][77]. Therefore, characterizing the beat note signal becomes one of the most effective and convenient methods to monitor comb operation. The frequency of the beat note signal is inversely proportional to the length of the waveguide. For a metal-metal waveguide designed for comb THz QCLs, with the usual length of 3~6 mm, the generated beat note signal is around 5~14 GHz. In order to extract this weak RF beat note signal from the laser cavity without interfering with the injection of pumping current (suppose in CW mode), a bias tee can be used in the circuit [78][79], as shown in Figure 5.10.

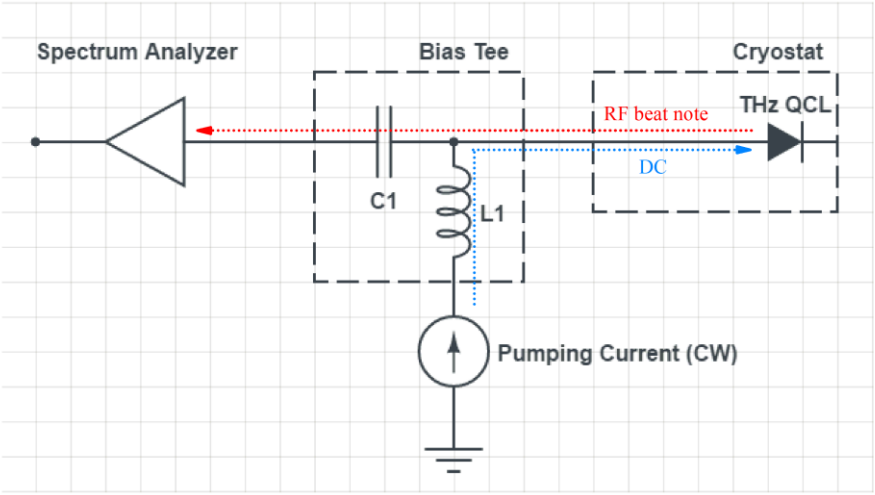

Figure 5.10 RF beat note detection set up in a LJV system. A bias tee is used to extract the RF signal from the THz QCL without interference with the pumping current (DC).

However, in typical LJV measurement setup, the already weak beat note signal may suffer additional loss during the transmission from the device package to the spectrum analyzer. Even for some reported successful measurements, the power of the collected beat

note signal is low (at a level of -90 dBm [44]). Therefore, the circuit board and the electrical feedthrough of our LJV system were carefully designed to reduce transmission loss in our target frequency band (5~8 GHz).

Mounted on the cryogenic chamber, the electrical feedthrough serves as a connection between the inner circuit board and the outer measurement instruments. The original electrical feedthrough, which only works for the signal transmission in a frequency range from DC to ~kHz, will bounce the input signal back with a frequency higher than 5 GHz. The structure was then optimized, which dramatically decreased signal transmission loss from ~ -30 dB to ~ -5dB in the high frequency region, as shown in Figure 5.11.

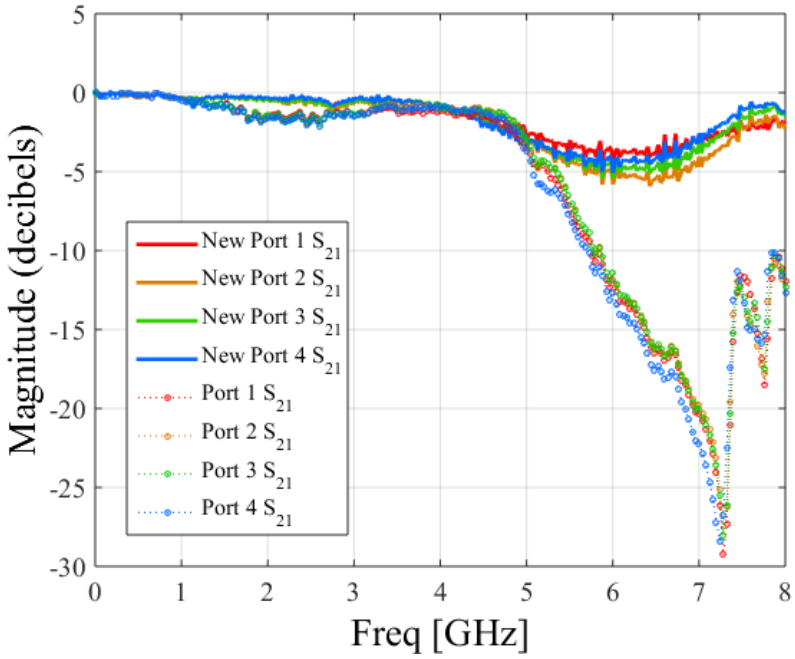

Figure 5.11 Transmission loss measurements from 4 independent electrical feedthrough ports in the new LJV system, based on an S-parameter scan taken using an Agilent network analyzer.

The electric circuit board, which collects the signal from the device package and feeds it into the cables, is another major origin of RF loss in the signal transmission line. Figure 5.12 shows the circuit board based on the knowledge of stripline in RF circuits, which matches the characteristic impedance of 50 Ohm at a frequency of 8 GHz. The

calibrated RF loss in the whole transmission line, from the pins on the package to the electric feedthrough ports, is also shown in Figure 5.12. Apart from the inevitable package induced ~12 dB loss at frequency regions above 6 GHz, the whole transmission line demonstrates a low transmission loss within 0~8 GHz, which provides an important support to our future measurements on comb THz QCLs.

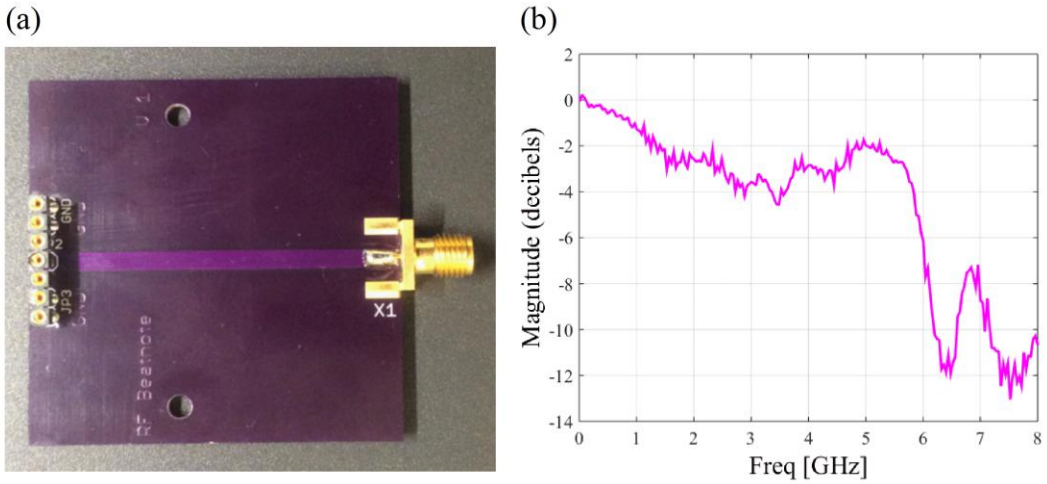

Figure 5.12 (a) Circuit board designed for mounting the device package in the LJV system for THz QCL measurement. (b) Measured transmission loss of the circuit board in (a), based on a S-parameter scan taken using an Agilent network analyzer.

5.4 Pulse-mode LJV measurement results

In order to check the quality of both the wafer growth and the metal-metal waveguide fabrication process for our THz QCLs, I took the pulse-mode LJV measurements on THz QCLs G0216 and G0226. The schematic diagram of the measurement setup is shown in Figure 5.13.

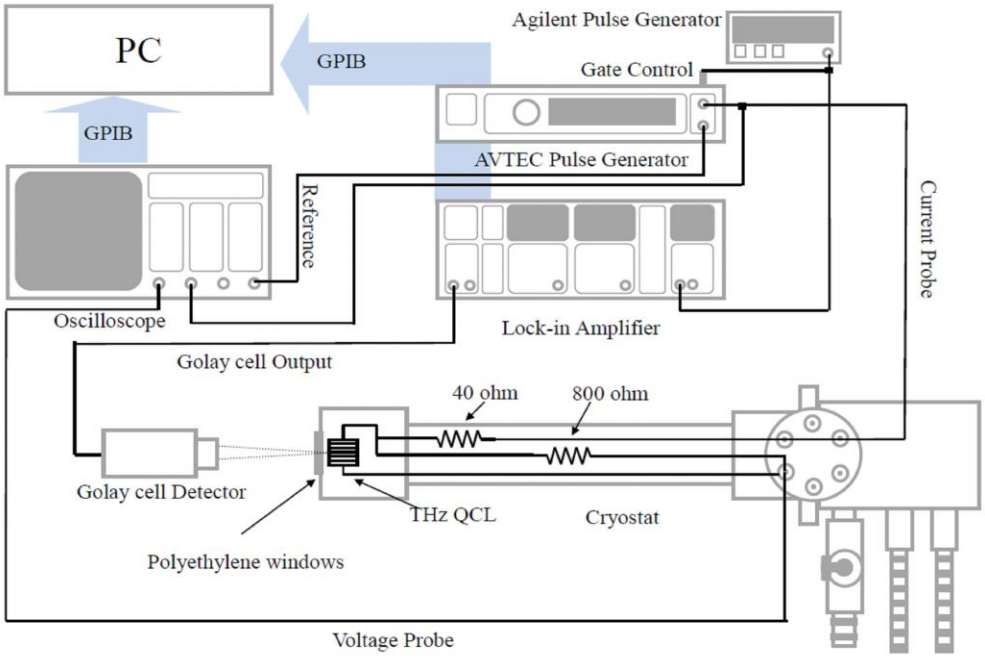

Figure 5.13 Schematic diagram of the characterization setup for pulse-mode THz QCL LJV measurements.

In pulse-mode LJV measurement, an AVTECH pulse generator is used to electrically pump the THz QCL with a train of pulses at a repetition rate of 1 kHz and with pulse width of 250 ns. A Golay cell serves as a detector for collecting the output terahertz radiation from THz QCLs. To offset the slow response time of the Golay cell, it was modulated by another Agilent pulse generator with a frequency of 20 Hz. The electric circuit inside the cryostat chamber, which includes two resistors (40 Ω and 800 Ω), is connected to match the output impedance of the AVTEC pulse generator. The current and voltage data from the THz QCL are measured through an oscilloscope (Tektronix MDO3054).

5.4.1 G0216 LJV results

Figure 5.14 shows the pulse-mode LJV measurement characteristics of THz QCL G0216

with cavity dimensions of 150 µm × 2.1 mm, at heat sink temperatures of 10 K to 144 K, with a pulse duration of 250 ns, and repetition rate of 1 kHz. The threshold current density (J_{th}) of 477 A/cm^2 and the maximum current density (J_{max}) of 841 A/cm^2 was measured at a heat sink temperature of 10 K. The wide dynamic range of $(J_{max}-J_{th})/J_{max}$=0.43, which improves the temperature performance of the device to enable a high maximum lasing temperature of 144 K (same as the current record for maximum lasing temperature reported in [72]) is due to low cavity loss, which proves the high quality of our device growth and waveguide fabrication.

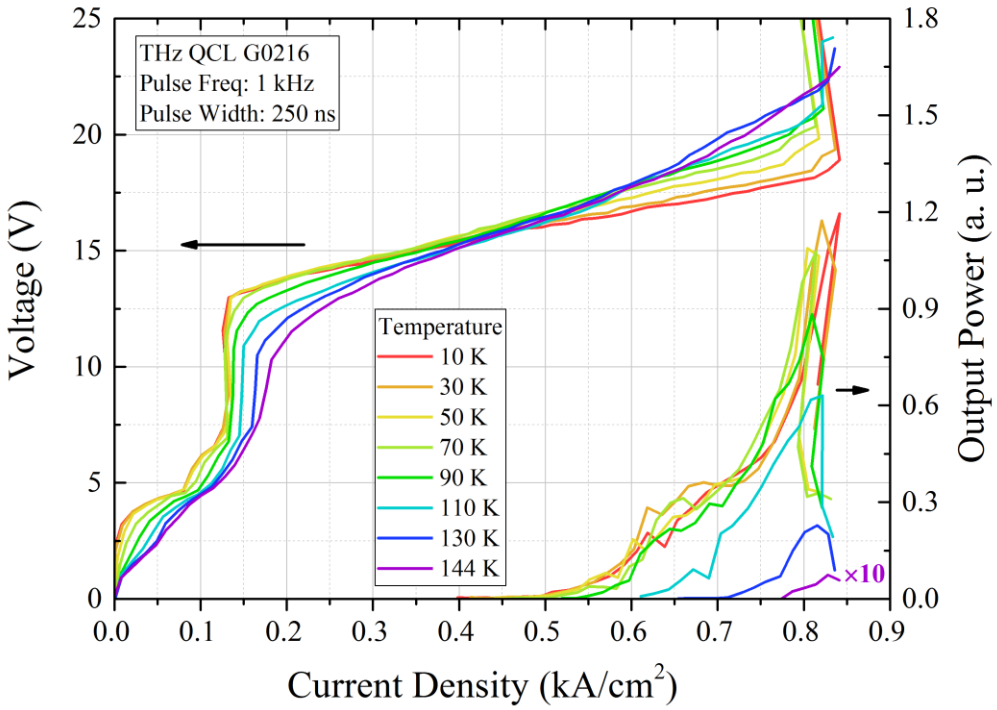

Figure 5.14 Left axis: The bias voltage of THz QCL G0216 versus current density at different heat sink temperatures. Right axis: Collected THz light (optical output power) from the Golaycell versus current density at different heat sink temperatures. The cavity dimension of the THz QCL is 150 µm × 2.1 mm. LJV measurements were taken under pulse mode with a pulse repetition frequency of 1 kHz and with a pulse width of 250 ns.

5.4.2 G0226 LJV and spectroscopy results

Figure 5.15 shows the pulse-mode LJV measurement characteristics of THz QCL G0226 with cavity dimensions of 150 µm × 2 mm, at heat sink temperatures of 20 K to 111 K, with a pulse duration of 250 ns, and repetition rate of 1 kHz. The threshold current density (J_{th}) of 218 A/cm^2 was measured at a heat sink temperature of 20 K, which is very close to the published J_{th} of 220 A/cm^2 in [44]. Also, the measured maximum lasing temperature for this device is 111 K, which is comparable with the reported highest operating temperature of 105 K in the supplementary material of [44]. Both the threshold current density and the maximum lasing temperature results for G0226 clearly confirmed good quality control in MBE growth for the heterogeneous active region structure and the in fabrication work of the THz QCL metal-metal waveguide.

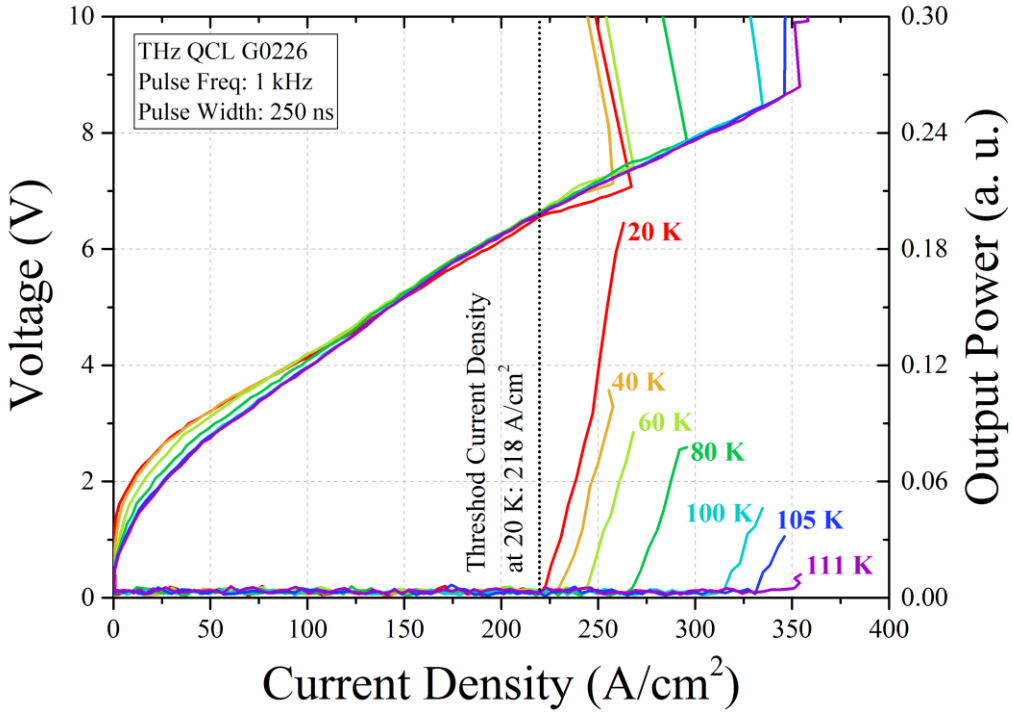

Figure 5.15 Left axis: The bias voltage versus current density analysis for THz QCL G0226 at different heat sink temperatures. Right axis: Collected THz light (optical output power) from the Golay cell versus current density at different heat sink temperatures. The cavity dimension of the THz QCL is 150 µm × 2 mm. LJV measurements were taken under pulse

mode with a pulse repetition frequency of 1 kHz and a pulse width of 250 ns. The threshold current density of this device, at a heat sink temperature of 20 K, is 218 A/cm^2 (marked with black dashed line).

To further compare the active region growth of THz QCL G0226 with the published result from ETH, the JV measurement results for both devices (taken at a heat sink temperature of 20 K) are plotted in Figure 5.16. The highly consistent shape of the JV curves from the two devices shows that the quantum designs of the heterogeneous structures (consisting of three different active regions) were accurately controlled during MBE growth, and confirms the XRD fitting data analysis (with maximum discrepancies of ~3% in layer thickness and ~0.2% in aluminum compositions).

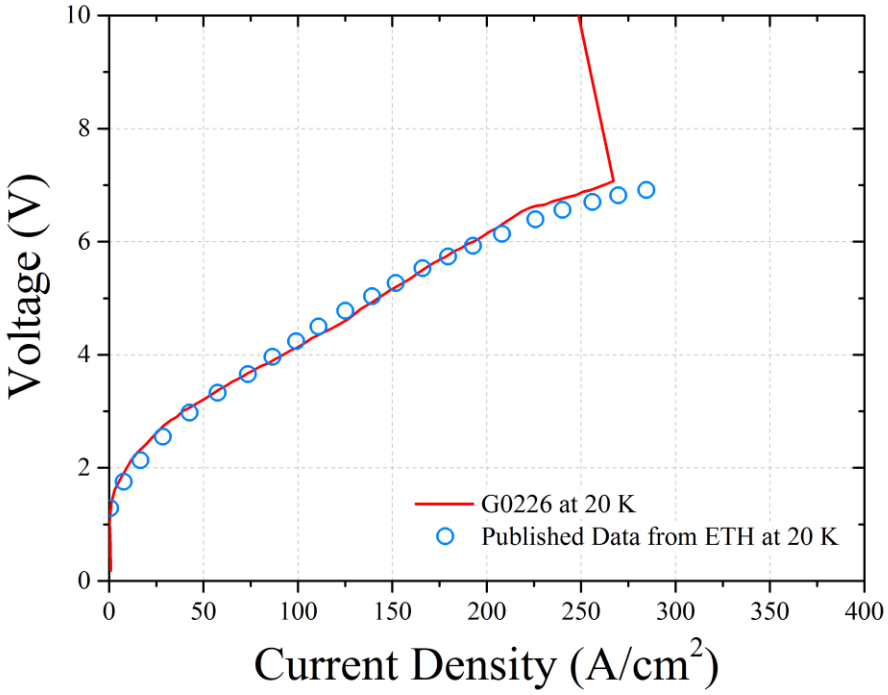

Figure 5.16 JV results for THz QCL G0226 (red solid line) and the device reported by ETH (blue circles) at a heat sink temperature of 20 K. Both devices have the same cavity dimensions (150 µm × 2 mm) and were tested under pulse mode.

Figure 5.17 shows the lasing spectrum of G0226 (150 µm × 2 mm) at an injected current density of 250 A/cm^2 (pulse mode, 1 kHz, and 0.15% duty cycle), at a heat sink

temperature of 13 K. The spectral measurements were carried out by using a commercial nitrogen purged Fourier-transform infrared (FTIR) spectrometer with a frequency resolution of 0.15 cm^{-1}. The lasing spectrum extends from 2.36 to 2.86 THz, including 20 observed Fabry-Perot (FP) lasing modes (the red peaks as labelled in Figure 5.17). These FP modes are equally spaced (marked by the grey dotted lines). The frequency spacing of adjacent lasing modes is ~21.8 GHz, corresponding well to the round-trip frequency in the 2-mm-long waveguide ($c/2nl$ = 3×10^8 m/s/($2\times3.4\times2\times10^{-3}$ m) = 22.0 $\times10^9$ s^{-1} = 22.0 GHz, assuming the effective refractive index of the waveguide is n = ~3.4). Some FP modes are missing in the spectrum (such as the one between 1 and 2 and the one between 17 and 18), which is attributed to the residual water vapor absorption existing in the FTIR system that was only dry nitrogen gas purged. The blue curve of Figure 5.17 shows that the spectral features of the residual water vapour absorption of the FTIR system (the blue curve) can be pretty strong at some frequencies.

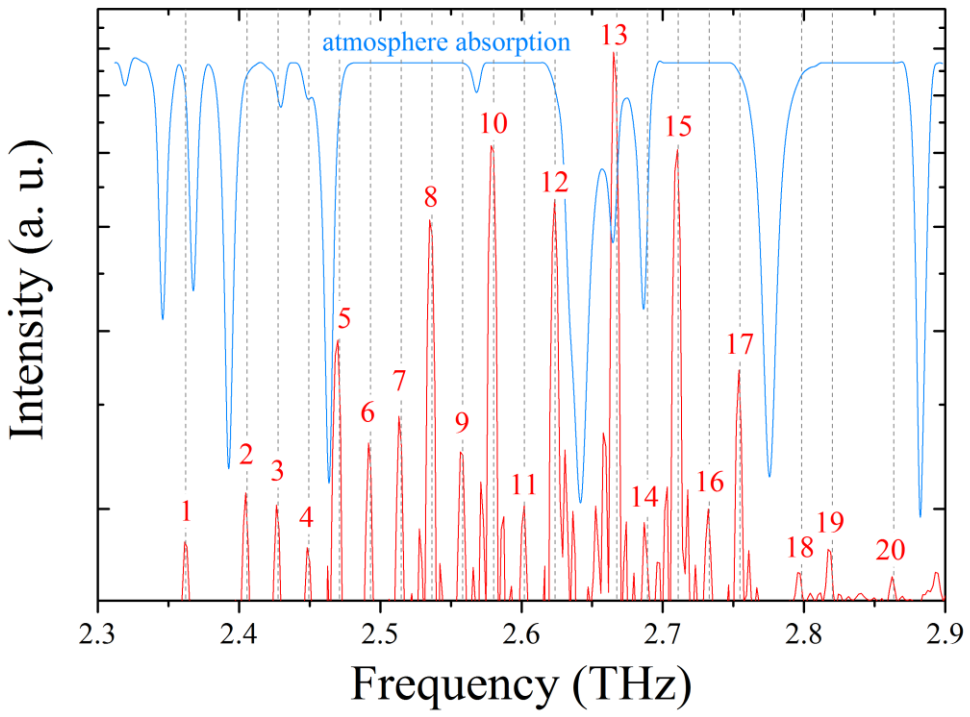

Figure 5.17 Red curve: lasing spectrum of THz QCL G0226 biased to 250 A/cm^2, at a heat sink temperature of 13 K. The device is 150 µm × 2 mm, and tested under pulse mode (1 kHz, 0.15% duty cycle). The frequencies of observed Fabry-Perot lasing modes are marked (grey dashed lines). Blue curve: atmosphere absorption.

5.5 Summary

In this chapter, the MBE growth results for two THz QCL active regions were presented. The XRD fitting results for the first device, THz QCL G0216, show the grown structure suffers mismatches of ~5% of in layer thickness and 2% in aluminum composition compared to target parameters. Results for the second, heterogeneous structure (G0226), only small discrepancies of ~3% in layer thicknesses and ~0.2% in aluminum compositions were observed, which indicated that the growth very nearly on target.

Achievements related to the fabrication of our THz QCL devices and metal-metal waveguides, were also presented. Several tested and, subsequently, optimized recipes for major fabrication steps were briefly introduced. As one of the most important steps for THz QCL fabrication, the RIE dry etching process, which produces critically import mesa ridges in our waveguides, was discussed, and two successful recipes were demonstrated.

To prove the quality of active region growth and metal-metal waveguide fabrication, LJV measurements results for THz QCL G0216 and G0226 were presented. Although the MBE growth of G0216 slightly shifted from the structure design, fabricated devices from G0216 still lased up to a maximum temperature of 144 K due to the success of the fabricated low-loss cavity as well as the high quality of the grown epitaxial layers. The LJV and spectrum measurement results for THz QCL G0226 were also presented. The experimental results are consistent in terms of maximum lasing temperature, threshold current density, the shape of the JV curve, and broad lasing spectrum, proving the high quality and stability of active region growth and waveguide fabrication. The lasing spectral result clearly demonstrates the lasing operation of the G0226 device with up to 20 equally-spacing Fabry-Perot modes, indicating potential frequency comb operation, which needs to be further confirmed by beat note signal measurements.

Chapter 6

Conclusion

In summary, a new THz QCL frequency comb device that covers a wide frequency range from 2 to 4 THz, is proposed based on the combination of a broadband gain active region design and a novel GVD-compensated DBR structure. Two new quantum-well active region designs, one based on a BTC scheme and one based on a RP scheme, are presented and simulated, both showing broad-band gain spectrum coverage. A complete theoretical model is established and employed to systematically investigate the behaviors of chirped DBR waveguides with different geometric parameters. A novel two-section chirped DBR waveguide is designed. The simulation results demonstrate improved GVD compensation over an octave frequency range from 2 to 4 THz. A THz QCL with a broad-band gain active region design is subsequently fabricated, which lases up to a maximum lasing temperature of 111 K.

To support heterogeneous active region design, a rate equation model is created and employed to simulate a previously reported heterogeneous structure. The simulation results are compared to the published experimental data. After confirming the model is capable of predicting the current-voltage (IV) and gain characteristics of THz QCLs with heterogeneous active regions, it is deployed to design and investigate two new heterogeneous structures with a lasing frequency coverage of 2-4 THz. In the first design, three different BTC active regions with central lasing frequencies of 2.5 THz, 3.1 THz, and 3.6 THz, respectively, are designed for achieving broad-band operation at a temperature of 25 K. The inherent broad gain bandwidths of each individual BTC active region together with the overall contribution of the heterogeneous structure yield an ultra-broadband gain spectrum coverage from 2 to 4 THz. In the second design, four different 3-well RP active regions with central lasing frequencies of 2.4 THz, 2.8 THz, 3.2 THz, and 3.6 THz are

designed for targeting an operating temperature of 77 K (liquid nitrogen temperature) or higher. The new design could lead to a new record operating temperature for ultra-broad-band THz QCLs.

To support waveguide design, a one-dimensional (1D) model, based on the transfer matrix method in MATLAB, is developed. A systematic investigation to explore the GVD compensation characteristcs of chirped DBR structures in metal-metal waveguides is performed. The simulation results reveal the basic behaviors and properties of the chirped DBR structure. A more rigorous three-dimensional (3D) model based on COMSOL is established for designing and simulating the chirped DBR waveguides for real devices. The simulation results show that to make deeper corrugations in the DBRs is more effective for achieving broadband reflectance than to increase the number of corrugation periods. Unfortunately, large corrugation depth would strongly distort the group delay dispersion compensation behavior of the DBRs.

To eliminate the strong ripples observed in the group delay curves, which result from the abrupt transition from the flat ridge segment to the chirped DBR segment, a two-section chirped DBR structure is proposed. The new two-section DBR consists of a buffer section between the flat ridge segment and the chirped DBR segment. The new two-section chirped DBR yields a much smoother group delay compensation over a very broad frequency range, which may significantly improve the performance of ultra-broad band frequency comb THz QCLs. Based on the simulation results, two groups of chirped DBR structures are designed: 1. A conventional chirped DBR structure for GVD compensation between 2.5 THz and 3.5 THz for our F-series THz QCLs; 2. A two-section chirped DBR structure for GVD compensation over an octave-spanning frequency range from 2 to 4 THz for the new heterogeneous active regions mentioned earlier.

Two THz QCL wafers are grown using MBE: G0216 which is based on the SA scheme, and G0226, which is based on the BTC scheme. G0226 is a heterogeneous structure that consists of three quantum designs targeting different lasing frequencies. Microfabrication recipes are developed and THz QCLs are fabricated at the Quantum –

Nano -Centre clean-room fab lab. The light-current density-voltage (LJV) measurement results of the G0216 THz QCLs demonstrate a high maximum lasing temperature of 144 K. The LJV measurement results of the G0226 device reveal a maximum lasing temperature of 111 K, and a low threshold current density of 218 A/cm^2. The pulse mode spectrum measurement result of the G0226 device show a broad lasing spectrum covering the frequencies from 2.36 to 2.86 THz at a temperature of 13 K, representing the frequency comb operation. The experimental results confirm the high quality and stability of the MBE growth of semiconductor quantum structures as well as the device microfabrication.

Bibliography

[1] C. Sirtori, "Bridge for the terahertz gap," Nature, 417, 132 (2002)

[2] X. Yang, X. Zhao, K. Yang, Y. P. Liu, Y, Liu, W. Fu, and Y. Luo, "Biomedical Applications of Terahertz Spectroscopy and Imaging," Trends in Biotechnology 34, 810-824 (2016).

[3] M. Tonouchi, " Cutting-edge terahertz technology," Nature Photonics, 1, 97 (2007).

[4] N. Nagai, R. Kumazawa, and R. Fukasawa, " Direct evidence of inter-molecular vibrations by THz spectroscopy," Chem. Phys. Lett., 413, 495 (2005).

[5] G.P. Gallerano and S. Biedron, "Overview of terahertz radiation sources," Proceedings of the 2004 FEL Conference, 216-221 (2004)

[6] F. C. Cruz, G. T. Nogueira, L. F. L. Costa, N. C. Frateschi, R. C. Viscovini, and D. Pereira, "Continuous and pulsed THz generation with molecular gas lasers and photoconductive antennas gated by femtosecond pulses," IEEE MIT-S IMOC, 446-449 (2007)

[7] A. Khalid, G. M. Dunn, R. F. Macpherson, S. Thoms, D. Macintyre, C. Li, M. J. Steer, V. Papageorgiou, I. G. Thayne, M. Kuball, C. H. Oxley, M. Montes Bajo, A. Stephen, J. Glover, and D. R. S. Cumming, "Terahertz oscillations in an $In_{0.53}Ga_{0.47}As$ submicron planar Gunn diode," J. Appl. Phys. 115, 114502 (2014)

[8] M. Mukherjee, N. Mazumder, S. K. Roy, and K. Goswami, "GaN IMPATT diode: a photo-sensitive high power terahertz source," Semicond. Sci. Technol. 22, 1258-1267 (2007)

[9] K. J. P. Jacobs, B. J. Stevens, O. Wada, T. Mukai, D. Ohnishi, and R. A. Hogg, "A dual-pass high current density resonant tunneling diode for terahertz wave applications," IEEE Electron Device Letters 22, 1295-1298 (2015)

[10] G. L. Carr, M. C. Martin, W. R. McKinney, K. Jordan, G. R. Neil, and G. P. Williams, "High-power terahertz radiation from relativistic electrons," Nature 420, 153-156 (2002)

[11] S. Par, Y. Choi, Y. Oh, K. Jeong, "Terahertz photoconductive antenna with metal nanoislands," Opt. Express 20, 25530-25535 (2012)

[12] R. Kohler, A. Tredicucci, F. Beltram, H. E. Beere, E. H. Linfield, A. G. Davies, D. A. Ritchie, R. C. Iotti and F. Rossi, "Terahertz semiconductor-heterostructure laser," Nature 417, 156-159 (2002).

[13] M. S. Vitiello, G. Scalari, B. Williams, and P. D. Natale, "Quantum cascade lasers: 20 years of challenges," Opt. Express 2, 5167-5182 (2015).

[14] Th. Udem, R. Holzwarth, and T. W. Hansch, "Optical frequency comb metrology," Nature 416, 233-237 (2002)

[15] S. T. Cundiff, and J. Ye, "Femtosecond optical frequency combs," Rev. Mod. Phys. 75, 325 (2003)

[16] J. Ye, and S. T. Cundiff, "Femtosecond optical frequency comb: principle, operation and applications," Springer, New York (2005)

[17] F. C. Cruz, "Optical frequency combs generated by four-wave mixing in optical fibers for astrophysical spectrometer calibration and metrology," Opt. Express 16, 13267-13275 (2008)

[18] S. A. Diddams, "The evolving optical frequency comb," J. Opt. Soc. Am. B 27, B51-62 (2010).

[19] K. L. Corwin, I. Thomann, T. Dennis, R. W. Fox, W. Swann, E. A. Curtis, C. W. Oates, G. Wilpers, A. Bartells, S. L. Gilbert, L. Hollberg, N. R. Newbury, and S. A. Diddams, "Absolute-frequency measurements with a stabilized near-infrared optical frequency comb from a Cr:forsterite laser," Opt. Lett. 29, 397-399 (2004)

[20] S. Bartalini, P. Cancio, G. Giusfredi, D. Mazzotti, and P. De Natale, "Frequency-comb-referenced quantum-cascade laser at 4.4 μm," Opt. Lett. 32, 988-990 (2007)

[21] I. Coddington, N. Newbury, and W. Swann, "Dual-comb spectroscopy," Optica 3, 414-425 (2016).

[22] G. Millot, S. Pitois, M. Yan, T. Hovhannisyan, A. Bendahmane, T. W. Hansch, and N. Picque, "Frequency-agile dual-comb spectroscopy," Nat. Photonics 10, 27-30 (2015).

[23] F. Keilmann, C. Gohle, and R. Holzwarth, "Time-domain mid-infrared frequency-comb spectrometer," Opt. Lett. 29, 1542-1544 (2004).

[24] B. S. Williams, "Terahertz quantum-cascade lasers, " Nat. Photonics 1, 517-525 (2007)

[25] M. Rochat, L. Ajili, H. Willenberg, J. Faist, and H. Beere, "Low-threshold terahertz quantum cascade lasers," Appl. Phys. Lett. 81, 1381-1383 (2002)

[26] A. Tredicucci, R. Kohler, F. Beltram, H. E. Beere, E. H. Linfield, A. G. Davies, and D. A. Ritchie, "Terahertz quantum cascade lasers," Physica E 21, 846-851 (2004)

[27] G. Scalari, N. Hoyler, M. Giovannini, and J. Faist, "Terahertz bound-to-continuum quantum-cascade lasers based on optical-phonon scattering extraction," Appl. Phys, lett. 86, 181101 (2005).

[28] S. Barbieri, J. Alton, H. E. Beere, J. Fowler, E. H. Linfield, "2.9 THz quantum cascade lasers operating up to 70K in continuous wave," Appl. Phys. Lett. 85, 1674-1676 (2004)

[29] L. Mahler, A. Tredicucci, R. Kohler, F. Beltram, and H. E. Beere, "High-performance operation of single-mode terahertz quantum cascade lasers with metallic gratings," Appl. Phys. Lett. 84, 181101 (2005)

[30] B. S. Williams, S. Kumar, H. Callebaut, Q. Hu, and J. L. Reno, "Terahertz quantum-cascade laser operating up to 137 K," Appl. Phys. Lett. 83, 5142-5144 (2003)

[31] S. Kumar, Q. Hu, and J. L. Reno, "186 K operation of terahertz quantum-cascade lasers based on a diagonal design," Appl. Phys. Lett. 94, 131105 (2009)

[32] S. Fathololoumi, E. Dupont, C. W. I. Chan, Z. R. Wasilewski, S. R. Laframboise, D. Ban, A. Matyas, C. Jirauschek, Q. Hu, and H. C. Liu, "Terahertz quantum cascade lasers operating up to ~200 K with optimized oscillator strength and improved injection tunneling," Opt. Express 20, 3866-3876 (2012).

[33] E. Dupont, S. Fathololoumi, Z. R. Wasilewski, S. R. Laframboise, M. Lindskog, S. G. Razavipour, A. Wacker, D. Ban, and H. C. Liu, "A phonon scattering assisted injection and extraction based terahertz quantum cascade laser," J. Appl. Phys. 111, 073111 (2012).

[34] S. G. Razavipour, E. Dupont, S. Fathololoumi, C. W. I. Chan, M. Lindskog, Z. R. Wasilewski, G. Aers, S. R. Laframboise, A. Wacker, Q. Hu, D. Ban, and H. C. Liu, "An indirectly pumped terahertz quantum cascade laser with low injection coupling strength operating above 150 K," J. Appl. Phys. 113, 203107 (2013)

[35] B. S. Williams, H. Callebaut, S. Kumar, Q. Hu, and J. L. Reno, "3.4 THz quantum cascade laser based on longitudinal-optical-phonon scattering for depopulation," Appl. Phys. Lett. 82, 1015-1017 (2003)

[36] B. S. Williams, S. Kumar, H. Callebaut, Q. Hu, and J. L. Reno, "Terahertz quantum-cascade laser at $\lambda \approx 100$ μm using metal waveguide for mode confinement," Appl. Phys. Lett. 83, 2124 (2003).

[37] J. A. Fan, M. A. Belkin, F. Capasso, S. P. Khanna, and M. Lachab, "Wide-ridge metal-metal terahertz quantum cascade lasers with high-order lateral mode suppression," Appl. Phys. Lett. 92, 031106 (2008)

[38] C. Xu, S. G. Razavipour, Z. Wasilewski, and D. Ban, "An investigation on optimum ridge width and exposed side strips width of terahertz quantum cascade lasers with metal-metal waveguides," Opt. Express 21, 31951 (2013).

[39] J. B. Khurgin, Y. Dikmelik, A. Hugi, and J. Faist, "Coherent frequency combs produced by self frequency modulation in quantum cascade lasers," Appl. Phys. Lett. 104, 081118 (2014)

[40] G. Villares and J. Faist, "Quantum cascade laser combs: effects of modulation and dispersion," Opt. Express 23, 1651-1669 (2015).

[41] R. W. Boyd, "Nonlinear Optics (3rd edition)," Academic Press (2008)

[42] D. Burghoff, Y. Yang, J. L. Reno, and Q. Hu, "Dispersion dynamics of quantum cascade lasers," Optica 1, 1-5 (2014)

[43] D. Bachmann, M. Rosch, G. Scalari, M. Beck, J. Faist, K. Unterrainer, and J. Darmo, "Dispersion in a broadband terahertz quantum cascade laser," Appl. Phys. Lett. 109, 221107 (2016)

[44] M. Rosch, G. Scalari, M. Beck, and J. Faist, "Octave-spanning semiconductor laser," Nat. Photonics 9, 42 (2015)

[45] D. Burghoff, T.-Y. Kao, N. Han, C. W. I. Chan, X. Cai, Y. Yang, D. J. Hayton, J.-R. Gao, J. L. Reno, and Q. Hu, "Terahertz laser frequency combs," Nat. Photonics 8, 462–467 (2014)

[46] T. Ando, "Line width of inter-subband absorption in inversion layers: scattering from charged ions," J. Phys. Soc. Jpn. 54, 2671-2675 (1985).

[47] P. Harrison, "Quantum Wells, Wires and Dots: Theoretical and Computational Physics," John Wiley & Sons (2005)

[48] C. Deutsch, H. Detz, M. Krall, M. Brandstetter, T. Zederbrauer, A. M. Andrews, W. Schrenk, G. Strasser, and K. Unterrainer, "Dopant migration effects in terahertz quantum cascade lasers," Appl. Phys. Lett. 102, 201102 (2013)

[49] H. Callebaut, S. Kumar, B. S. Williams, Q. Hu, and J. L. Reno, "Importance of electron-impurity scattering for electron transport in terahertz quantum-cascade lasers," Appl. Phys. Lett, 84, 645 (2004)

[50] T. Unuma, M. Yoshita, T. Noda, H. Sakaki, and H. Akiyama, "Intersubband absorption linewidth in GaAs guantum wells due to scattering by interface roughness, phonons, alloy disorder, and impurities," J. Appl. Phys. 93, 1586-1597 (2003)

[51] R. Terazzi, T. Gresch, A. Wittmann, and J. Faist, "Sequential resonant tunneling in quantum cascade lasers," Phys, Rev. B 78, 155328 (2008)

[52] R. Terazzi and J. Faist, "A density matrix model of transport and radiation in quantum cascade lasers," New journal of Physics, 12, 033045 (2010)

[53] S. G. Razavipour, "Design, Analysis, and Characterization of Indirectly-pumped Terahertz Quantum Cascade Lasers," Thesis, University of Waterloo, Dept. of Electrical and Computer Engineering, (2013)

[54] S. L. Chuang, "Physics of Photonic Devices (2nd edition)," John Wiley & Sons (2009)

[55] D. Turcinkova, G. Scalari, F. Castellano, M. I. Amanti, M. Beck, and J. Faist, "Ultra-broadband heterogeneous quantum cascade laser emitting from 2.2 to 3.2 THz," Appl. Phys. Lett. 99, 191104 (2011)

[56] M. I. Amanti, G. Scalari, R. Terazzi, M. Fischer, M. Beck, J. Faist, A. Rudra, P. Gallo, and E. Kapon, "Bound-to-continuum terahertz quantum cascade laser with a single-quantum-well phonon extraction/injection stage," New Journal of Physics 11, 125022 (2009)

[57] R. S. Dhar, S. G. Razavipour, E. Dupont, C. Xu, S. Laframboise, Z. Wasilewski, Q. Hu, and D. Ban, "Direct nanoscale imaging of evolving electric field domains in quantum structures," Scientific Reports 4, 7183 (2014)

[58] H. Yasuda, I. Hosako, and K. Hirakawa, "High-field domains in terahertz quantum cascade laser structures based on resonant-phonon depopulation scheme," Infrared, Millimeter, and Terahertz Waves, 38th International Conference on IEEE (2013)

[59] C. Sirtori, F. Capasso, J. Faist, and S. Scandolo, "Nonparabolicity and a sum rule associated with bound-to-bound and bound-to-continuum intersubband transitions in quantum wells," Phys. Rev. B, 50, 8663-8674 (1994)

[60] D. Burghoff, "Broadband terahertz photonics," Thesis, Massachusetts Institute of Technology, Dept. of Electrical Engineering and Computer Science (2014)

[61] S. Fathololoumi, E. Dupont, Z. R. Wasilewski, C. W. I. Chan, S. G. Razavipour, S. R. Laframboise, S. Huang, Q. Hu, D. Ban, and H. C. Liu, "Effect of oscillator strength and intermediate resonance on the performance of resonant phonon-based terahertz quantum cascade lasers," J. Appl. Phys. 113, 113109 (2013)

[62] A. Hugi, G. Villares, S. Blaser, H. C. Liu, & J. Faist, "Mid-infrared frequency comb based on a quantum cascade laser," Nature 492, 229–233 (2012)

[63] F. Ouellette, "Dispersion cancellation using linearly chirped Bragg grating filters in optical waveguides," Opt. Lett. 12 (10), 847 (1987).

[64] M. Sumetsky and B. J. Eggleton, "Fiber Bragg gratings for dispersion compensation in optical communication systems," J. Opt. Fiber Commun. Rep. 2, 256-278 (2005).

[65] J. S. Blakemore, "Semiconducting and other major properties of gallium arsenide," J. Appl. Phys. 53, R123–R181 (1982).

[66] M. Strain, "Integrated chirped Bragg gratings for dispersion control," Thesis, University of Glasgow, Depts. of Electronics and Electrical Engineering (2007)

[67] P. Yeh, "Optical waves in layered media," John Wiley & Sons, Singapore (1991)

[68] F. Gires, and P. Tournois. "Interferometre utilisable pour la compression d'impulsions lumineuses modulees en frequence," C. R. Acad. Sci. Paris 258, 6112–6115 (1964)

[69] J. P. Berenger, "A perfectly matched layer for the absorption of electromagnetic waves," J. Comput. Phys. 114, 185-200 (1994)

[70] C. Xu and D. Ban, "Design of chirped distributed Bragg reflector for octave-spanning frequency group velocity dispersion compensation in terahertz quantum cascade laser," Opt. Express 24, 13500-13510 (2016)

[71] S. Fathololoumi, E. Dupont, Z. R. Wasilewski, C. W. I. Chan, S. G. Razavipour, S. R. Laframboise, S. Huang, Q. Hu, D. Ban, and H. C. Liu, "Effect of oscillator strength and intermediate resonance on the performance of resonant phonon-based terahertz quantum cascade lasers," J. Appl. Phys. 113, 113109 (2013)

[72] S. Khanal, J. L. Reno, and S. Kumar, "2.1 THz quantum-cascade laser operating up to 144 K based on a scattering-assisted injection design," Opt. Express 23, 19689-19697 (2015)

[73] N. Han, "Electrically tunable terahertz quantum cascade lasers," Thesis, Massachusetts Institute of Technology, Depts. of Electrical Engineering and Computer Science (2013)

[74] Y. Yang, "Towards Terahertz Dual-comb Spectroscopy Based on Quantum Cascade Lasers," Thesis, Massachusetts Institute of Technology, Depts. of Electrical Engineering and Computer Science (2015)

[75] S. Kohen, B. S. Williams and Q. Hu, "Electromagnetic modeling of terahertz quantum cascade laser waveguides and resonators," J. Appl. Phys. 97, 053106 (2005).

[76] S. Kumar, "Development of terahertz quantum-cascade lasers," Thesis, Massachusetts Institute of Technology, Dept. of Electrical Engineering and Computer Science (2007)

[77] H. Li, P. Laffaille, D. Gacemi, M. Apfel, C. Sirtori, J. Leonardon, G. Santarelli, M. Rosch, G. Scalari, M. Beck, J. Faist, W. Hansel, R. Holzwarth, and Stefano. Barbieri, "Dynamics of ultra-broadband terahertz quantum cascade lasers for comb operation," Opt. Express 23, 33270-33294 (2015)

[78] J. Maysonnave, K. Maussang, J. R. Freeman, N. Jukam, J. Madeo, P. Cavalie, R. Rungsawang, S. P. Khanna, E. H. Linfield, A. G. Davies, H. E. Beere, D. A. Ritchie, S. S. Dhillon, and J. Tignon, "Mode-locking of a terahertz laser by direct phase synchronization," Opt. Express 20, 20885 (2012)

[79] M. Wienold, B. Roben, L. Schrottke, and H. T. Grahn, "Evidence for frequency comb emission from a Fabry-Perot terahertz quantum-cascade laser," Opt. Express 22, 30410-30424 (2014)